



저작자표시-비영리-변경금지 2.0 대한민국

이용자는 아래의 조건을 따르는 경우에 한하여 자유롭게

- 이 저작물을 복제, 배포, 전송, 전시, 공연 및 방송할 수 있습니다.

다음과 같은 조건을 따라야 합니다:



저작자표시. 귀하는 원 저작자를 표시하여야 합니다.



비영리. 귀하는 이 저작물을 영리 목적으로 이용할 수 없습니다.



변경금지. 귀하는 이 저작물을 개작, 변형 또는 가공할 수 없습니다.

- 귀하는, 이 저작물의 재이용이나 배포의 경우, 이 저작물에 적용된 이용허락조건을 명확하게 나타내어야 합니다.
- 저작권자로부터 별도의 허가를 받으면 이러한 조건들은 적용되지 않습니다.

저작권법에 따른 이용자의 권리와 책임은 위의 내용에 의하여 영향을 받지 않습니다.

이것은 [이용허락규약\(Legal Code\)](#)을 이해하기 쉽게 요약한 것입니다.

[Disclaimer](#)



Ph. D. DISSERTATION

**Study on surface plasmon caustic and vortex
pattern generation using plasmonic lens**

**플라즈모닉 렌즈를 이용한 표면 플라즈몬 커스틱과
소용돌이 형상 생성에 관한 연구**

By

SEONG-WOO CHO

AUGUST 2012

**DEPARTMENT OF ELECTRICAL ENGINEERING AND
COMPUTER SCIENCE
COLLEGE OF ENGINEERING
SEOUL NATIONAL UNIVERSITY**

Abstract

Study on surface plasmon caustic and vortex pattern generation using plasmonic lens

SEONG-WOO CHO

DEPARTMENT OF ELECTRICAL ENGINEERING AND
COMPUTER SCIENCE
COLLEGE OF ENGINEERING
SEOUL NATIONAL UNIVERSITY

Surface plasmon (SP) waves are highly confined electromagnetic waves that propagate along the interface between a metal and a dielectric material via the coupling of the electrons in the metal. The groundwork for plasmonic structures has been laid through intensive studies of surface plasmon polaritons (SPPs) propagation in metal-dielectric structures. The combination of these plasmonic nano-structures can generate various useful SP interference patterns on metal surfaces. SP pattern generation is a fundamental research area of plasmonics that was initiated very recently. Although research on SP pattern generation started from the formation of SP focal spots, specifically hot spots on a subwavelength scale, the diffractive synthesis of complex SP fields as well as single hot spots and dynamic control of the SP fields for various applications came before most plasmonics research. In this dissertation, I investigate the modulation of SP patterns using a plasmonic lens and propose a method to generate various surface plasmon patterns using a plasmonic lens.

I show that directional curved optical power flows can be generated through SP

caustics. Light caustic is the curved envelope of concentrated light waves that can take various geometric patterns in nature. The SP caustic light flow proposed in this dissertation is a generalization and enrichment of the recent focusing approaches of SPs with an additional concept of directional power flow control. I devise the plasmonic caustic fouscator for generating plasmonic caustic light flows and demonstrate various curved low-dimensional light power flows experimentally. The plasmonic caustic focusators provide a novel degree of freedom in managing low-dimensional light fields.

I present that two distinct optical properties of light, the spin angular momentum (SAM) and the orbital angular momentum (OAM), can be coupled in the plasmonic vortex. If a plasmonic vortex lens (PVL) is illuminated by the helical vector beam (HVB) with the SAM and OAM, then those distinct angular momenta contribute to the generation of the plasmonic vortex together. The analytical model reveals that the total topological charge of the generated plasmonic vortex is given by a linear summation of those of the SAM and OAM, as well as the geometric charge of the PVL. The generation of the plasmonic vortex and the manipulation of the fractional topological charge are also presented.

The generation of surface plasmon vortices with plasmonic vortex lens is experimentally demonstrated. It is shown that the polarization sensitivity of the plasmonic vortex lens can be utilized for the dynamic switching of the surface plasmon vortices with different topological charges. A simple algebraic rule related to the vortex topological charge change in the dynamic switching is verified with experiment. The generation of multiple vortex-cones using an annular aperture array and a spatial light modulator is studied. It is experimentally demonstrated that the direct-phase modulation of an annular aperture array can control both the topological charge and the horizontal positions of multiple vortex-cones simultaneously.

Keywords: Plasmonics, nanophotonics, surface plasmons, diffraction limit, plasmonic vortex, plasmonic lens, surface plasmon pattern generation, plasmonics hot spot, plasmonic fouscator, helical vector beam, caustics, vortex beam, angular momentum

Student number: 2007-30841

List of Figures

Figure 1.1 SPs at the interface between a metal and a dielectric material have a combined electromagnetic wave and surface charge characteristic. They are transverse magnetic in character (H is in the y direction), and the generation of the surface charge requires an electric field normal to the surface. This combined characteristic also causes the field component perpendicular to the surface to be enhanced near the surface while decaying exponentially as the distance away from it increases.	4
Figure 1.2 Dispersion of SPP at a dielectric–metal interface. Also plotted is the dispersion of light in the dielectric medium, and the corresponding surface plasmon frequency.	6
Figure 1.3 NSOM measurement showing SPP focusing in a plasmonic lens illuminated by radially (left) and linearly (right) polarized light. A radially polarized laser generates a single hot spot and a linearly polarized laser generates a double hot spot [15].	8
Figure 1.4 Spin-dependent geometric phase in the spiral plasmonic structure [16]....	9
Figure 1.5 Surface plasmon patterns generated by a plasmonic lens are shown: (a) a plasmonic vortex, (b) a super-ellipse, (c) the letter ‘S’, and (d) a triangle	10
Figure 2.1(a) Caustic network observed inside of cup, (b) schematic of caustic network.....	15
Figure 2.2 Design of the PCF for synthesizing the SP caustic light flow. PCF for a super-ellipse. The SP rays generated at the PCF propagate inward and the envelope of the SP rays forms a super-ellipse-shaped SP caustic light flow. The derivative of the parameterized coordinate $(x(t),y(t))$ of any arbitrary caustic light flow allows for the tangential line, the end point	

of which results in the trajectory coordinate $(X(t), Y(t))$ of the PCF. The SP rays generated along the PCF are normal to the PCF and tangential to the SP caustic light flow.....	16
Figure 2.3 (a) Simulation results for the SP caustic light flow. It is assumed that point-source-like Green functions are located along the trajectory of PCF (shown as a dotted white curve). (c) The Poynting vector stream calculated on the PCF surface. The region of interest is presented in (b) as a square with a white dashed line. It is shown that a low-dimensional light energy flow circulates in the counter-clockwise direction along the super-ellipses SP caustic pattern.....	17
Figure 2.4 (a) Vector Green function of SP field in two-dimensional space and (b) total SP field generated by a PCF represented by the line integral of the vector Green function on the specified curve on the PCF.....	18
Figure 2.5. Schematic diagram of the NSOM measurement setup. The PCF on the silver film evaporated on the fused silica substrate is illuminated from the back side by a circularly polarized laser beam with a wavelength of 980 nm. The near-field distribution near the center is collected through the aperture in the NSOM tip.....	22
Figure 2.6. SEM image of the PCF producing a super-ellipse SP caustic light flow. The scale bar is 20 μm	24
Figure 2.7 CCD image of the PCF under the illumination of the circularly polarized light beam and the bright curve observed in the CCD image corresponds to the transmitted light through the designed slit. The dark shadow near the center is the shadow of the NSOM tip approaching the metal film. The rectangle with the white dashed lines shows the scanned window.....	26
Figure 2.8 The NSOM image near the center of the configuration. The scale bar in the NSOM image corresponds to 2.5 μm . The NSOM image of the super-ellipse with a major axis of 9 μm and a minor axis of 6 μm can	

clearly be observed.....	26
Figure 2.9 SP caustic light flows with spatial multiplexing. Composite caustic pattern composed of continuous arrangement of several partial caustic curves. The SP caustic light flow patterns can be divided into multi segments in such a way that there is no inflection point in each segment.....	28
Figure 2.10 Spatial multiplexing of the multi-segment SP caustic light flows. An example of the ‘S’-shaped SP caustic light flow is presented. The upper curve of the ‘S’ letter, denoted by the solid green line, is generated by the left bottom arc of the PCF (the dashed green line), whereas the lower curve (the red solid line) corresponds to the right upper arc of the PCF (the dashed red line). The arrows at the PCF arcs denote the directions for a hypothetical binding process of a tight rope in the design of the PCF.....	28
Figure 2.11 PCF patterns for (a) letter ‘S’, (b) triangle, (c) square, and (d) pentagon. Since the SP caustic flow light with straight line patterns cannot be implemented, the apex and edge of polygons are expressed as convex and concave super-formula curves, respectively.....	30
Figure 2.12 Synthesis of arbitrary SP caustic light flows. (a)–(d) Caustic light flow for the letter ‘S’. (e)–(h) Caustic light flow for a triangle. (i)–(l) Caustic light flow for a square. (m)–(p) Caustic light flow for a pentagon. (a), (e), (i), and (m) are the SEM images and the scale bars correspond to 30 μm . (b), (f), (j), and (n) are the experimental results of the NSOM measurement and the scale bars are 5 μm . (c), (g), (k), and (o) are the simulation results and the scale bars denote the length of 5 μm . (d), (h), (l), and (p) are the Poynting vector streams calculated on the PCF surface.....	32
Figure 2.13. (a) SP wave crossing over the metal gap with an incidence angle of θ . (b) transmission efficiency and c, phase delay for various incidence angles.....	35
Figure 3.1 Electric field distributions at a fixed time for various combinations of polarization states and helix winding numbers (Top panel: the LCP, middle panel: the radial polarization, bottom panel: the RCP). The	

helix winding number l varies from -1 to 2 with increment of 1.....	39
Figure 3.2 Three cases of SP excitation at a slit with the backside illumination. (a) The polarization of illuminating light is perpendicular to the slit. (b) The direction of the polarization having a nonzero angle to the direction of SPs propagation. (c) The slit is illuminated by the HVB.	41
Figure 3.3 Phase diagram of SPs generated at the PVL for four cases: (a) $(l, m, s) = (0, 0, 0)$, (b) $(l, m, s) = (1, 0, 0)$, (c) $(l, m, s) = (0, 0, 1)$, and (d) $(l, m, s) = (0, 1, 0)$. The most left panel corresponds to the phase of $\omega t = 0$. As time evolves, each phase decreases since wave functions have the time-dependence of $\exp(-i\omega t)$. The most right panel exhibits the phase of $\omega t = 3\pi/2$	43
Figure 3.4 Hypothetical experimental setup. The PVL is inscribed on the gold layer. The wavelength of laser is 660 nm and the corresponding wavelength of SPs is 641 nm.....	47
Figure 3.5 Schematic diagram of the converging angular spectrum of the SP waves inside the plasmonic vortex lens with $m=2$ under (a) the radial polarization, (b) the right-handed circular polarization, and (c) the left-handed circular polarization. The black arrows in upper right corners show the polarization states. The red, green, blue, and yellow arrows correspond to the out-of-plane electric field E_z with the relative phase difference of 0, $\pi/2$, π , and $3\pi/2$, respectively. The dark colors are used to give emphasis on the phases along the circumference of a circle.	50
Figure 3.6 Simulation result with various HVBs for a fixed geometrical charge ($m = 1$). For the sake of clear comparison, the arrangement of panels is the same as that in Figure 3.1.....	51
Figure 3.7 Geometric effect of PVL. (a) $(l, m, s) = (0, 1, 0)$, (b) $(l, m, s) = (0, 3, 0)$, (c) $(l, m, s) = (-1, 3, -1)$	52
Figure 3.8 Radius of vortex as a function of azimuthal phase term l . Each figure displays different geometric effect, (a) $m = -1$, (b) $m = 0$, (c) $m = 1$, (d) $m = 2$. The blue dashed, green dotted, and red solid lines with diamond,	

cross, and circle markers denote results of the RCP, the radial polarization, and the LCP, respectively. The black dashed lines denote solution of the Bessel function of the first kind.....	53
Figure 3.9 Phase discontinuity breaks the plasmonic vortex pattern as shown in (a) with $(l, m, s) = (0, 1.7, 0)$. The phase of surface plasmon at the center of PVL is represented in (b) with $(l, m, s) = (0, 1.7, 0)$	55
Figure 3.10 The phase profile is obtained along the white circle in Figure 3.9 and shown in (a) $(l, m, s) = (0, 1.7, 0)$, (b) $(l, m, s) = (1.3, 0, 0)$, (c) $(l, m, s) = (1.3, 1.7, 0)$, and (d) $(l, m, s) = (2, 0, 1)$. When j is fractional, the phase varies nonlinearly as shown (a) and (b). When j is integer, the phase varies linearly as shown in (c) and (d). This figure shows superposition property, $j = l + m + s$	56
Figure 4.1 (a) SEM image of the PVL with the geometrical vortex topological charge $m=4$. The inner (r_i) and outer (r_o) radii are $4.00 \mu\text{m}$ and $4.64 \mu\text{m}$, respectively. (b) Experimental setup for the NSOM. Illuminated from the bottom is the laser with the free space wavelength of 660 nm and the circular polarization.....	62
Figure 4.2 Experiment and simulation results under the right-handed circular polarization in (a)-(d). (a) Near-field intensity distribution measured by the NSOM. (b) Near-field intensity distribution calculated by the RCWA. The dark spot is clearly observed in both images. (c) E_z distribution of the near-field calculated by the RCWA. The number of node lines is five, which indicates that the topological charge of the SP vortex is $j=5$. The white arrows in (a)-(c) denote the directions of the rotation of the polarization. (d) Comparison of the intensity profiles. The red dashed line corresponds to the result of the theoretical model i.e., the square of the absolute value of the 5th order Bessel function of the first kind. The blue solid line depicts the field intensity along the dashed line in the NSOM image (Figure 4.2(a)). The black dotted line shows the field intensity along the dotted line in the RCWA image (Figure 4.2(b)).....	65

Figure 4.3 Experiment and simulation results under the left-handed circular polarization (a)-(d). (a) Near-field intensity distribution measured by the NSOM. (b) Near-field intensity distribution calculated by the RCWA. The dark spot is clearly observed in both images. (c) E_z distribution of the near-field calculated by the RCWA. The number of node lines is five, which indicates that the topological charge of the SP vortex is $j = 3$. The white arrows in (a)-(c) denote the directions of the rotation of the polarization. (d) Comparison of the intensity profiles. The red dashed line corresponds to the result of the theoretical model i.e., the square of the absolute value of the 3th order Bessel function of the first kind. The blue solid line depicts the field intensity along the dashed line in the NSOM image (Figure 4.3(a)). The black dotted line shows the field intensity along the dotted line in the RCWA image (Figure 4.3(b)).	66
Figure 4.4 Size of the primary ring of the SP vortex as a function of the geometric vortex topological charge m for various types of the polarization states. The straight lines with markers are from the simulation results, whereas the error bars are from the experimental data. The horizontal dotted lines show the sizes of the primary rings from the theoretical prediction given by the Bessel function of the first kind. The topological charge of the SP vortex j is given by $j = m + 1$ for the right-handed circular polarization, $j = m$ for the radial polarization, and $j = m - 1$ for the left-handed circular polarization, respectively.	68
Figure 4.5. Phase profiles of (a) the circular aperture and (b) the annular aperture are shown, where the phase profiles are given by $\exp(i3\varphi)$, where φ as given by $\varphi = \tan^{-1}(y/x)$ varies from 0 to 2π	73
Figure 4.6 The x - z plane cross-sections of (a) the circular aperture and (b) the annular aperture show a slightly diverging profile of the vortex-cone. The x - y plane cross-sections ($z=300\text{ }\mu\text{m}$) of (c) the circular aperture and (d) the annular aperture show vortex profiles with bright thick and thin vortex rings, respectively.	74

Figure 4.7 The phase modulation profiles of the zeroth to the fourth topological charges to be displayed on the SLM and the x - y cross-sections of the corresponding optical field profiles at $z = 0.3$ mm and 0.6 mm are shown.....	75
Figure 4.8 (a) A scanning electron microscopy (SEM) image of the annular aperture inscribed on the silver surface. (b) The overall experimental setup is shown.....	76
Figure 4.9 Experimentally measured optical field profiles at the aperture surface and relatively close and far planes over the aperture surface are displayed.....	77
Figure 4.10 (a) The phase modulation profiles and (b) a CCD image of annular aperture array. (c) The simulation and (d) experimental results of multiple vortex-cones. The right upper vortex-cone denotes the zeroth-order topological charge (no vortex) and the left upper, left lower, and right lower vortex-cones denote the third-order, the fifth-order and the fourth-order topological charges, respectively.....	79
Figure 4.11 (a) ((b) and (c)) The phase profiles to induce the spatial shifting of the vortex-cones, (d) ((e) and (f)) the corresponding simulations, and (g)((h) and (i)) the experiment results. In this experiment, the vortex-cones in the first and third quadrant regions are shifted. The red dotted reference line is drawn for a comparison of the spatial positions of the vortex-cones.....	80

List of Tables

Table 2.1 Geometric parameters of the designed patterns of SP caustic light flows of composite super-formulas.....	23
Table 2.2 Geometric parameters of the designed patterns of SP caustic light flows	23

Contents

Abstract.....	i
List of Figures	iii
List of Tables.....	x
Chapter 1. Introduction	3
1.1. Introduce to surface plasmons.....	3
1.2. Motivation of this dissertation.....	7
1.3. Scope and organization	10
Chapter 2. Generating surface plasmon wave patterns with caustics.....	13
2.1. Inducement of caustics for surface plasmon	14
2.1.1. Introduction of caustics.....	14
2.1.2. Vectorial field model of surface plasmon wave.....	18
2.1.3. Design equations of PCF	20
2.2. Experiment and simulation.....	21
2.2.1. Experimental setup.....	21
2.2.2. Experimental result of the PCF.....	25
2.2.3. Complicated pattern generation by PCF.....	27
2.2.4. Spatial multiplexing of PCFs	33

Chapter 3. Surface vortices with plasmonic lens and helical vector beam.....	36
3.1. Helical vector beam	37
3.1.1. Introduction of helical vector beam	38
3.1.2. SPP excitation at Metal slit	40
3.2. Plasmonic vortex with helical vector beam	41
3.2.1. Phase variation by PVL and HVB.....	41
3.2.2. Plasmonic vortex lens with circular polarized beam.....	44
3.2.3. Simulation result with helical vector beam	51
3.2.4. Fractional plasmonic vortex	54
3.2.5. Orbital angular momentum of the surface plasmon vortex fields	57
Chapter 4. Surface plasmon modulation.....	60
4.1. SP modulation with PVL and circular polarized beam .	60
4.1.1. Experimental setup and method	60
4.1.2. Experimental result	63
4.1.3. Orbital angular momentum of SP vortex	70
4.2. Beam modulation with Annular aperture and HVB	71
4.2.1. Generation and control of a single vortex-cone	72
4.2.2. Generation and control of multiple vortex-cones	78
Chapter 5. Conclusion.....	82
Bibliography	84
한글 초록.....	91

Chapter 1

Introduction

1.1. Introduce to surface plasmons

The interaction between metals and electromagnetic radiation is largely dictated by the free conduction of electrons in the metal. As a consequence, most metals possess a negative dielectric constant at optical frequencies, which causes high reflectivity. Furthermore, at optical frequencies, the metal's free electron gas can sustain surface and volume charge density oscillations, known as plasmon polaritons or plasmons, with distinct resonance frequencies [1]. According to the simple Drude model, at frequencies below the plasma frequency, the optical wave decays with an attenuation coefficient that decreases as the frequency increases, vanishing at the plasma frequency; the free electrons then undergo longitudinal oscillations associated with plasmons [2]. The study of optical phenomena related to the electromagnetic response of metals has recently been termed plasmonics or nanoplasmatics. Bulk metals cannot confine and guide optical waves. At a metal/dielectric interface, however, Maxwell's equations admit solutions in the form of charge-density waves coupled with optical waves, generally referred to as surface plasmon polaritons (SPPs) [3, 4].

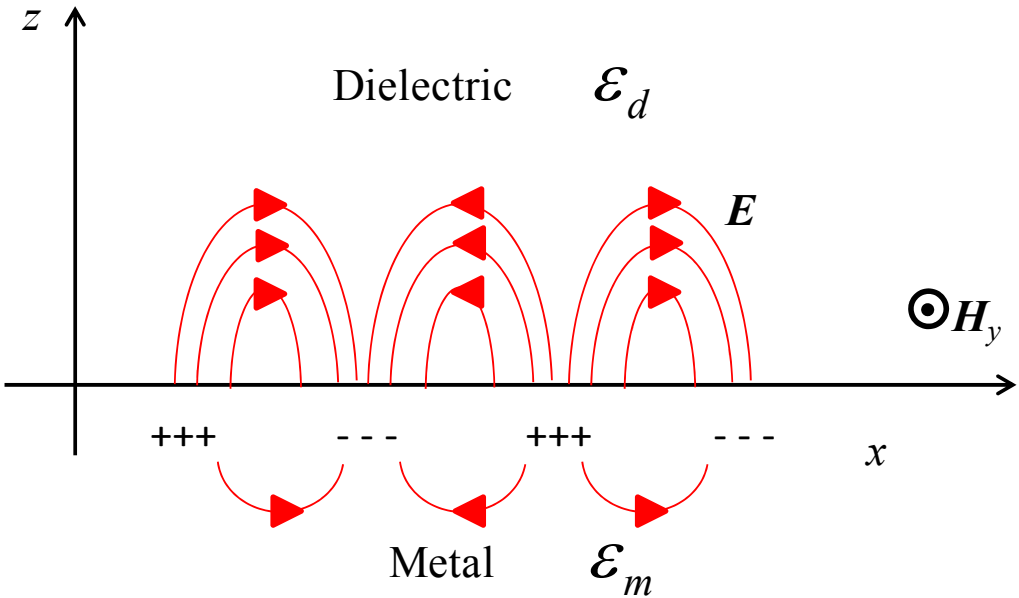


Figure 1.1 Surface plasmons (SPs) at the interface between a metal and a dielectric material have a combined electromagnetic wave and surface charge characteristic. They are transverse magnetic in character (\mathbf{H} is in the y direction), and the generation of the surface charge requires an electric field normal to the surface. This combined characteristic also causes the field component perpendicular to the surface to be enhanced near the surface while decaying exponentially as the distance away from it increases.

SPs are well described by classical electromagnetic theory. There are a set of expressions for surface waves which exist at the plane boundary between two such regions and decay gradually with the distance from the boundary, $z = 0$, in Figure 1.1. The dielectric constant of metal ϵ_m is assumed to be real and negative. For the time being, I assume ϵ_d to be real and positive. The electromagnetic fields are TM-polarized. Thus, the fields are expressed as follows [3]:

$$z \geq 0,$$

$$\begin{aligned} H_y(x, z) &= A \exp(i\beta x) \exp(-k_d z), \\ E_x(x, z) &= -i \frac{k_d}{\omega \epsilon_0 \epsilon_d} A \exp(i\beta x) \exp(-k_d z), \\ E_z(x, z) &= \frac{\beta}{\omega \epsilon_0 \epsilon_d} A \exp(i\beta x) \exp(-k_d z); \end{aligned} \quad (1.1)$$

$$z \leq 0,$$

$$\begin{aligned} H_y(x, z) &= A \exp(i\beta x) \exp(-k_m z), \\ E_x(x, z) &= -i \frac{k_m}{\omega \epsilon_0 \epsilon_m} A \exp(i\beta x) \exp(-k_m z), \\ E_z(x, z) &= \frac{\beta}{\omega \epsilon_0 \epsilon_m} A \exp(i\beta x) \exp(-k_m z). \end{aligned} \quad (1.2)$$

Here, $k_x = \beta + ik_{x,i}$. The dispersion relation for surface waves is obtained from the boundary condition for Eqs. (1.1) and (1.2), as

$$\beta = \frac{\omega}{c} \sqrt{\frac{\epsilon_d \epsilon_m}{\epsilon_d + \epsilon_m}}. \quad (1.3)$$

To display the result, I assume for the dielectric function of the metal according to the Drude model that

$$\epsilon(\omega) = 1 - \frac{\omega_p^2}{\omega^2}, \quad (1.4)$$

where ω_p is the frequency of bulk longitudinal electron excitations, i.e., the plasma frequency. The corresponding dispersion curve is shown in Figure 1.2. The requirement that β be real and positive so that the electromagnetic field of the surface plasmon polariton decay exponentially into the dielectric medium in contact with the metal means that the SPP dispersion curve must lie to the right of the light in the dielectric medium. Consequently, the SPP cannot radiate light into the dielectric medium and cannot be excited with conventional illumination from the adjacent dielectric.

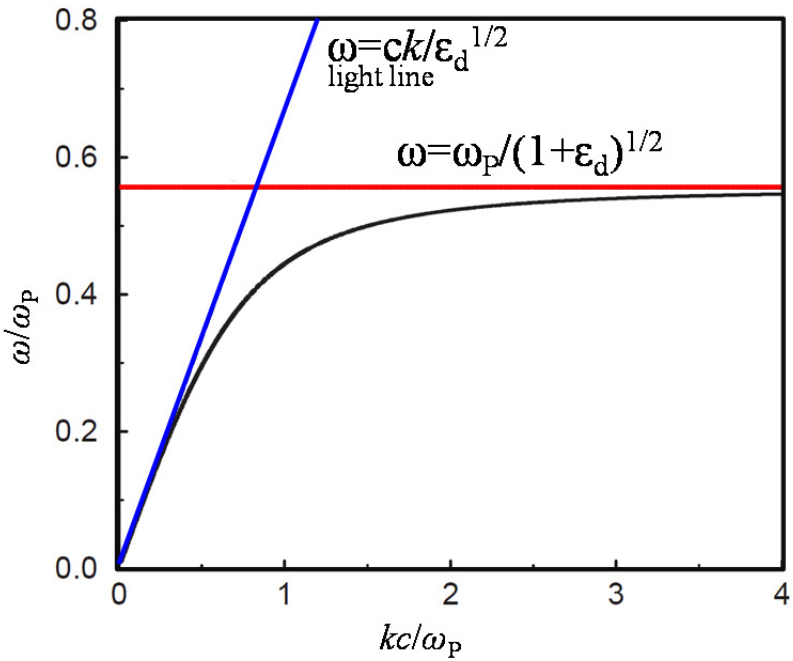


Figure 1.2 Dispersion of SPP at a dielectric–metal interface. Also plotted is the dispersion of light in the dielectric medium, and the corresponding surface plasmon frequency.

Nano-metallic structures have shown optical properties such that they can confine and manipulate light far below the wavelength scale, i.e., the diffraction limit. These remarkable and fascinating characteristics originate from the interaction between the electromagnetic field and free electron oscillation between dielectric and metal surface, known as SPs. The explosion in research on plasmonics stems from the developments of fabrication and measurement nanotechnology. Presently, this research is discovering breakthroughs in nanotechnology with the help of the focused ion beam and the near-field scanning optical microscope [5, 6].

For researchers in the field of optics, one of the most attractive aspects of SPs is the way in which they help us to concentrate and channel light using subwavelength structures. This can lead to miniaturized photonic circuits with length scales much smaller than those currently achieved [7, 8]. Such a circuit would first convert light into

SPs, which would then propagate and be processed by logic elements before being converted back into light. To build such a circuit, numerous components are necessary, including waveguides, switches, and couplers.

1.2. Motivation of this dissertation

An optical modulator is a device which is used to modulate a beam of light. The beam can be carried over free space or propagated through an optical waveguide. Depending on the parameter of a light beam to be manipulated, modulators can be categorized as amplitude modulators, phase modulators, or polarization modulators. The spatial light modulator (SLM), one type of optical modulator, is an object that imposes some form of spatially varying modulation on a beam of light. Usually, an SLM modulates the intensity of the light beam. However, it is also possible to produce devices that modulate the phase of the beam or both the intensity and the phase simultaneously.

One of the most important yet challenging requirements for SPs applications in photonics, opto-electronics, and optical communications is to introduce a means to modulate SPPs. Modulation of SPs has been one of the most important issues in plasmonics because it provides the very fundamental function of imaging. To influence SPs and hence the associated optical properties directly, manipulation of the refractive index of the dielectric medium adjacent to the metal surface is the method of choice. The route to all-optical control takes advantage of the intense nature of confined electromagnetic radiation in nanostructured elements as the stimulus for optically nonlinear dielectrics that are hybridized with a metallic structure [9, 10]. Another technique of fundamental importance in the context of controlling SPP signals is the application of an external electric field [11]. This is especially significant because both plasmonic and electric signals can be guided in the same metallic circuitry. The applied voltage can then be used to exert direct control over an electro-optically active dielectric medium, changing its refractive index and thus creating SPP modes on the metal/dielectric interface.

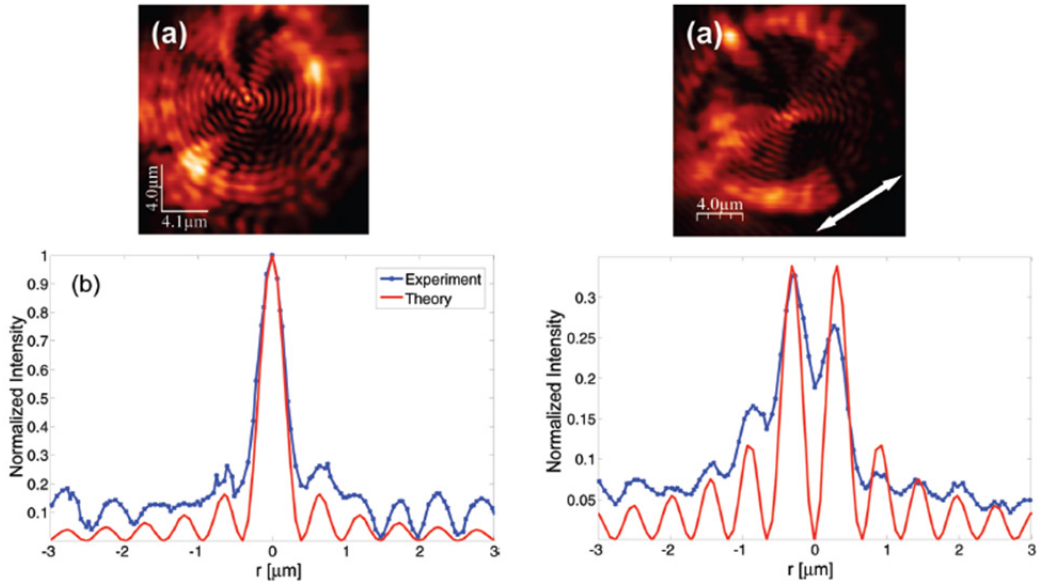


Figure 1.3 NSOM measurement showing SPP focusing in a plasmonic lens illuminated by radially (left) and linearly (right) polarized light. A radially polarized laser generates a single hot spot and a linearly polarized laser generates a double hot spot [15].

Another means of controlling surface plasmon polariton signals is to use a plasmonic lens. A plasmonic lens under linear polarization illumination was proposed to generate a plasmonic hot spot [12]. It was also shown that the position of the hot spot can be tuned by changing the incident angle [13]. An asymmetric plasmonic lens obtained through half wavelength translation was devised to achieve a smaller hot spot [14]. Recently, novel methods to increase the efficiency and uniformity of both hot and dark spots were proposed. An Israeli research group proposed a method to generate both a single hot spot and two hot spots using radial polarization, as shown in Figure 1.3 [15]. By illuminating a radially polarized beam to an annular aperture, a single hot spot is generated. Two hot spots are generated by changing the beam polarization to linear. Another group proposed a method of generating a dark spot and a hot spot by changing the polarization, as shown in Figure 1.4 [16]. The polarization-dependent near-field intensity distribution obtained in previous research is attributed to the presence of a

geometric phase arising from the interaction between light with an anisotropic and an inhomogeneous nanoscale structure.

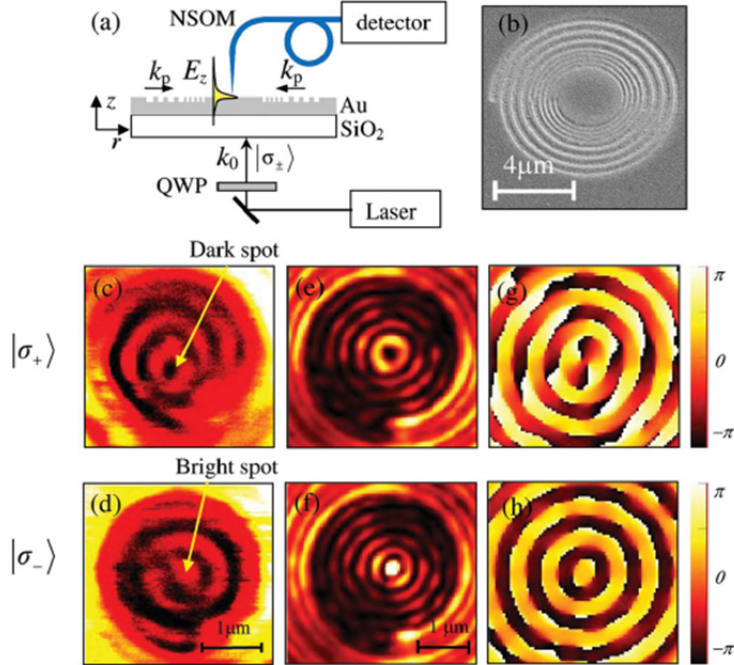


Figure 1.4 Spin-dependent geometric phase in the spiral plasmonic structure [16].

The structure of the plasmonic lens, the initial phase of the SPs at the plasmonic lens structure, and the propagating direction of the SPs are the factors which affect the generated plasmonic patterns. Although the polarization variation alters the initial phase at the plasmonic lens structure, there are limited types of polarization suitable for plasmonic lens. Therefore, the types and size of the shape of the plasmonic pattern is limited in previous research when polarization on a limited plasmonic lens structure varies. This study focuses on the generation of a variety of SPs patterns which can be realized by diversifying the plasmonic lens structures and the initial phase at the lens structure. I will introduce a method to design a plasmonic lens and to vary the initial phase of the SPs. After introducing the generic properties and the design principle of the plasmonic lens inscribed on a thin metal film, I explore various patterns, such as a vortex,

a super-ellipse, arbitrary alphabetical letters, and polygons, as shown in Figure 1.5. A comparative analysis between two-dimensional field distribution based on the proposed plasmonic lens and that from the conventional interference of SPs is also provided.

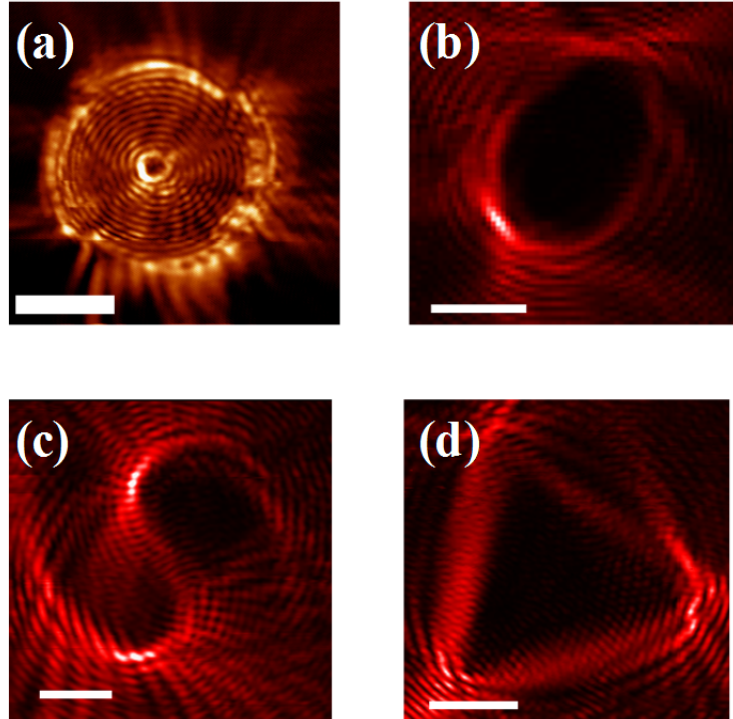


Figure 1.5 Surface plasmon patterns generated by a plasmonic lens are shown: (a) a plasmonic vortex, (b) a super-ellipse, (c) the letter ‘S’, and (d) a triangle

1.3. Scope and organization

Light is an electromagnetic wave that is described as electromagnetic radiation. Electromagnetic waves propagate in the form of two mutually coupled vector waves, an electric-field wave and a magnetic-field wave. Nevertheless, it is possible to describe many optical phenomena using ray optics when light waves propagate through and around objects whose dimensions are much greater than the wavelength. Although the excitation and propagation of SPs are explained in terms of electromagnetic optics, some

pattern generations of SPs can be explained via ray optics. In this dissertation, I will explain SP pattern generation with ray optics first and then explain these concepts in terms of electromagnetic optics.

In free space, the optical lens corresponds to a plasmonic lens. Therefore, the design method of an optical lens is meaningful when designing a plasmonic lens. In ray optics, the image of incident light is determined by the lens structure and the direction of the incident rays. In plasmonics, it is also possible to design a plasmonic lens for a specific plasmonic image by considering the structure of the plasmonic lens and the propagating direction of the SPs. The design method is introduced in Chapter 2. In Chapter 2, SP pattern modulation with caustics, which is explained in terms of ray optics, is addressed. In Section 2.1, the concept of a plasmonic caustic and the related design method are introduced. In Section 2.2, the simulation and experimental results are shown. I report an exploration of the possibility of low-dimensional light field synthesis using a novel device, a plasmonic caustic fociusator, which can generate SP caustic light flows. The generation and control of the SP caustic light flows are experimentally demonstrated.

The ray optics theory used in Chapter 2 is an approximation of electromagnetic theory, in which the wavelength of light is assumed to be zero. As long as the surface plasmon waves propagate through and around a plasmonic structure whose dimensions are much greater than the wavelength, ray theory suffices for describing most phenomena, even if there is some difference in the interpretation when using electromagnetic optics. In the nanostructure of plasmonic lens, however, the wavelength of the surface plasmon is relatively long; hence, the difference becomes more significant. In Chapter 3, I discuss the plasmonic lens and the process of illuminating light with electromagnetic optics. First, in Section 3.1, I introduce the helical vector beam which is used to excite the SP wave on the plasmonic lens. In Section 3.2, I show the simulation results of a variety plasmonic lens structures and instances of illuminated light. The properties of a plasmonic vortex, such as its orbital angular momentum, the size of the vortex, and the topological charge of vortex patterns, are also interpreted.

In Chapter 4, the plasmonic lens is verified with an experiment. In Section 4.1, various plasmonic vortex patterns using circular polarization and plasmonic lens

structures are shown. The experimental result is then compared to a simulation and theory for verification. Far-field beam modulation with a plasmonic lens structure and a helical vector beam is discussed in Section 4.2. I demonstrate how to generate and to control multiple vortex beams. Finally, concluding remarks for this dissertation are provided in Chapter 5.

Chapter 2

Generating surface plasmon wave patterns with caustics

Great efforts have been devoted to controlling low-dimensional light fields. One of those efforts was concentrated on synthesizing and controlling surface plasmon (SP) fields. Conventional approaches are based on forming specific intensity distributions such as hot spots and vortexes. In this dissertation, I show that directionally curved optical power flows can be generated through SP caustics. Light caustic is the curved envelope of concentrated light waves that can take various geometric patterns in nature. The SP caustic light flow proposed in this dissertation is a generalization and enrichment of the recent focusing approaches of SPs with an additional concept of directional power flow control. I devise the plasmonic caustic fouscator for generating plasmonic caustic light flows and demonstrate various curved low-dimensional light power flows experimentally. The plasmonic caustic focusators provide a novel degree of freedom in managing low-dimensional light fields.

2.1. Inducement of caustics for surface plasmon

The field of low-dimensional optics explores the universe and unique characteristics of diverse optical phenomena in low-dimensional space. The control and synthesis of low-dimensional light field has attracted considerable interest recently for a variety of applications including integrated photonics [17], metamaterials [18, 19], bio imaging and sensing [5], nano-metric optical manipulations [20], and nano-scale optomechanics [21]. Even though light field synthesis is now a classical part of optics, a complete understanding of the potential capability of light in synthesizing arbitrary functional patterns in spaces still remains unresolved.

2.1.1. Introduction of caustics

A light caustic is an envelope of concentrated light rays that are produced by the refraction or reflection of light from curved objects or natural processes such as waving water surfaces in a swimming pool as shown in Figure 2.1. In particular, when caustics are generated by natural processes, it is referred to as natural focusing [22]. It is well known that natural caustic patterns are structurally stable under small environmental perturbations, which is in contrast to artificial focusing using lenses with catastrophic instability. Caustic is a general feature of a wave and can be found in various fields of physics. In astrophysics, the discovery of dark matter is closely related to the observation of caustic patterns in sky images that are invoked by a gravitational lensing effect [23].

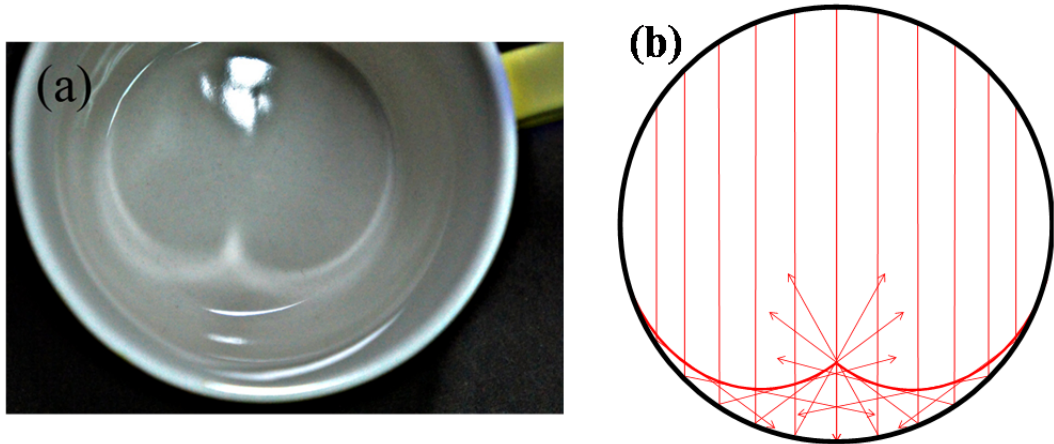


Figure 2.1(a) Caustic network observed inside of cup, (b) schematic of caustic network

In particular, caustic patterns can appear in an SP field confined to low-dimensional space, such as a flat metal surface. SP caustics can be considered as a general class of focused SP fields including previously reported SP hot spots [12, 15, 24, 25] and SP vortexes [26]. When the SP wave is excited simultaneously on a circular slit, the SP wave converges to a single hot spot, while the SP wave generated on a spiral slit pattern forms SP vortex fields. It is expected that the formation of more general SP caustic patterns could be achieved by a proper design of curved slit patterns on a flat metal surface. An additional insight regarding an SP caustic pattern is that it is not just a simple light field pattern but a directional light flow bound on the metal surface accompanying with the Poynting vector stream flowing along the patterned caustic curves, which is supposed to induce various interesting effects such as opto-mechanical forces.

In this dissertation, I report on an exploration on the possibility of low-dimensional light field synthesis using a novel device, a plasmonic caustic fouscator (PCF) that can generate SP caustic light flows. The generation and control of the SP caustic light flows are experimentally demonstrated. This investigation on SP caustic light flow promises to open a new avenue in nanophotonics and to enhance our insights in the essential nature of light fields as well.

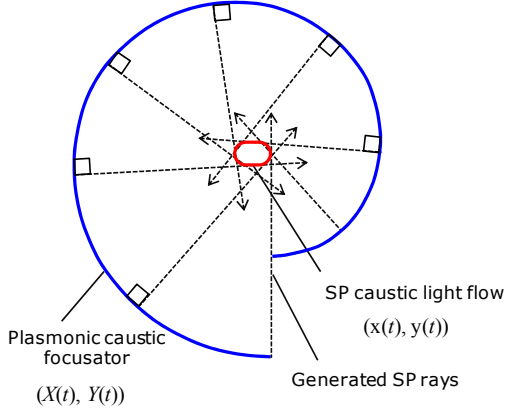


Figure 2.2 Design of the PCF for synthesizing the SP caustic light flow. PCF for a super-ellipse. The SP rays generated at the PCF propagate inward and the envelope of the SP rays forms a super-ellipse-shaped SP caustic light flow. The derivative of the parameterized coordinate $(x(t),y(t))$ of any arbitrary caustic light flow allows for the tangential line, the end point of which results in the trajectory coordinate $(X(t),Y(t))$ of the PCF. The SP rays generated along the PCF are normal to the PCF and tangential to the SP caustic light flow.

Figure 2.2 illustrates the principle of generating SP caustic light flows of a super-ellipse curve with a PCF. The PCF is composed of curved slits sculptured on a metallic film. Under the assumption that the PCF is composed of slowly varying and small curvature curved slits, I can utilize a ray-picture description of SP propagation. Light that is normally incident on the backside of the PCF generates SP rays on the slit pattern that tangentially graze the super-ellipse curve on the front-side of the metallic layer, the envelope of which forms the SP caustic pattern. The PCF and the SP caustic light flow are represented by $(X(t),Y(t))$ and $(x(t),y(t))$, respectively, in Figure 2.2, where t is a parameter that denotes the curve. The geometrical relationship between the PCF and the SP caustic light flow mediated by the SP rays can be intuitively understood as a binding and revolving process of a tight rope around a rigid body whose perimeter represents the

SP caustic light flow. The trajectory of the end point of the rope, $(X(t), Y(t))$, corresponds to the PCF. In this case, the patterns of the SP caustic light flow are inevitably limited to simply connected convex curves.

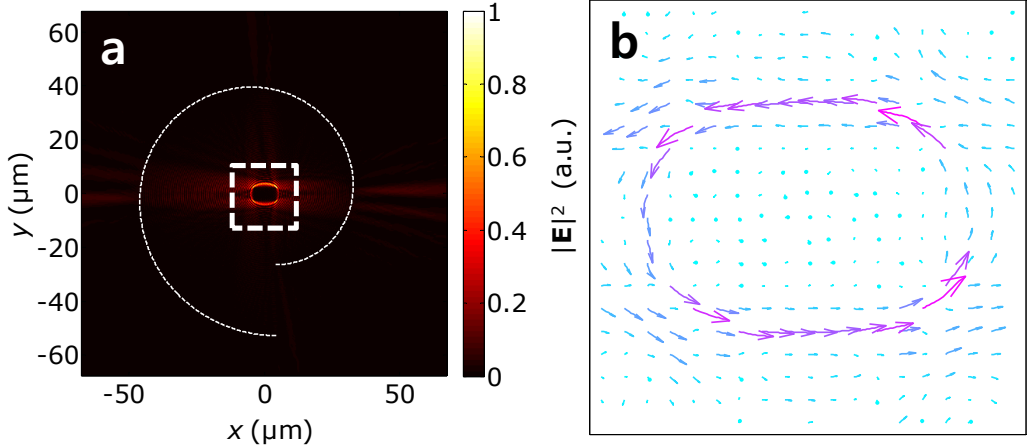


Figure 2.3 (a) Simulation results for the SP caustic light flow. It is assumed that point-source-like Green functions are located along the trajectory of PCF (shown as a dotted white curve). (b) The Poynting vector stream calculated on the PCF surface. The region of interest is presented in (a) as a square with a white dashed line. It is shown that a low-dimensional light energy flow circulates in the counter-clockwise direction along the super-ellipses SP caustic pattern.

The approximated vectorial field model is devised for analyzing the characteristics of the SP caustic light flows. The vectorial Green function of the SP field at the two-dimensional interface is represented with the zeroth order Hankel function of the first kind $H_0^{(1)}(k_{sp}r)$, where k_{sp} and r are the in-plane SP wave number and the distance between the source and the point of observation, respectively. The point-source-like vectorial Green functions of the SP field are continuously arranged on the PCF. (See Section 2.1.2 ‘Vectorial field model of surface plasmon wave’) The coherent superposition of all of the contribution of the SP fields leads to the formation of a super-

ellipse SP caustic field as shown in Figure 2.3(a). More interestingly it can be seen that the optical Poynting vector stream flows uni-directionally along the curve in the counter-clockwise direction, as presented in Figure 2.3(b). This is the reason that the obtained SP caustic field is referred to as an SP caustic light *flow*, which stresses the physics of the low-dimensional directional optical power flow along the curve.

2.1.2. Vectorial field model of surface plasmon wave

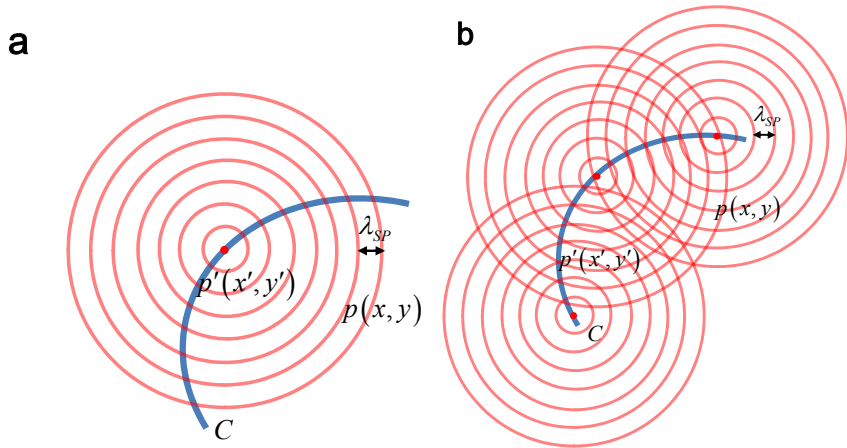


Figure 2.4 (a) Vector Green function of SP field in two-dimensional space and (b) total SP field generated by a PCF represented by the line integral of the vector Green function on the specified curve on the PCF.

To represent the surface plasmon (SP) caustic light flow patterns, a vectorial field model of the SP wave is devised. The scalar wave equation in two-dimensional space (x - y plane) is described by

$$\left(\frac{1}{r} \frac{\partial}{\partial r} \left(r \frac{\partial}{\partial r} \right) + k_{SP}^2 \right) g(r) = -4\pi\delta(r), \quad (2.1)$$

where k_{SP} is the SP wavenumber. It is well known that the Green function of the above wave equation takes the form of the Hankel function;

$$g(r) = j\pi H_0^{(1)}(k_{SP}r). \quad (2.2)$$

Considering the angular spectrum representation of the Hankel function

$$H_0^{(1)}(k_{SP}r) = \frac{1}{\pi} \int_{-\infty}^{\infty} dk_x \frac{\exp(j(k_x x + k_y |y|))}{k_y}, \quad (2.3)$$

where k_x and k_y have the relationship of $k_x^2 + k_y^2 = k_{SP}^2$, I can construct the vector representation of the vector SP point-source on a single interface of metal as shown in Figure 2.4(a). With the vector representation of the SP eigenmode on a single interface of metal, I can straightforwardly obtain the vectorial SP point source representation with the center at the position of (x', y') in the dielectric region ($z > 0$) as

$$\begin{aligned} \mathbf{E}_G(x - x', y - y', z) \\ = jA \frac{k_d}{\omega \epsilon_0 \epsilon_d} H_0^{(1)}(k_{SP} |\rho - \rho'|) e^{-k_d z} \frac{((x - x'), (y - y'), 0)}{\sqrt{(y - y')^2 + (x - x')^2}} - \dots \\ A \frac{k_{SP}}{\omega \epsilon_0 \epsilon_d} H_0^{(1)}(k_{SP} |\rho - \rho'|) e^{-k_d z} (0, 0, 1), \end{aligned} \quad (2.4)$$

$$\mathbf{H}_G(x - x', y - y', z) = AH_0^{(1)}\left(k_{SP}\sqrt{(x - x')^2 + (y - y')^2}\right) e^{-k_d z} \frac{(-(y - y'), (x - x'), 0)}{\sqrt{(y - y')^2 + (x - x')^2}}, \quad (2.5)$$

where \mathbf{E}_G and \mathbf{H}_G are the electric field and magnetic field, respectively, and k_d is the wavevector component perpendicular to the metal surface. In profiling the SP caustic light flows, the developed vectorial field model is applied according to the Huygens' principle as illustrated in Figure 2.4(b). Infinite number of point sources are arranged on the slit pattern and the total SP field generated by the slit is represented by the following line integrals along the curve of PCF denoted by C ,

$$\mathbf{H}(x, y, z) = \oint_C \mathbf{H}_G(x - x', y - y', z) dl', \quad (2.6)$$

$$\mathbf{E}(x, y, z) = \oint_C \mathbf{E}_G(x - x', y - y', z) dl'. \quad (2.7)$$

The time-averaged Poynting vector stream \mathbf{S} is computed by the formula

$$\mathbf{S} = \frac{1}{2} \operatorname{Re} \{ \mathbf{E} \times \mathbf{H}^* \}. \quad (2.8)$$

2.1.3. Design equations of PCF

The mathematical relationship between the pattern of the PCF $\mathbf{S}(t) = (X(t), Y(t))$ and the corresponding SP caustic light flow $\mathbf{s}(t) = (x(t), y(t))$ is given by

$$\mathbf{S}'(t) \bullet \mathbf{s}'(t) = 0, \quad (2.9)$$

where the prime denotes the derivative with respect to the parameter t and \bullet is the inner-product operation. The pattern of the PCF, $\mathbf{S}(t)$, is represented as

$$\mathbf{S}(t) = \mathbf{s}(t) + \gamma(t) \mathbf{s}'(t). \quad (2.10)$$

The differential relationship indicates that the tangential vectors of the SP caustic slit and the SP caustic flow are orthogonal to each other. The condition that the tangential vectors of the coordinates of the PCF and the caustic curve are normal to each other leads to the differential equation of $\gamma(t)$ as

$$\begin{aligned} 0 &= \mathbf{S}'(t) \bullet \mathbf{s}'(t) \\ &= ((x + \gamma x')', (y + \gamma y')') \bullet (x', y') \\ &= [(x')^2 + (y')^2] \gamma' + [x' x'' + y' y''] \gamma + [(x')^2 + (y')^2]. \end{aligned} \quad (2.11)$$

Then $\gamma(t)$ is obtained by

$$\gamma(t) = -\frac{\int_{t_0}^t \sqrt{(x')^2 + (y')^2} dt - \gamma(t_0) \sqrt{(x')^2 + (y')^2}}{\sqrt{(x')^2 + (y')^2}}, \quad (2.12)$$

where the initial value of $\gamma(t)$ is given by $\gamma(t_0) = R_1$. The pattern of the PCF is represented by

$$\mathbf{S}(t) = \mathbf{s}(t) + \left\langle \bar{\gamma}(t) \frac{x'(t)}{\sqrt{(x'(t))^2 + (y'(t))^2}}, \bar{\gamma}(t) \frac{y'(t)}{\sqrt{(x'(t))^2 + (y'(t))^2}} \right\rangle, \quad (2.13)$$

where $\bar{\gamma}(t)$ is given by

$$\bar{\gamma}(t) = - \int_{t_0}^t \sqrt{(x')^2 + (y')^2} dt + \gamma(t_0) \sqrt{(x')^2 + (y')^2}. \quad (2.14)$$

A circularly polarized beam was used to enhance the uniformity of the SP intensity generated from the SP caustic slit. The initial phases of the SPs excited on the PCF depend on the azimuthal angle of the slit with respect to the origin and the direction of rotation of the circularly polarized beam. Therefore, it is necessary to compensate for this polarization dependent initial phase distribution. Finally, the design equation of the PCF, $\mathbf{S}(t)$, is represented as

$$\mathbf{S}(t) = \mathbf{s}(t) + \bar{\gamma}(t) \frac{d\mathbf{s}}{dt} / \left| \frac{d\mathbf{s}}{dt} \right| + l \cdot \left[\frac{\lambda_{SP} \cdot \phi(t)}{2\pi} \right] (\cos \phi(t), \sin \phi(t)), \quad (2.15)$$

where λ_{SP} is the effective SP wavelength and $\phi(t)$ is the azimuthal angle with respect to the origin. Here, the second term plays a role of the radial shift in the PCF to compensate the effect of the circularly polarized beam. l is -1 for the right-handed circularly polarized beam, whereas l is +1 for the left-handed circularly polarized beam.

2.2. Experiment and simulation

The generation and control of the Poynting vector streams of focused SP caustics in low-dimensional space are experimentally demonstrated. This investigation of SP caustic light flow promises to open new avenues in nanophotonics and to enhance our insights in the essential nature of light fields as well.

2.2.1. Experimental setup

Figure 2.5 summarizes the experiment setup used in this study. A thin silver film with a thickness of 300 nm was deposited on a fused silica wafer by evaporation technique. Tolerance of thickness is about 5 nm, however this degree of tolerance is not appending the shape of SP pattern. By the simulation, the shape is almost same under 20 nm tolerance. The PCF producing the super-ellipse SP caustic light flow was designed. The geometric parameters of this pattern are listed in Tables 2.1 and 2.2.

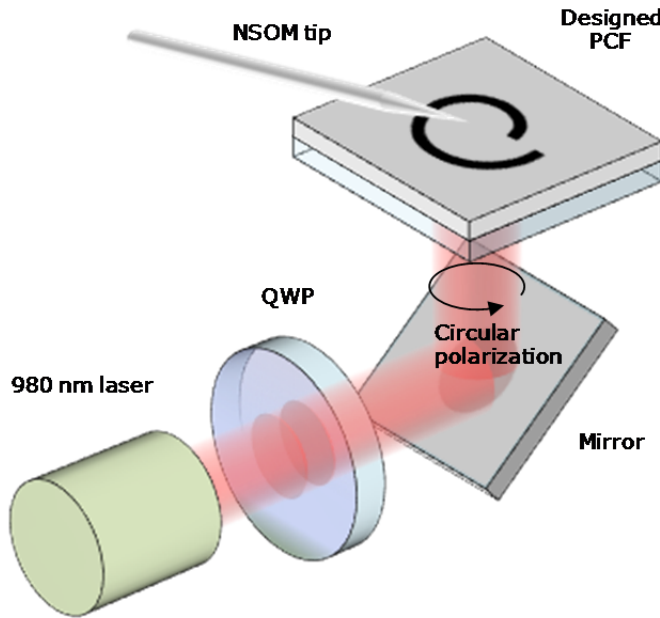


Figure 2.5. Schematic diagram of the NSOM measurement setup. The PCF on the silver film evaporated on the fused silica substrate is illuminated from the back side by a circularly polarized laser beam with a wavelength of 980 nm. The near-field distribution near the center is collected through the aperture in the NSOM tip.

I used the super-ellipse as an elementary pattern for constituting complex patterns of SP caustic light flows. The super-ellipse curve is mathematically represented as

$$(x(\theta), y(\theta)) = \left(\operatorname{sgn}(\cos \theta) a |\cos \theta|^{2/m}, \operatorname{sgn}(\sin \theta) b |\sin \theta|^{2/n} \right), \quad (2.16)$$

where $\operatorname{sgn}(a)$ is the sign function of a real number a . With the parameters, $a, b, m, n, \theta = (t_0, t_f)$, and $\gamma(t_0)$, I can specify the pattern of the target SP caustic light flow and the suitable PCF using the design equation of Eq. (2.15). Table 2.1 shows the geometric parameters $a, b, m, n, \theta = (t_0, t_f)$, and $\gamma(t_0)$ used in this dissertation.

Table 2.1 Geometric parameters of the designed patterns of SP caustic light flows of composite super-formulas

Designed pattern	a	b	m	n_1	n_2	n_3
Triangle	1.5	1.5	3	1	4	4
Square	2	2	3	3	2	2
Pentagon	2	2	3	3	2	2

Table 2.2 Geometric parameters of the designed patterns of SP caustic light flows

Designed pattern	a	b	m	n	(t_0, t_f)	$\gamma(t_0)$
Super-ellipse	4.5 μm	3 μm	3	3	$(0, 2\pi)$	51 μm
Letter ‘S’	Upper part (curve 1)	4.5 μm	3 μm	3	3	$(\pi/6, 3\pi/2)$
	Upper part (curve 2)	4.5 μm	3 μm	3	3	$(7\pi/6, 5\pi/2)$

In addition, I can employ a more elaborate curve segment, the super-formula. This curve can be regarded as the generalized form of the super-ellipse and is represented in the polar coordinate system by

$$r(\theta) = \left(|\cos(m\theta/4)/a|^{n_2} + |\sin(m\theta/4)/b|^{n_3} \right)^{-1/n_1}, \quad (2.17)$$

where r and θ are radius (in μm) and polar angle (in radian), respectively. In this case, the geometric parameters of the super-formulas are a , b , m , n_1 , n_2 , and n_3 . Table 2.2 represents the values of these parameters used in this dissertation.

The detail fabrication and measurement processes are described in the following. To increase the adhesion of Ag, a 20 nm layer of Cr was evaporated on a fused silica wafer with a refractive index of 1.5 and a thickness of 0.5 mm by an electron beam evaporator (Korea Vacuum Tech, KVE-3004). A 300 nm-thick-layer of Ag was then evaporated on the Cr layer by using the same electron beam evaporator. The caustic slit patterns were inscribed on the Ag/Cr layer by focused ion beam (FIB: FEI, Quanta 200 3D). The acceleration voltage of the ion beam was 30 kV and the current was 0.5 nA. The slit width was set to 1450 nm. This is because the maximum SP excitation efficiency occurs at the slit width of $(q - 0.5)\lambda_{SP}$, where q is positive integers ($q = 1, 2, 3, \dots$) [27,28]. Here the free space wavelength λ_0 is 980 nm and corresponding SP wavelength λ_{SP} along the interface between silver and free space is 969 nm. This pattern was inscribed on the silver film using FIB equipment. A scanning electron microscope (SEM) image of this is shown in Figure 2.6.

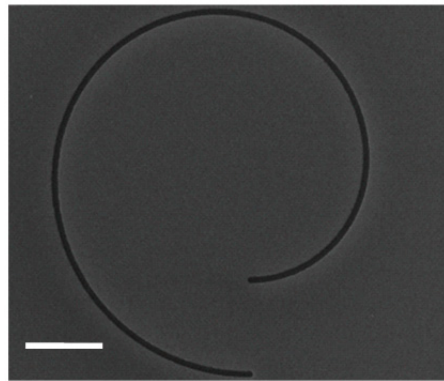


Figure 2.6. SEM image of the PCF producing a super-ellipse SP caustic light flow. The scale bar is 20 μm .

In the design of the PCF, the radial shift of the PCF segments was taken into account to compensate for the effect caused by the phase retardation due to the use of the circular polarization state (See Section 2.1.3 ‘Design equations of the PCFs’).

The sample was illuminated from the bottom by a laser with a free space wavelength of 980 nm (Newport, LQA980-220E). A quarter waveplate was located between the laser source and the target sample to produce a circularly polarized beam for uniform excitation of the SP at the PCF. The distribution of the SP evanescent field intensity was measured by means of near-field scanning optical microscope (NSOM: Nanonics, Multiview 4000). The SP field inside the PCF was detected by a cantilever type metal-coated (Cr/Au) NSOM tip with an aperture diameter of 250 nm, which was holed on the end of the tapered multimode fiber (UV 50). The feedback mode in the NSOM system I used was the noncontact intermittent mode (or tapping mode), in which the tip is tapping over the sample and touches it with the resonance frequency of the tip during the scan. The main benefit of this mode is that there is less chance of damaging the sample or tip compared with the contact mode while the tip is in sufficiently close proximity (\sim 50–100 nm) to the sample to detect the SP field, the decay length of which was \sim 2.08 μm at the operating wavelength used (980 nm). An avalanche photo-diode (APD) (Agilent, Agilent 81634B) with a power range of +10 to -110 dBm was used to convert the intensity of the light transmitted by the optical fiber into an electric signal.

2.2.2. Experimental result of the PCF

Figure 2.7 shows a charge-coupled device (CCD) image of the PCF under a backside illumination. The distribution of the SP field in the local region measured by the NSOM that is indicated by the white dashed rectangle in Figure 2.7 is shown in Figure 2.8. The scanned region does not include the SP slit and only the field distribution near the center of the geometry is shown, since the maximum size of the scanning window of the NSOM probe is limited to 33 μm by 33 μm .

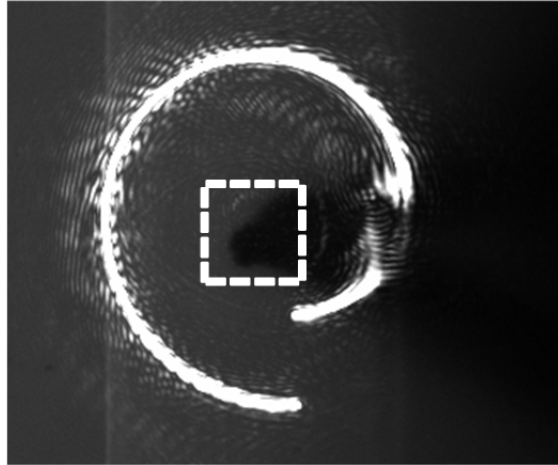


Figure 2.7 CCD image of the PCF under the illumination of the circularly polarized light beam and the bright curve observed in the CCD image corresponds to the transmitted light through the designed slit. The dark shadow near the center is the shadow of the NSOM tip approaching the metal film. The rectangle with the white dashed lines shows the scanned window.

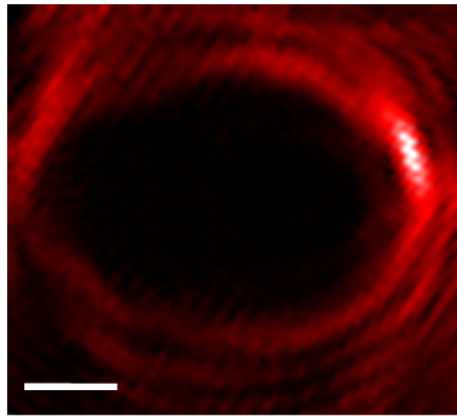


Figure 2.8 The NSOM image near the center of the configuration. The scale bar in the NSOM image corresponds to 2.5 μm . The NSOM image of the super-ellipse with a major axis of 9 μm and a minor axis of 6 μm can clearly be observed.

As shown in Figure 2.8, the super-ellipse pattern of SP caustic light flow can be clearly observed with a dark area at its center. The fringe pattern outside the caustic curve is attributed to optical interference of the counter-propagating SPs.

2.2.3. Complicated pattern generation by PCF

Meanwhile, an SP caustic light flow with a more complicated pattern can be synthesized by the spatial multiplexing of PCF segments. This approach is based on the notion that a segment of caustic light flow can be smoothly connected to another segment of caustic light flow generated by a different PCF segment. A complicated caustic curve shown in Figure 2.9 can be seen as a composite curve formed by the continuous connection of a set of convex and concave curved segments. The connection boundary is an inflection point between concave curve and convex curve arranged along the caustic curve. The SP caustic light flow can be divided into several segments in such a way that each segment does not impart any inflection point. The corresponding PCF segments for the curved partial segment of the SP caustic light flow are separately obtained and implemented simultaneously in one plane. I refer to this strategy as the spatial multiplexing of PCFs. For example, the letter ‘S’, the PCF pattern of which is illustrated in Figure 2.10, is composed of the upper and lower parts. The upper and lower PCFs are wound counter-clockwise and composed of the partial super-ellipse with respective range of parameters denoted by (t_o, t_f) .

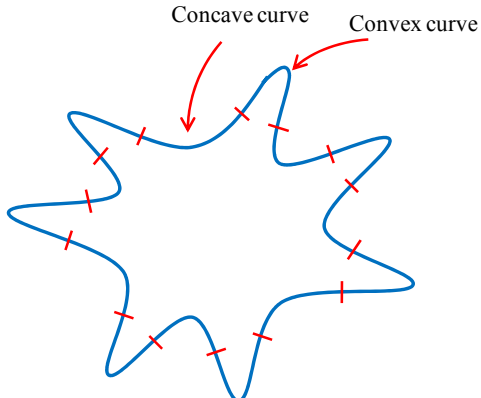


Figure 2.9 SP caustic light flows with spatial multiplexing. Composite caustic pattern composed of continuous arrangement of several partial caustic curves. The SP caustic light flow patterns can be divided into multi segments in such a way that there is no inflexion point in each segment.

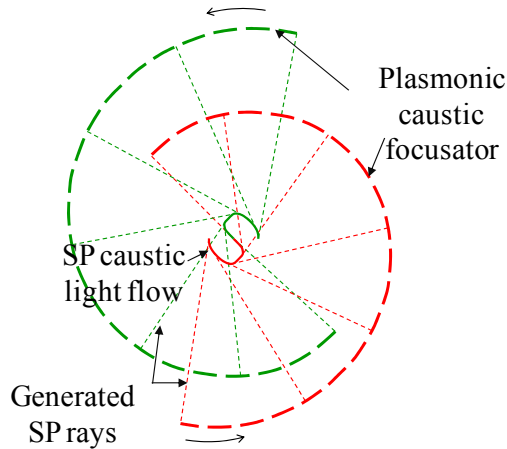


Figure 2.10 Spatial multiplexing of the multi-segment SP caustic light flows. An example of the ‘S’-shaped SP caustic light flow is presented. The upper curve of the ‘S’ letter, denoted by the solid green line, is generated by the left bottom arc of the PCF (the dashed green line), whereas the lower curve (the red solid line) corresponds to the right upper arc of the PCF (the dashed red line). The arrows at the PCF arcs denote the directions for a hypothetical binding process of a tight rope in the design of the PCF.

The exemplary composite PCFs demonstrated in this dissertation are presented in Figure 2.11. The specific design parameters for the letter ‘S’ are presented in ‘Design parameters’ in the method section. The spatial multiplexing technique can also be extended to produce SP caustic light flows of various polygon patterns, such as a triangle, a square, and a pentagon. The designs of the PCFs for these patterns are presented in Figure 2.11. In order to describe more complicated segments, I employ the super-formulas for polygons (See the ‘Design equations of PCF’ in the Section 2.1.3.). In the design of a triangle, a square, and a pentagon, the rope length $\bar{\gamma}(t)$ in Eq. (2.12) is adaptively changed at the inflection points to represent the designed caustic pattern. Those PCFs are wound clockwise. As a result, the PCF of the triangle is composed of six pieces of PCF segments as shown in Figure 2.11(b). The six values of $\bar{\gamma}$ at the six respective connection boundaries including the initial rope length are set to 68, 72, 68, 72, 68, and 72 μm , respectively. The three blue curves and red curves in Figure 2.11b are in charge of the curves around three apex points and around three edges of the triangle, respectively. For the square, eight pieces of PCF comprise the composite PCFs as presented in Figure 2.11(c). The eight lengths of the values of $\bar{\gamma}$ at the points of inflection are set to 68 μm and 72 μm in turns in a similar manner to the triangle. For a pentagon, ten pieces of PCF segments constitute the composite PCFs as presented in Figure 2.11d. The ten lengths of the values of $\bar{\gamma}$ are also set to 68 and 72 μm , alternatively.

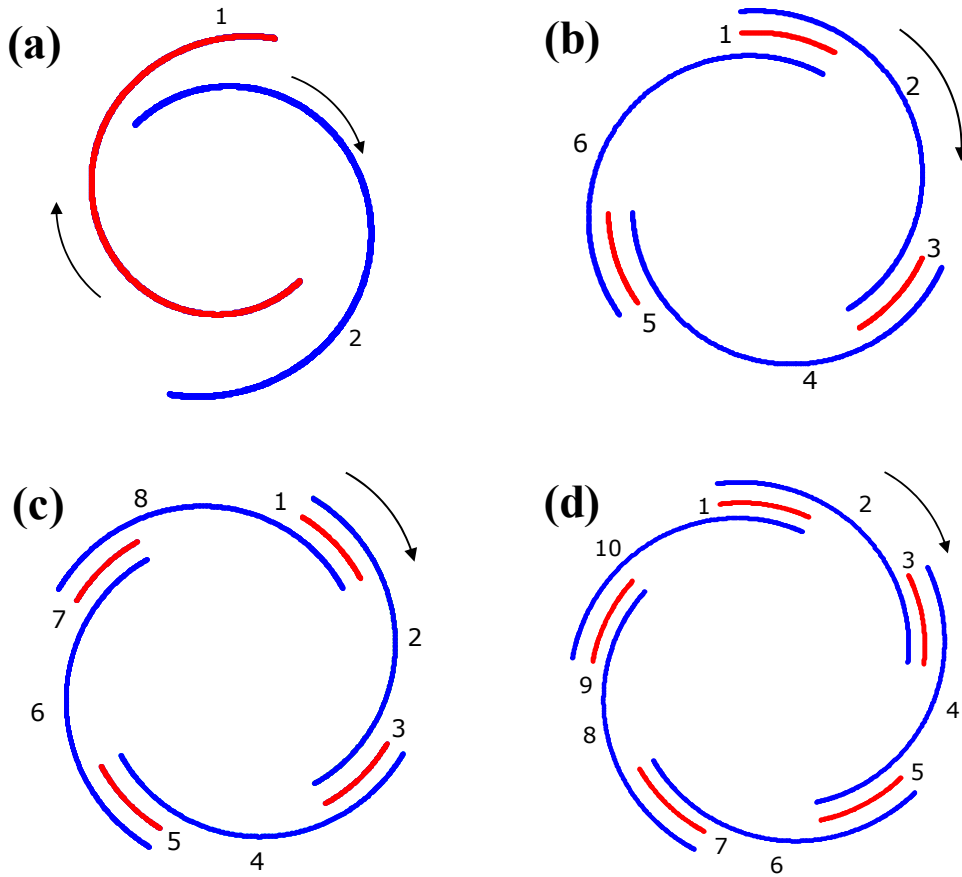


Figure 2.11 PCF patterns for (a) letter ‘S’, (b) triangle, (c) square, and (d) pentagon. Since the SP caustic flow light with straight line patterns cannot be implemented, the apex and edge of polygons are expressed as convex and concave super-formula curves, respectively.

It is experimentally demonstrated that the spatial multiplexing of PCF segments can produce arbitrarily patterned SP caustic light flows. A SEM image of the PCF designed to synthesize the SP caustic light flow in the form of a capital letter ‘S’ is shown in Figure 2.12(a). The total PCF is composed of two curved partial PCF segments. The NSOM measurement results and simulation results of the SP field distribution are shown in Figure 2.12(b) and (c), respectively. With the backside illumination of light, a capital ‘S’ appears at the center of the structure. The measured NSOM results are in good agreement

with the simulation results. The scale bars in the simulation and experimental results correspond to a length of 5 μm in common. The Poynting vector stream flowing outward from the center of the ‘S’ along the curved paths is shown in Figure 2.12(d). The standing wave interference pattern is observed around the center of the ‘S’ due to two counter-propagation Poynting vector streams. In this spatial multiplexing of two separate PCF segments, the SPs generated from one slit segment inevitably propagate over the other slit segment. An analysis of the effect of phase retardation that SPs experience when crossing over the slit segment can be found in Section 2.2.4 ‘Spatial multiplexing of PCFs’. It turned out that, in the case of the PCF design, the effect of phase retardation experienced by the SP crossing a slit segment on the formation of caustic flow is negligible. It should also be noted that the effect of this small perturbation in the formation of an SP caustic light flow is not significant, because of the structural stability of the caustics [22].

In Figure 2.12, the examples of PCFs generating SP caustic light flow patterns of polygons such as a triangle (Figure 2.12(e) – (h)), a square (Figure 2.12(i) – (l)), and a pentagon (Figure 2.12(m) – (p)) are shown with experimental and simulation results. In practical design, the corners of each polygon of the caustic light flow are designed by slightly convex lines and the edges are described by means of slightly concave lines. By properly arranging separate segments of corners and edges, and their directions, SP caustic light flow patterns with directional Poynting vector streams can be produced. The simulation results shown in the third and fourth column panels of Figure 2.12 confirm the aforementioned design principles. Experimental demonstrations on the SP caustic light flows of the polygons are shown in the second column panels in Figure 2.12. As can be seen, the experimental results are in good agreement with the theory and simulation results. Developed PCFs composed of spatially multiplexed PCF segments are successfully demonstrated by the synthesis of complicated curved SP caustic light flows.

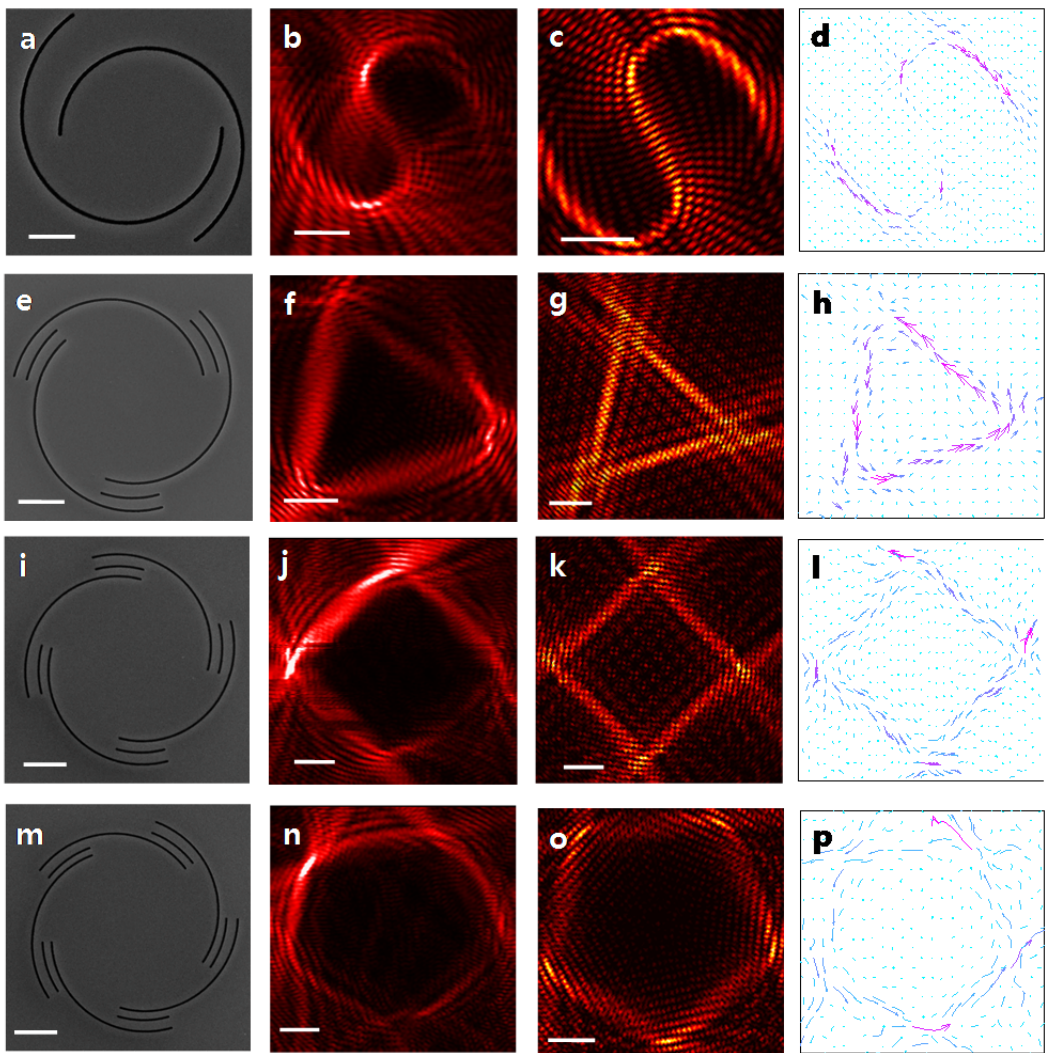


Figure 2.12 Synthesis of arbitrary SP caustic light flows. (a)–(d) Caustic light flow for the letter ‘S’. (e)–(h) Caustic light flow for a triangle. (i)–(l) Caustic light flow for a square. (m)–(p) Caustic light flow for a pentagon. (a), (e), (i), and (m) are the SEM images and the scale bars correspond to 30 μm . (b), (f), (j), and (n) are the experimental results of the NSOM measurement and the scale bars are 5 μm . (c), (g), (k), and (o) are the simulation results and the scale bars denote the length of 5 μm . (d), (h), (l), and (p) are the Poynting vector streams calculated on the PCF surface.

2.2.4. Spatial multiplexing of PCFs

This treatment of the spatial multiplexing also brings a complicated situation that there must be elementary PCFs intersecting the path of propagating SP waves generated by relatively rear-positioned elementary PCFs. Thus the SP waves generated by the rear-positioned PCFs must cross over the dielectric gap (or air gap) of the fore-positioned PCFs as illustrated in Figure 2.10. It is thus necessary to analyze the transmission characteristics of the SP wave crossing over the dielectric gap. As seen in Figure 2.13(a), the z -directional electric field component of the SP wave with an oblique angle of θ crossing in an air gap of the PCF structure is represented as

$$E_z(x, y) = E_0 \exp(j(k_{SP} \cos \theta x + k_{SP} \sin \theta y)). \quad (2.18)$$

At the metal surface ($z = 0$), the z -directional electric field distributions of the SP wave at the left interface ($x = 0$) and the right interface ($x = d$) of the air gap are represented, respectively, by

$$E_z(0, y) = E_0 \exp(jk_{SP} \sin \theta y) \quad (2.19)$$

and

$$E_z(d, y) = TE_0 \exp(jk_{SP} \cos \theta d) \exp(jk_{SP} \sin \theta y), \quad (2.20)$$

where T is the complex transmission coefficient of the SP wave crossing over the air gap.

If there is no air-gap, the electric field distribution at $x=d$ of the SP wave that propagated on the flat surface of the metal is given by

$$E_z(d, y) = E_0 \exp(jk_{SP} \cos \theta d) \exp(jk_{SP} \sin \theta y). \quad (2.21)$$

The transmission efficiency and the phase delay are defined, respectively, by $|T|^2$ and $\psi = \text{angle}(T)$. The phase and amplitude changes of an incident SP wave are dependent on its incident angle θ and slit width. The transmission characteristics of surface plasmon crossing in a metal gap are analyzed using the rigorous coupled-wave analysis (RCWA) [29–31]. The simulation parameters are denoted in Figure 2.13(a). The values of the relative permittivity of silver, glass substrate, and air are $\epsilon_m = -43.7249 + 2.7427i$, $\epsilon_s = 2.25$, and $\epsilon_{air} = 1$, respectively. The analysis shown in

Figure 2.13(b) and (c) reveals that, within the range of incidence of 0° to 30° , the transmission efficiency is in the range of 50–57% and the phase delay is less than 0.31 rad. The phase delay is negligible in the design of the composite PCFs where the SP waves intersected the PCF segments with the intersection angles less than about 10 degrees. Thus any additional compensation technique of the phase delay was not considered in the composite PCF design.

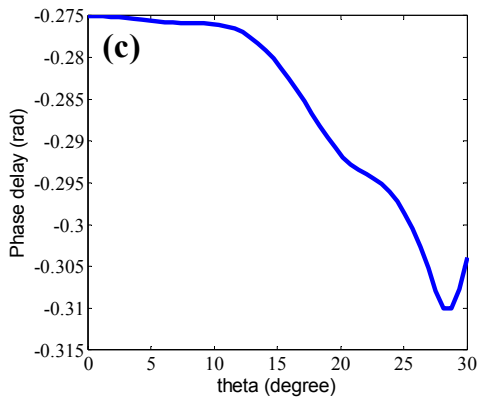
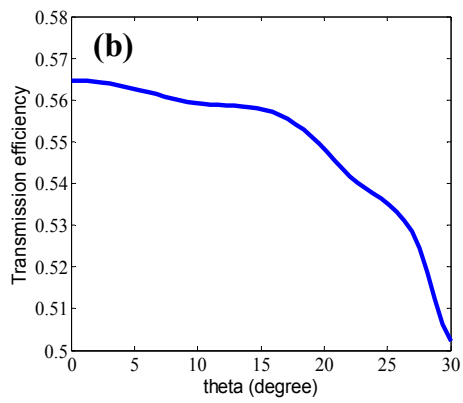
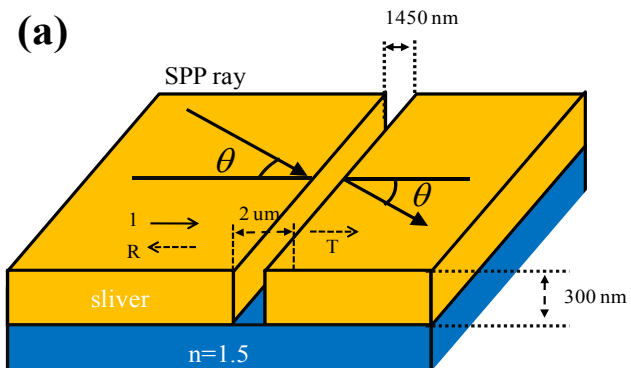


Figure 2.13. (a) SP wave crossing over the metal gap with an incidence angle of θ . (b) transmission efficiency and (c) phase delay for various incidence angles.

Chapter 3

Surface vortices with plasmonic lens and helical vector beam

I present that two distinct optical properties of light, the spin angular momentum (SAM) and the orbital angular momentum (OAM), can be coupled in the plasmonic vortex. If a plasmonic vortex lens (PVL) is illuminated by the helical vector beam (HVB) with the SAM and OAM, then those distinct angular momenta contribute to the generation of the plasmonic vortex together. The analytical model reveals that the total topological charge of the generated plasmonic vortex is given by a linear summation of those of the SAM and OAM, as well as the geometric charge of the PVL. The generation of the plasmonic vortex and the manipulation of the fractional topological charge are also presented.

Helical vector beam with two angular momenta is treated in Section 3.1. Fundamental principles of generation of surface plasmon (SP) and the effect of the helical vector beam on SPs are explained. The principal wave function of the dominant electric field is discussed. The direction and phase relationship of SPs over the diffractive slit are also discussed. The dependence of the phase and the polarization state of the incident beam and the geometric translation of the diffractive metal slit is also described. In Section 3.2, general properties of the plasmonic vortex such as the topological charge

dependence on the polarization state of incident light and the primary ring size are covered. It turns out that the rotating phase distribution results in the plasmonic vortex with the wave function form in the evanescent Bessel beam.

3.1. Helical vector beam

The local excitation of SPs is one of the fundamental elements in plasmonics, for which nano-holes, nano-slits, and curved nano-slits are normally used. Besides, nano-particles, channel waveguides, and surface gratings can also be used for local excitation of SPs. The combination of these SP generators can generate various useful SP interference patterns on metal/dielectric interfaces. The interferometric or diffractive SP pattern generation is a fundamental research area of plasmonics initiated very recently. Although research on SP patterning started from the formation of SP focal spots, namely, hot spots on a subwavelength scale, diffractive synthesis of complex SP fields as well as single hot spots and dynamic control of SP fields for various applications appear in the front of plasmonics research.

Considerable research has been devoted to fundamentals and applications for SP interference pattern based on the angular momenta of light [32–37]. SAM resides in the circularly polarized beam, whereas OAM comes from the spiral phase profile of beam around the axis of propagation. Although there are a few researches about the coupling of the PVL and each of the angular momentum [38], discussion on the overall effect of the SAM, the OAM and the geometrical charge of the PVL to the plasmonic vortex has not yet been established.

In this section, the overall effect of two angular momenta and the PVL structure on SP interference patterns is examined. Explanations on the HVB with two angular momenta are given. I propose a method to generate the plasmonic vortex with arbitrary topological charge, synthesized with momenta of HVB and geometrical effect of PVL. It is shown that effects of the SAM and the OAM of light can be coupled in the plasmonic vortex.

3.1.1. Introduction of helical vector beam

The electromagnetic field component of an HVB has an azimuthal phase term of $\exp(il\phi)$. Here, l is the helix winding number of 2π cycles in phase around the circumference. Light with the helix winding number l is regarded as a flux of photons with the OAM $l\hbar$. This azimuthal phase distribution can be obtained by the spiral phase plate or the spatial light modulator (SLM). Note that the positive and negative signs of l correspond to the direction of counter-clockwise and clockwise rotating electromagnetic fields, respectively. There are various kinds of optical beam with helicity such as the Laguerre-Gaussian beams and the Bessel beam [39].

The transverse field of light can be expressed as a superposition of two orthogonal electric fields. Depending on the amplitude and phase relationship between them, various polarization states can be obtained such as linearly, circularly, and elliptically polarized beams. Those states are achieved by using the half- or quarter-wave plates. Especially, the circularly polarized beam is considered to have the SAM of $\sigma = s\hbar$, where $s = +1$ for the right-handed circular polarization (RCP) and $s = -1$ for the left-handed circular polarization (LCP), respectively [16]. There are other nonconventional polarization states of light that have the electric field direction with spatial dependence, such as radially and azimuthally polarized beams [16]. Corrugated surface gratings or specific polarizer can be used to generate those polarization states of light [40]. The magnetic fields of radially and azimuthally polarized beams are determined to be orthogonal to the electric fields, so that the resultant magnetic fields are azimuthally and radially polarized, respectively.

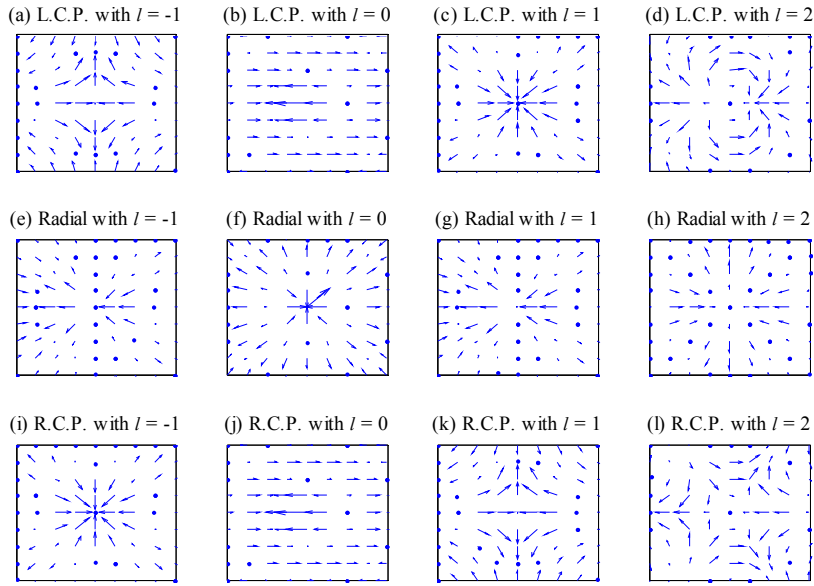


Figure 3.1 Electric field distributions at a fixed time for various combinations of polarization states and helix winding numbers (Top panel: the LCP, middle panel: the radial polarization, bottom panel: the RCP). The helix winding number l varies from -1 to 2 with increment of 1.

The two properties of light mentioned above can be combined together, leading to the HVB. In particular, the phase and polarization state can be independently controlled to have arbitrary combinations by cascading wave plates and spiral phase plates. Figure 3.1 represents electric field distributions at a fixed time for various combinations of polarization states and helix winding numbers. The top panel corresponds to the LCP, the middle the radial polarization, and the bottom the RCP. From the left panel, the helix winding number l varies from -1 to 2 with increment of 1. The abscissa and the ordinate denote the x and y coordinates with arbitrary unit, respectively. In addition to the polarization factor, the azimuthal phase term of $\exp(il\phi)$ is multiplied as well as the radial term of $J_j(\rho)$, where J_j and ρ are the j th-order Bessel function with the first kind and the radial coordinate ($\rho = (x^2 + y^2)^{1/2}$). Even though the polarization is different for each panel, they look quite similar in some cases. For example, the LCP with $l = 1$

(Figure 3.1(c)), the radial polarization with $l = 0$ (Figure 3.1(f)), and the RCP with $l = -1$ (Figure 3.1(i)) look similar at a fixed time. However, the field distributions with time development show definitely unique patterns. It will be shown below that there are such combinations that result in the same topological charges due to coupling of the spin and angular momenta in the PVL. From these observations, an important remark can be made that the polarization states and helix winding number of phase can be separately manipulated so that I obtain any arbitrary combination of SAM and OAM.

3.1.2. SPP excitation at metal slit

Now let us discuss about the excitation mechanism of SPs based on the subwavelength metal slit. When the slit is illuminated by light from one side of metal, light passing through the slit excites SP wave on the other side. I note that the normal incidence of light induces the equal phase distribution of electron oscillations across the slit and thus the propagation direction of SPs generated by slit is always perpendicular to the slit. The electric field component normal to the slit contributes to the longitudinal oscillation of electrons. Consequently, the magnitude of excited SP becomes the maximum when the polarization of incident light has the electric field perpendicular to the slit.

Three cases of SP excitation at a slit with the backside illumination are illustrated in Figure 3.2. Figure 3.2(a) shows the case that the polarization of illuminating light is perpendicular to the slit. In this case, the direction of polarization is the same as that of direction of SPs propagation. Therefore, the electric field thoroughly contributes to SP excitation. Second case is shown in Figure 3.2(b), in which the direction of the polarization does not coincide with direction of SPs propagation, having a nonzero angle. When the polarization has such nonzero angle, energy of electric field cannot thoroughly contribute to SP excitation. Rather the projection of electric field direction upon SP propagation direction can excite SPs. The third case is that the slit is illuminated by HVB, as shown in Figure 3.2(c). In contrast to the previous two cases, the HVB exhibits time-varying and spatially-dependent polarization direction. As a result, the angle between directions of the polarization and SP propagation varies along the slit.

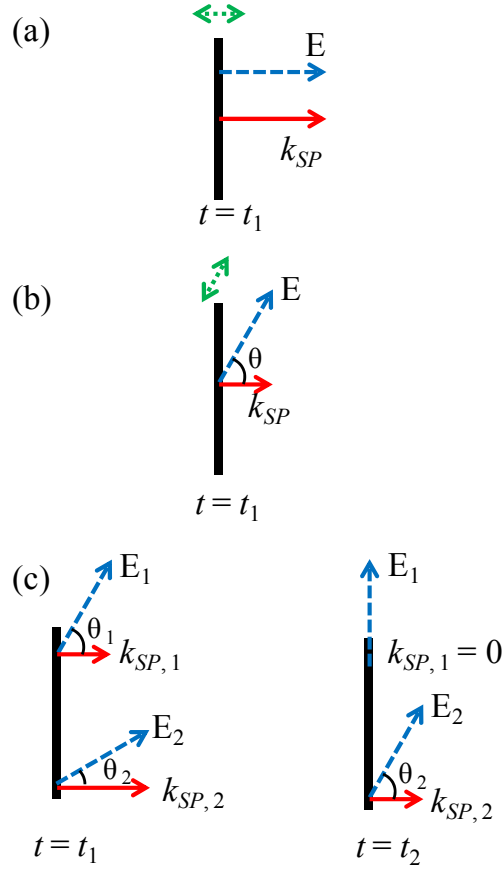


Figure 3.2 Three cases of SP excitation at a slit with the backside illumination. (a) The polarization of illuminating light is perpendicular to the slit. (b) The direction of the polarization has a nonzero angle to the direction of SPs propagation. (c) The slit is illuminated by the HVB.

3.2. Plasmonic vortex with helical vector beam

In previous section I treated the PVL and circular polarized beam. In this section, not only circular polarized beam, the HVB is considered for illuminated light.

3.2.1. Phase variation by PVL and HVB

When the PVL slit pattern is illuminated by the HVB from the back side, the SPs excited at the metal slit propagate toward the center of the PVL and generate the SP vortex. The properties of the SP vortex are governed by the total topological charge. In order to understand how the total topological charge is determined, it is necessary to examine the phase relationship in the PVL. Figure 3.3 presents the phase diagram of SPs excited at the PVL slits for various cases. The phase of SPs is highly dependent on the relationship between the direction of the instantaneous electric field and the direction of infinitesimal metal slit for the PVL. Throughout this dissertation, I define the relative phase Ω of the excited SPs as zero or an integer multiple of 2π when the amplitude A_{SP} of the in-plane electric field $E_{||}$ of incident light toward the center of the PVL reaches its maximum ($\Omega = \angle A_{SP}$). Here $A_{SP} = [\mathbf{E}_{||} \bullet (-\hat{\mathbf{r}})] / |\mathbf{E}_{||}|$ and $\mathbf{r} = \hat{\mathbf{x}} \cos \phi + \hat{\mathbf{y}} \sin \phi$. Figure 3.3(a) shows the phase diagram for the radial polarization with $l = 0$. For the initial state with $\omega t = 0$, the in-plane electric field heads toward the center of the PVL. The resultant phase is $\Omega = 0$, which is denoted by the red arrows. As time evolves, the phase decreases and the phase becomes $\Omega = 3\pi/2$, (or $\Omega = -\pi/2$), which is represented by the yellow arrows. The next level ($\omega t = \pi$) exhibits the in-plane electric field directed outward of the PVL and the resultant phase is $\Omega = \pi$ (the blue arrows). The final phase with $\omega t = 3\pi/2$ gives rise to $\Omega = \pi/2$. Note that all the phases Ω are the same along the circle in this case. In Figure 3.3(b)-(d), I show more complicated cases. If there is a phase retardation coming from the helical winding ($l = 1$, Figure 3.3(b)), then the SPs excited at the slit also carry the phase retardation proportional to $\exp(i\phi)$. If the PVL is illuminated by the RCP without the helical phase retardation (Figure 3.3(c)), the initial phase of SPs excited at the slit depends on the azimuthal phase. This is because the angle between the directions of the slit and the in-plane electric field differs along the azimuthal phase of the slit position. Figure 3.3(d) illustrates the PVL with $m = 1$ illuminated by the full-symmetric HVB with the radial polarization and no helical phase. Note that the initial phases at the slit are the same. In this case, however, the distance from the center of the PVL to the slit is linearly proportional to the azimuthal angle of the slit. Therefore, another type of phase retardation occurs: the propagation phase retardation. This relation is represented by the

arrows between the PVL slit and the hypothetical circle (denoted by dashed line). Note that the number of arrows is dependent on the azimuthal angle. The resultant phase distribution along the dashed circle exhibits the same phase distribution as those of the case in Figure 3.3(b) and (c). From discussion above based on the phase diagram, it can be inferred that the phase distribution of the SPs inside the PVL is affected by three factors: the helical phase of the HVB, the polarization state, and the geometrical charge of the PVL.

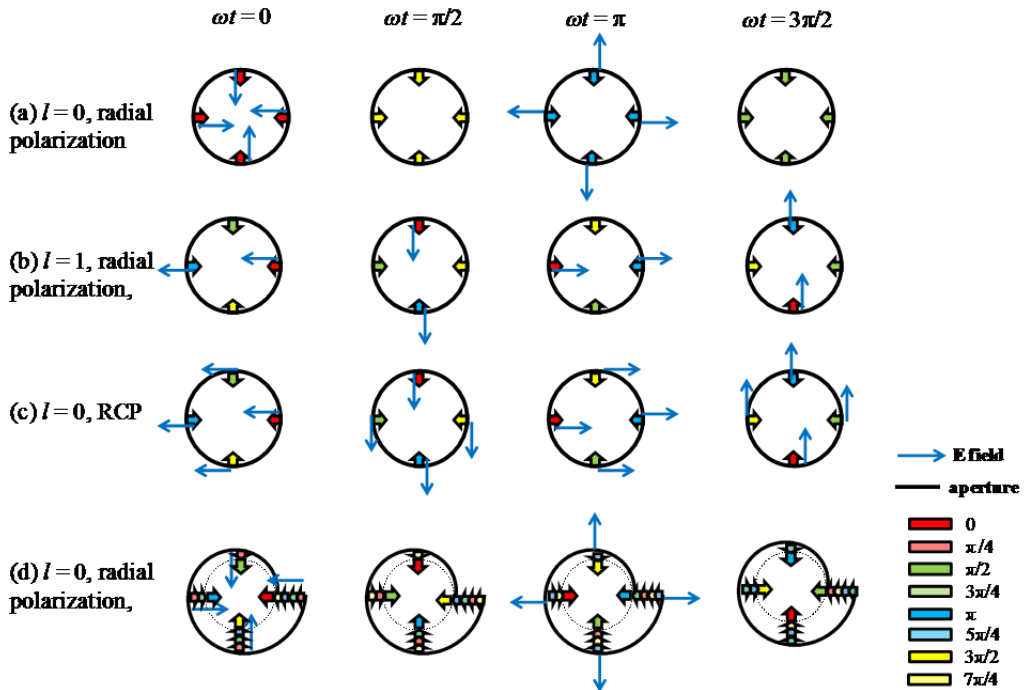


Figure 3.3 Phase diagram of SPs generated at the PVL for four cases: (a) $(l, m, s) = (0, 0, 0)$, (b) $(l, m, s) = (1, 0, 0)$, (c) $(l, m, s) = (0, 0, 1)$, and (d) $(l, m, s) = (0, 1, 0)$. The most left panel corresponds to the phase of $\omega t = 0$. As time evolves, each phase decreases since wave functions have the time-dependence of $\exp(-i\omega t)$. The most right panel exhibits the phase of $\omega t = 3\pi/2$.

The aforementioned property can be expressed in a simple algebraic equation. When the HVB with azimuthal phase term $\exp(il\phi)$ illuminates the PVL, the phase on the slit

varies according to the position on the PVL. The value of topological charge can be either increased or decreased by proper helical phase. Here phase term of $\exp(il\phi)$ shares the same positive direction as that of geometrical charge of the PVL. The topological charge j by the PVL and the HVB is given by $j = l + m$. In addition, this can be extended to take the effect of polarization status into account, i.e., the total topological charge j is given by

$$j = l + m + s. \quad (3.1)$$

One may be inclined to ask the values of spin parameter s for the radial and azimuthal polarizations. In the PVL structure, the radially polarized HVB excites SPs as seen for the linear polarization perpendicular to slit at each point. s of the radial polarization is 0 as can be observed with simulation results in Section 3.2.3.

3.2.2. Plasmonic ortex lens with circular polarized beam

Let us first understand the mathematical structure of the SP vortex that shows all concepts addressed in this dissertation very clearly. The z -directional electric field of the SP vortex on a flat metal/dielectric interface (x - y plane) is mathematically represented by the j -th order Bessel function with the spiral phase profile of $j\phi$:

$$E_{z,j}(r, \phi) \propto J_j(k_{SP}r) \exp\left[ij\left(\phi - \frac{\pi}{2}\right)\right], \quad (3.2)$$

where k_{SP} is the wavenumber of the SP wave given by $k_{SP} = 2\pi/\lambda_{SP}$ and λ_{SP} is the wavelength of the SP. (r, ϕ) is the polar coordinate corresponding to the Cartesian coordinate (x, y) . Here, the index j , which is the proportional constant of the azimuthal angle ϕ in the phase around the dark spot, is referred to as the topological charge of the SP vortex. The whole vectorial field representation of the SP vortex is presented in Section 3.2.5 ‘Orbital angular momentum of the surface plasmon vortex fields’. The angular spectrum representation of Eq. (3.2) unveils the physical origin of the SP vortex;

$$J_j(k_{SP}r) \exp\left[ij\left(\phi - \frac{\pi}{2}\right)\right] = \frac{1}{2\pi} \int_0^{2\pi} \exp(im\phi) \exp\left[ik_{SP}(x\cos\phi + y\sin\phi)\right] d\phi \quad (3.3)$$

where $j = m$. Throughout this dissertation, ϕ denotes the azimuthal angle associated with the SP angular spectrum and the geometry of PVL, whereas φ indicates that of the resultant SP vortex field. The superposition of the infinitesimal SP plane waves converging to the center with the spiral phase $\exp(im\phi)$ results in the SP vortex taking the form of the j -th order Bessel function with the spiral phase profile of $\exp[ij(\phi - \pi/2)]$ with the phase difference $j\pi/2$ from the spiral phase profile of the angular spectra ($j = m$).

The objective of PVL is to make such a converging angular spectrum with the spiral phase profile $\exp(im\phi)$ to synthesize SP vortex around the converging center. The design equation of PVL is directly derived from Eq. (3.3). The spiral phase profile of the angular spectrum plane wave can be provided by the PVL having the specific curved slit pattern on thin metal film given by

$$r_m(\phi) = r_i + \frac{\lambda_{SP}m\phi}{2\pi}, \quad \text{for } 0 \leq \phi < 2\pi. \quad (3.4)$$

Here, the inner radius r_i is the distance from the center to the nearest point of the slit. According to this equation, the distance from slit to the center is proportional to the value of azimuthal angle ϕ . Since the energy of SPs decays as SPs propagate, SP propagating from slits at large azimuthal angle experiences large energy decay and the uniformity of SP energy at the center deteriorates. In order to avoid this unnecessary degrade, Eq. (3.4) can be modified to

$$r_m(\phi) = r_i + \frac{\lambda_{SP} \text{mod}(m\phi, 2\pi)}{2\pi}, \quad \text{for } 0 \leq \phi < 2\pi. \quad (3.5)$$

The notation $\text{mod}(a, b)$ represents the remainder of the division of a by b . The outer radius r_o , defined as the distance from the center to the farthest slit point, is given by $r_i + \lambda_{SP}$. Figure 3.5(a) shows the relative phase differences between the converging angular spectra of the SP waves generated from each infinitesimal curved slit of the PVL under

radial polarization. If the radial polarization beam illuminates the PVL from the bottom, it induces SP point sources with the same phase on the curved slit pattern of $r_m(\phi)$, as shown in the light red arrows in Figure 3.5(a). However, as the SP waves travel from the slit to the center, they experience the phase retardations, which are proportional to the distance from the slit to the center region, as indicated in the arrows with light colors in Figure 3.5(a). Owing to the spiral geometry of the slit pattern, the SP waves excited on the PVL comprise the angular spectrum with the spiral phase along the circumference of the dashed circle in Figure 3.5(a). Note that there are $\pi/2$ phase delays between the point A, B, C, and D on the circle. Consequently, the spiral phase profile of the resultant SP vortex field has $\exp(i2\phi)$ i.e., the topological charge of the SP vortex is $j = 2$. It is noteworthy that this spiral phase originates from the geometric structure of the slit pattern. In this sense, I can say that the PVL shown in Figure 3.5(a) has the geometric vortex topological charge of $m = 2$ for this example PVL. Throughout this dissertation, I adopt a convention that the plus and minus signs of the geometric vortex topological charge correspond to the right- and left-handed rotation direction of the PVL slit patterns looking from the top, respectively. In other words, if the geometric vortex topological charge m is positive, the distance from the center to the slit increases as the azimuthal angle ϕ increases and vice versa. Note that the plasmonic lens for making a single SP hot spot can be regarded as the simplest PVL with $m = 0$ [12].

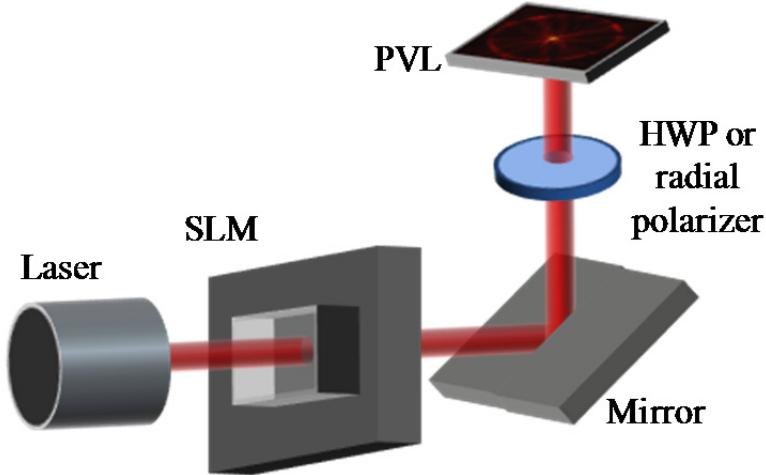


Figure 3.4 Hypothetical experimental setup. The PVL is inscribed on the gold layer. The wavelength of laser is 660 nm and the corresponding wavelength of SPs is 641 nm.

The aforementioned hypothesis is verified by using full-vectorial and three-dimensional rigorous coupled-wave analysis (RCWA) [31]. RCWA is a kind of mode analysis method, it needs to simulate sufficient number of modes for analysis to saturation. In this simulation, the number of analyzed modes is decided by steady state of field patterns and it is 31 by 31 on x - y directions. In the simulation it is assumed that the experimental setup is as shown in Figure 3.4. The PVL is inscribed on the gold layer. The wavelength of laser is 660 nm and the corresponding wavelength of SPs is 629 nm. The laser beam is assumed to be modulated by the phase SLM. When the modulated laser beam passing through a quarter wave plate or a radial polarizer illuminates the PVL from the backside, SPs are excited at the slit and propagate toward the center of the geometry. The simulation is carried out with altering three variables: the variable for geometrical effect of the PVL m , the polarization effect s , and the helix winding number of azimuthal phase term l . The key factor governing the properties of the plasmonic vortex is the topological charge. I can extract the topological charge by measuring the primary ring size of the generated plasmonic vortex [26].

The proposed PVL has interesting polarization sensitivity for the illumination of circular polarization beams. In contrast to the case of the radial polarization, the phases of the SP waves generated at the slit pattern depend on the azimuthal angle ϕ . In Figure 3.5(b), I illustrate the SP angular spectrum under the illumination of the right-handed circular polarization. Since the direction of the SP wave generated at an infinitesimal part of a slit is always normal to the part of the slit [4, 14, 15, 41], the initial phases of the SP waves arriving at the points B, C, and D in Figure 3.5(b) are led by $\pi/2$, π , and $3\pi/2$ compared with that at the point A, respectively. In other words, the right-handed circular polarization beam induces the SP point sources with $\exp(i\phi)$. This is the key difference from the case of the radial polarization where the SP point sources have the same phase. The arrows with dark red and dark yellow colors in the points A and B show the phase difference of $3\pi/2$ at the circumference. In a similar way, one can also construct the phase relation between the points C and D. The resulting spiral phase profile of the SP angular spectrum exhibits $\exp(i3\phi)$, and then the topological charge of the synthesized SP vortex is $j=3$. Figure 3.5(c) illustrates the SP angular spectrum for the left-handed circular polarization beam. The initial phases of the SP waves at the points B, C, and D are led by $\pi/2$, π , and $3\pi/2$ compared to that at the point A, respectively. It can hence be inferred that illumination of the left-handed circular polarization beam on the PVL induces the SP point sources with $\exp(i\phi)$. It is seen in Figure 3.5(c) that the spiral phase profile of the SP angular spectrum is obtained as $\exp(i\phi)$, i.e., $j=1$.

This phase structure induced by the circular polarization beams leads to interesting effect on the synthesis of SP vortex by the PVL. The synthesis of SP vortices by the right- and left-handed circular polarization beams can be mathematically represented as

$$J_j(k_{SP}r)\exp\left[ij\left(\phi - \frac{\pi}{2}\right)\right] = \frac{1}{2\pi} \int_0^{2\pi} \exp[i(m \pm 1)\phi] \exp[jk_{SP}(x\cos\phi + y\sin\phi)] d\phi, \quad (3.6)$$

where $j = m + s$. Especially, the circularly polarized beam is considered to have the SAM of $\sigma = s\hbar$, where $s = +1$ for the right-handed circular polarization (RCP) and $s = -1$ for the left-handed circular polarization (LCP), respectively [16]. Therefore, the dynamic

switching of SP vortices with topological charges of $j=m+1$ and $j=m-1$ can be performed on the PVL of geometric vortex topological charge m by the dynamic change of polarization state of circular polarization excitation beam.

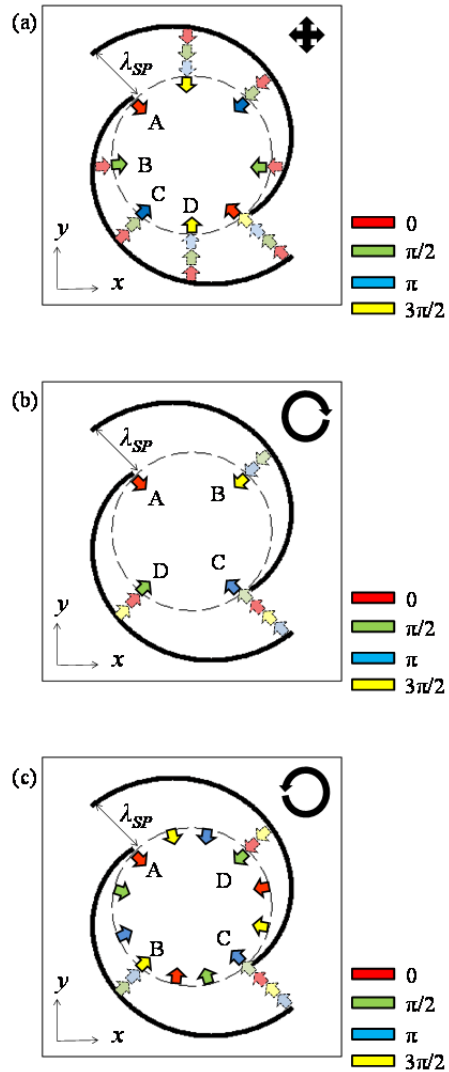


Figure 3.5 Schematic diagram of the converging angular spectrum of the SP waves inside the plasmonic vortex lens with $m=2$ under (a) the radial polarization, (b) the right-handed circular polarization, and (c) the left-handed circular polarization. The black arrows in upper right corners show the polarization states. The red, green, blue, and yellow arrows correspond to the out-of-plane electric field E_z with the relative phase difference of 0, $\pi/2$, π , and $3\pi/2$, respectively. The dark colors are used to give emphasis on the phases along the circumference of a circle.

3.2.3. Simulation result with helical vector beam

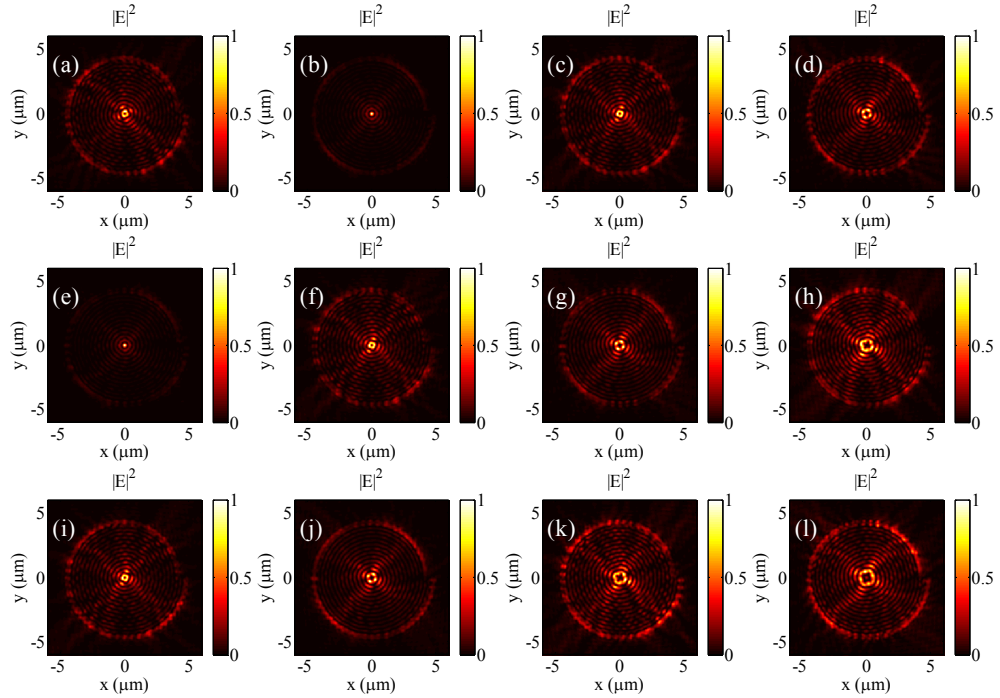


Figure 3.6 Simulation result with various HVBs for a fixed geometrical charge ($m = 1$). For the sake of clear comparison, the arrangement of panels is the same as that in Figure 3.1.

Figure 3.6 shows the simulation result with various HVBs with the fixed geometrical charge ($m = 2$). In this figure, the top panel corresponds to the LCP ($s = -1$), the middle to the radial polarization ($s = 0$), and the bottom to the RCP ($s = +1$). From the left panel, helix winding number l varies from -1 to 2 with increment of one. For the sake of clear comparison, the arrangement of panels in Figure 3.6 is the same as that in Figure 3.1. As shown in Figure 3.6, for the PVLs with the topological charge of 2, such as $(l, m, s) = (1, 1, 0)$, $(0, 1, 1)$, and $(2, 1, -1)$, the primary ring sizes of the plasmonic vortices are the same. Other PVL group with the same topological charge exhibited the same vortex radius as expected.

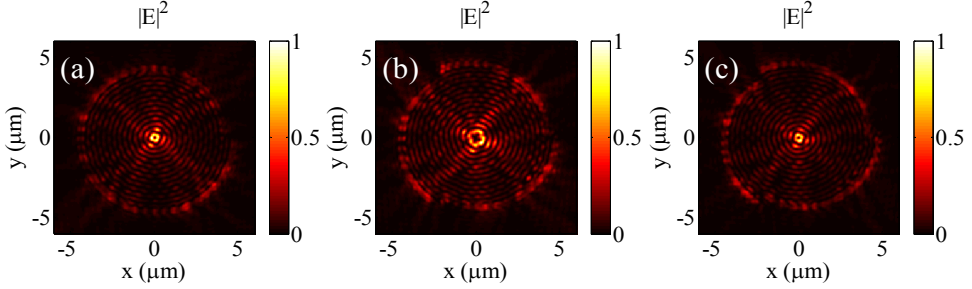


Figure 3.7 Geometric effect of PVL. (a) $(l, m, s) = (0, 1, 0)$, (b) $(l, m, s) = (0, 3, 0)$, (c) $(l, m, s) = (-1, 3, -1)$.

Figure 3.7 shows the geometric effect of PVL. While the polarization parameter s and the helix winding number l are fixed, the geometric effect m of the PVL is varied. It turns out that the change of the primary ring sizes of the plasmonic vortex also depends on the variation in geometric charge of PVL as shown in Figure 3.7(a) with $(l, m, s) = (0, 1, 0)$ and Figure 3.7(b) with $(l, m, s) = (0, 3, 0)$. In this case the total vortex charges are different from each other, resulting in the different sizes of the plasmonic vortices. However, even if the sum of the polarization effect and the helix winding number is different, vortex radii can be the same when PVLs are appropriately used as shown in Figure 3.7(c) with $(l, m, s) = (-1, 3, -1)$. It can be noted that the primary ring sizes of the plasmonic vortices in Figure 3.7(a) and (c) are the same. This is because the total vortex charges of those configurations are the same ($j = 1$).

The quantitative analysis of the result is as below. Point sources Q_{SRC} are aligned along the circle with the radius b and the angle ϕ . They are assumed to have the phase distribution function $g(\phi)$ which implies overall effects of the geometric, polarization, and azimuthal phases. The SPs propagate from a point source with the SP propagation constant k_{SP} . When an observation point is represented by $P(r, \varphi)$ inside the PVL, the wave function $f(r, \varphi)$ at $P(r, \varphi)$ is given by

$$f(r, \varphi) = \int_0^{2\pi} g(\phi) \exp[i k_{SP} |P(r, \varphi) - Q_{SRC}(b, \phi)|] d\phi. \quad (3.7)$$

By using Taylor's expansion and the integral form of the Bessel function of the first kind, I obtain approximation equation,

$$f(r, \varphi) \approx 2\pi J_j(k_{SP}r) \exp(ik_{SP}b) \exp[ij(\varphi - \pi/2)], \quad (3.8)$$

where $j = l + m + s$. The quantitative plasmonic vortex pattern is given with intensity of electrical field, $|f(r, \varphi)|$. Therefore, the primary ring size is given with solution of the Bessel function of the first kind.

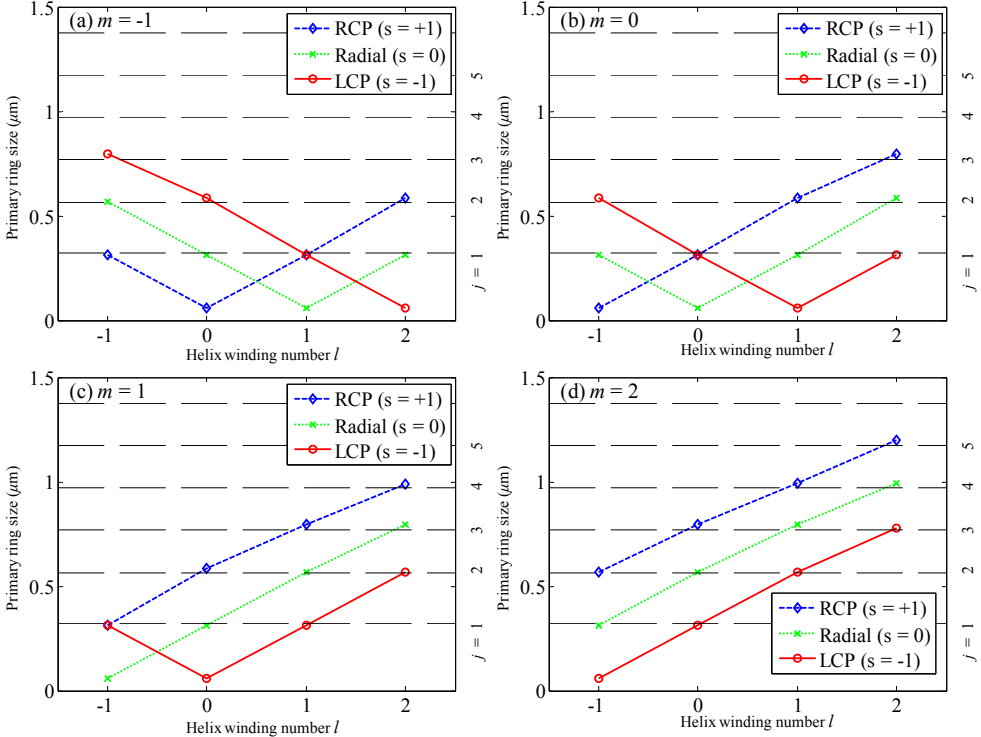


Figure 3.8 Radius of vortex as a function of azimuthal phase term l . Each figure displays different geometric effect, (a) $m = -1$, (b) $m = 0$, (c) $m = 1$, (d) $m = 2$. The blue dashed, green dotted, and red solid lines with diamond, cross, and circle markers denote results of the RCP, the radial polarization, and the LCP, respectively. The black dashed lines denote solution of the Bessel function of the first kind.

Figure 3.8 shows the radius of vortex as a function of the azimuthal phase term l . Each figure displays different geometric effect, such as $m = -1$ in Figure 3.8(a) and $m = 0$ in Figure 3.8(b). The blue dashed, green dotted, and red solid lines with diamond, cross,

and circle markers denote results of the RCP, the radial polarization, and the LCP, respectively. The left vertical axis of ordinates displays radius of vortex and the right vertical axis, solution of Bessel function of the first kind. As expected, the result shows the radii of vortices are identical when the PVLs have same topological charge j , which is the sum of geometrical charge m , polarization effect s , and azimuthal phase term l . Moreover, this figure shows that the primary ring sizes of simulation result are almost identical to solution of the Bessel function of the first kind.

3.2.4. Fractional plasmonic vortex

So far I have only considered the case in which all parameters j , l , m , and s are the integers. A question for the non-integer (or fractional) cases naturally arises. This section covers the case when those parameters have non-integer values and what would happen in that case. I also examine if the superposition rule ($j = l + m + s$) is still valid in the non-integer cases.

Non-integer l and m arises when the wavelength of the laser beam does not match that for the designed optical system. A spiral phase plate or an SLM induces a certain amount of phase delay and the amount of the modulated phase is intrinsically dependent on the wavelength of light. The parameters l and m are associated with the winding number of phase around the center axis, and thus they are integers when the modulated phase is an integer multiple of 2π . If the wavelength of incident light is different from the wavelength designed for the optical device, then the resultant amount of the modulated phase is not 2π anymore; it could go beyond or under 2π . For example, if the laser beam with the 600 nm wavelength illuminates the spiral phase plate or an SLM that induces 2π phase delay ($l = 1$) for the 660 nm, then the phase modulation would exceed 2π and the resultant helix winding number would be greater than one ($l \approx 1.1$). Likewise, the phase delay by the PVL is also dependent on the operating wavelength. If the PVL designed as $r = a + \lambda_{660} \phi / (2\pi)$ with the SP wavelength (λ_{660}) for free space wavelength of 660 nm ($m = 1$) is illuminated by a laser beam with a different wavelength of 600 nm, then the SP wave *feels* the distance λ_{660} more than 2π , which leads to a non-integer m ($1 < m < 2$).

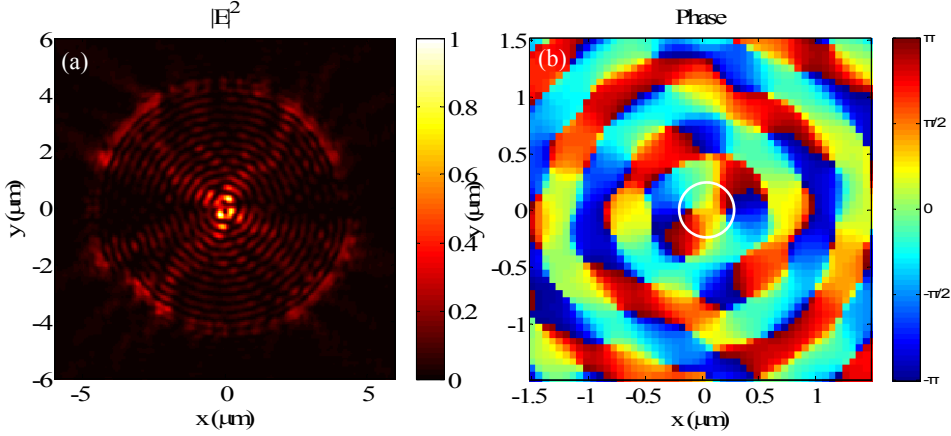


Figure 3.9 Phase discontinuity breaks the plasmonic vortex pattern as shown in (a) with $(l, m, s) = (0, 1.7, 0)$. The phase of surface plasmon at the center of PVL is represented in (b) with $(l, m, s) = (0, 1.7, 0)$.

In order to examine the effect of fractional l or m in the plasmonic vortex, I carried out numerical simulations. Let us first consider cases where either l or m is non-integer. If the helix winding number l is not an integer, the phase discontinuities are generated by the HVB along the axis and they cause a singular line linking the discontinuities in free space [42,43]. As noted earlier, the plasmonic vortex pattern is superposition of SPs propagating in the PVL, and the phase of the SP wave is affected by the illuminating light phase. Consequently, those discontinuities also affect the vortex pattern and generate a singular line in the plasmonic vortex pattern. In the same manner as the fractional l , the PVL with fractional m generates a singular line. Recall that the PVL is designed by using equation $r = a + \lambda_{SP} \text{mod}(m\phi, 2\pi) / (2\pi)$. Because of different optical path lengths between $\phi = 0$ and $\phi = 2\pi$, the PVL with fractional m thus makes discontinuity along x -axis. This discontinuity makes a singular line and breaks the plasmonic vortex pattern as shown in Figure 3.9(a) with $(l, m, s) = (0, 1.7, 0)$. In order to explain the effect of fractional l and m , phase profiles inside of vortex pattern are calculated by using RCWA. The phase profile is obtained along the circle whose center is coincident with center of vortex pattern as shown in Figure 3.9(b), which represents the phase of surface plasmon at the center of PVL.

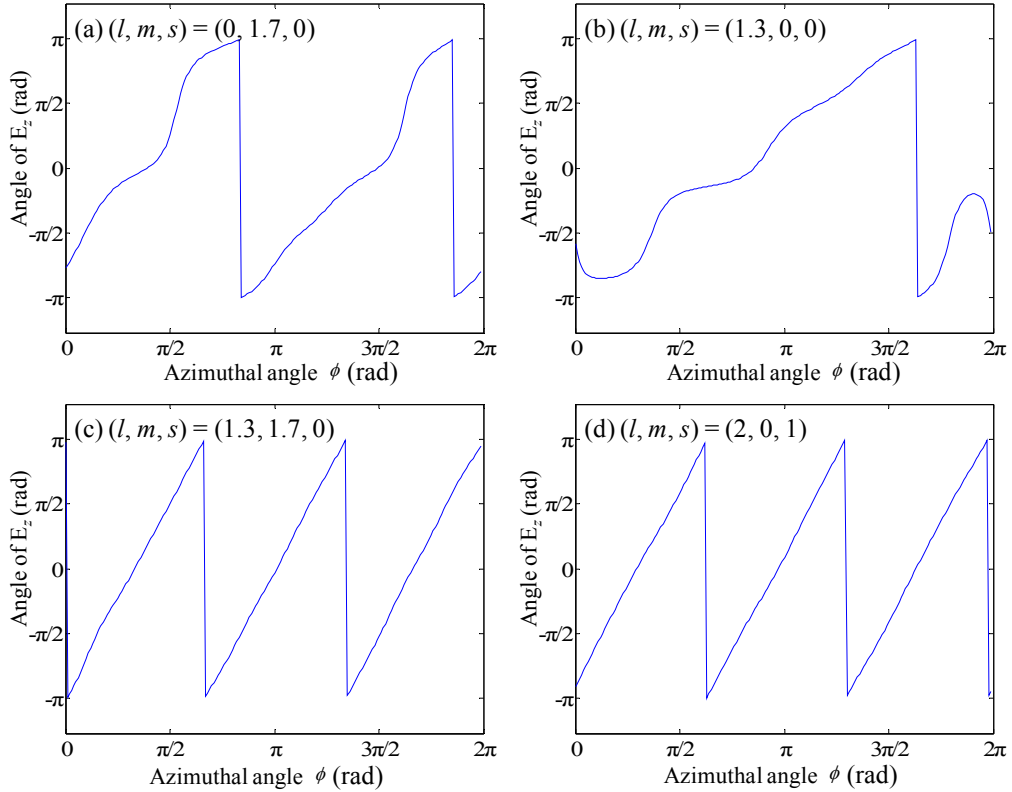


Figure 3.10 The phase profile is obtained along the white circle in Figure 3.9 and shown in (a) $(l, m, s) = (0, 1.7, 0)$, (b) $(l, m, s) = (1.3, 0, 0)$, (c) $(l, m, s) = (1.3, 1.7, 0)$, and (d) $(l, m, s) = (2, 0, 1)$. When j is fractional, the phase varies nonlinearly as shown (a) and (b). When j is integer, the phase varies linearly as shown in (c) and (d). This figure shows superposition property, $j = l + m + s$.

Figure 3.10(a) and (b) show the phase profiles in vortex pattern with $(l, m, s) = (0, 1.7, 0)$ and $(l, m, s) = (1.3, 0, 0)$, respectively. They show that the phase varies nonlinearly when m and l have fractional values. In the previous section, it was shown that the vortex topology j is determined by sum of l , m , and s when each value is integer ($j = l + m + s$) and this property originates from the superposition of the phase profile. It is not trivial whether the aforementioned superposition rule is still valid in the non-integer case. To examine this issue, I carried out simulations in which l and m are both

non-integers whereas their sum $l + m$ is an integer. Figure 3.10(c) shows the phase profile in vortex pattern with $(l, m, s) = (1.3, 1.7, 0)$. Note that this can be regarded as a superposition of $(l, m, s) = (0, 1.7, 0)$ (Figure 3.10(a)) and $(l, m, s) = (1.3, 0, 0)$ (Figure 3.10(b)). The topological charge j of Figure 3.10(c) is obtained as 3. It is noteworthy that its phase profile is the same as that of $(l, m, s) = (2, 0, 1)$ (Figure 3.10(d)), whose topological charge j is 3.

So far I have covered the fractional parameters only for l and m . One may be inclined to ask about the effect of the fractional spin parameter s . By using the spin operator, the spin of the polarization is represented as $s = \sin(2\theta)\sin(\varphi_{y-x})$, where the angle θ describes the angle between the amplitudes of the electric field components in the x and y directions, and φ_{y-x} is the relative phase difference of the electric field components in the x and y directions. In the case of the RCP, which is represented by $|R\rangle$, θ is $\pi/4$, φ_{y-x} is $\pi/2$, and $s = 1$. For the x -directional linear polarization ($|x\rangle$), θ is 0 and $s = 0$. In this equation, s is a real number between -1 and 1 when light has an elliptical polarization. Although the HVB has a fractional spin parameter s , light with a fractional s is unsuitable for PVL system. Because an elliptically polarized beam has different amplitudes between x and y directions, the intensity of excited SP waves is different with the position. Like the linearly polarized beam, the elliptically polarized HVB breaks uniformity of the SPs and it makes the asymmetric plasmonic vortex pattern. The radially polarized beam is represented by $|p_{Radial}\rangle = [\exp(-j\phi)|R\rangle + \exp(j\phi)|L\rangle]/2^{1/2}$, where $|L\rangle$ stands for the LCP and ϕ is the azimuthal angle [26,44]. This polarization is composed of the linear polarizations whose vector directions are toward the center of the beam. By using the spin operator, s of radial polarization is obtained as 0. Because the radially polarized beam excites the SP waves uniformly, it can be used in PVL system. Consequently, spin parameter s is one of only 1, 0 and -1 in the PVL system, and superposition property of PVL topology $j = l + m + s$ is satisfied at real number l, m and $s = 1, 0, -1$.

3.2.5. Orbital angular momentum of the surface plasmon vortex fields

A merit of the proposed PVL is that the OAM carried by the SP vortex fields can be tuned by the polarization state and phase of incident beam. In this section, I first present all components of the electromagnetic field in the SP vortex with the topological charge j . Then, the OAM of the SP vortex fields is derived. It will be shown that the OAM of the SP vortex fields is dependent on the topological charge j .

The z -component of the electric field in the SP vortex with the topological charge j is given by the angular spectrum representation as follows:

$$E_z(r, \varphi, z) = AJ_j(k_{SP}r)\exp[ij(\varphi - \pi/2)]\exp(-\kappa z), \quad (3.9)$$

where A is a constant and $\kappa^2 = k_{SP}^2 - k_0^2$. Here, k_0 is the wavenumber in free space. The definition of k_{SP} is presented in the main manuscript. The electric Hertz potential is obtained from Eq. (3.9) as follows [45]:

$$\pi_z(r, \varphi, z) = \left(\frac{A}{k_{SP}^2} \right) J_j(k_{SP}r)\exp[ij(\varphi - \pi/2)]\exp(-\kappa z). \quad (3.10)$$

Since the SP propagating along the interface between the metal and the dielectric is the transverse magnetic (TM) mode, the z -component of the magnetic field H_z is zero and the magnetic Hertz potential π_{mz} also vanishes. The in-plane electromagnetic fields are derived from the electric Hertz potential in Eq. (3.10) [45].

$$E_r(r, \varphi, z) = \left(-\frac{\kappa A}{k_{SP}} \right) J'_j(k_{SP}r)\exp[ij(\varphi - \pi/2)]\exp(-\kappa z), \quad (3.11)$$

$$E_\phi(r, \varphi, z) = \left(\frac{-ijkA}{rk_{SP}^2} \right) J_j(k_{SP}r)\exp[ij(\varphi - \pi/2)]\exp(-\kappa z), \quad (3.12)$$

$$H_r(r, \varphi, z) = \left(\frac{\omega \epsilon j A}{rk_{SP}^2} \right) J'_j(k_{SP}r)\exp[ij(\varphi - \pi/2)]\exp(-\kappa z), \quad (3.13)$$

$$H_\phi(r, \varphi, z) = \left(\frac{i\omega \epsilon A}{k_{SP}} \right) J'_j(k_{SP}r)\exp[ij(\varphi - \pi/2)]\exp(-\kappa z). \quad (3.14)$$

Here, ω and ϵ correspond to the angular frequency and the electric permittivity of the air, respectively. The angular momentum density is expressed as $\mathbf{j} = \mathbf{r} \times \mathbf{S}/c^2$, where \mathbf{S} is

the Poynting vector and c is the velocity of light in vacuum [46]. The z -component of the OAM is hence given by

$$\begin{aligned}\Gamma_z &= rS_\phi / c^2 \\ &= \frac{1}{2c^2} r \operatorname{Re} [E_z H_r^\dagger] \\ &= \left(\frac{\omega \epsilon j |A|^2}{2c^2 k_{SP}^2} \right) J_j^2(k_{SP}r) \exp(-2\kappa z).\end{aligned}\quad (3.15)$$

The symbol \dagger denotes the complex conjugate. Adopting $k_{SP} = \omega n_{SP}/c$, where n_{SP} is the effective refractive index of the SP propagating along the interface between the metal and the dielectric, I obtain

$$\Gamma_z = \left(\frac{\epsilon j |A|^2}{2\omega n_{SP}^2} \right) J_j^2(k_{SP}r) \exp(-2\kappa z) \propto \frac{P}{\omega} j,\quad (3.16)$$

where $P = |A|^2 J_j^2(k_{SP}r) \exp(-2\kappa z)$ is the power of the SP vortex field. This result is in agreement with that in Ref. [47].

Chapter 4

Surface plasmon modulation

4.1. SP modulation with PVL and circular polarized beam

4.1.1. Experimental setup and method

To prove the aforementioned properties of the synthesis and switching of SP vortices, I provide the experimental demonstrations with numerical simulations. The schematic diagram of the experimental setup is shown in Figure 4.1(a). The sample was illuminated from the bottom by the laser with the free space wavelength of 660 nm (Newport, LQA660-110C) and the SP evanescent field intensity distribution was measured by the near-field scanning optical microscope (NSOM) (Nanonics, Multiview 4000). For the sample fabrication, first, the Ag layer with the thickness of 300 nm was evaporated on a fused silica wafer (MUHAN, MHS-1800). Then the PVL slit patterns with the geometrical vortex topological charges m ranging from zero to four were inscribed on the Ag layer by using the focus ion beam (FIB) (FEI, Quanta 200 3D). Figure 4.1(b) shows the scanning electron microscopy (SEM) image of the PVL with the geometric vortex topological charge of $m = 4$. The inner radius r_i is $4 \mu\text{m}$. The slit width is set to be 250 nm, which was found to result in the maximum SP excitation efficiency

through numerical simulations. For the free space wavelength λ_0 of 660 nm, the relative permittivity of the silver, ε_m , is given by $-17.7+1.18i$ [48]. The relative electric permittivity values of the glass and air are 2.25 and 1, respectively. The effective refractive index of the SP at the interface between the Ag layer and air is $n_{SP} = 1.03$, resulting in the SP wavelength λ_{SP} of 641 nm. The propagation length of the SP is $L_p=25.7 \mu\text{m}$.

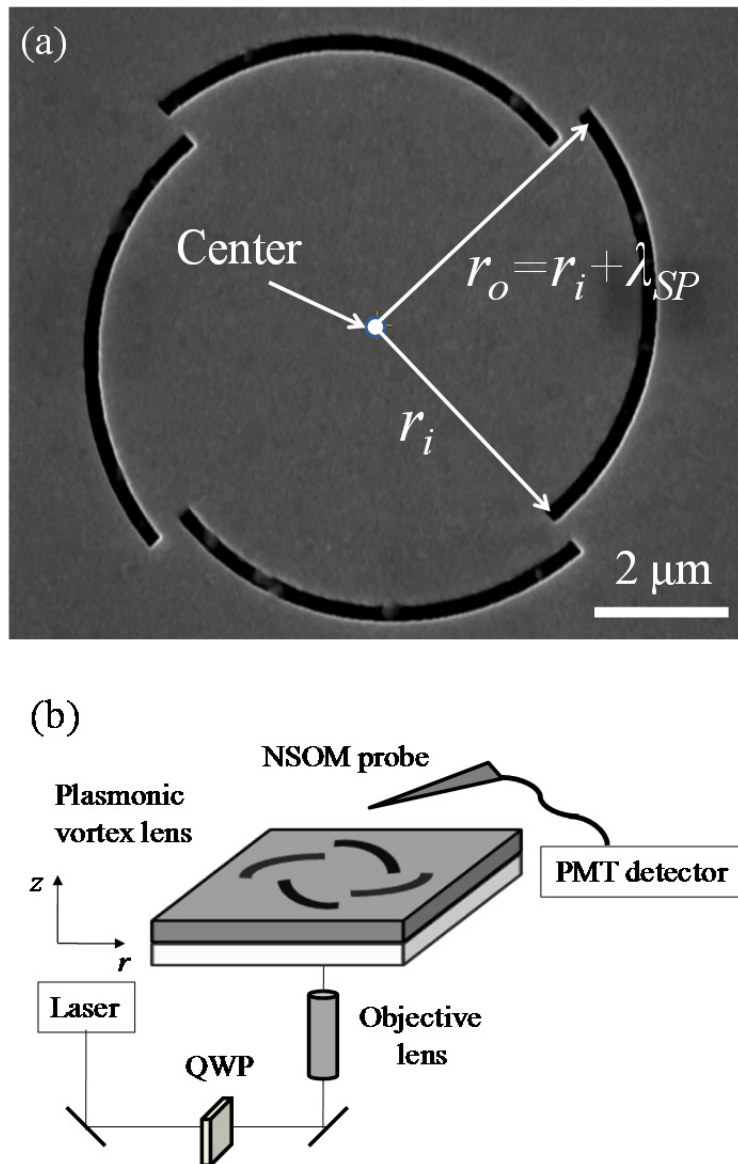


Figure 4.1 (a) SEM image of the PVL with the geometrical vortex topological charge $m=4$. The inner (r_i) and outer (r_o) radii are $4.00 \mu\text{m}$ and $4.64 \mu\text{m}$, respectively. (b) Experimental setup for the NSOM. Illuminated from the bottom is the laser with the free space wavelength of 660 nm and the circular polarization.

Located under the sample was the microscopic objective lens with the magnification of 10x, the numerical aperture of 0.28, the working distance of 33.5 mm, and the depth of focus of $3.5 \mu\text{m}$. To illuminate the whole area of PVL uniformly, the beam was slightly defocused on the sample [15]. The SP field inside the PVL was detected by the cantilever type metal-coated (Cr/Au) NSOM tip with the diameter of 250 nm. The feedback mode in the NSOM system I used is the non-contact intermittent mode (or tapping mode), in which the tip is tapping over the sample and touches it with the resonance frequency of the tip during the scan. The main benefit from this mode is that there is less chance to damage the sample or the tip compared with the contact mode while the tip is in close proximity (~ 50 -100 nm) to the sample enough to detect the SP field, the decay length of which is ~ 430 nm. The photomultiplier tube (PMT) (Hamamatsu, H7422-20) with the gain of 10^7 was used to convert the light intensity transmitted by the optical fiber into electric signal. The image processing was done with the WSXM [49]. The quarter wave plate was used to achieve the circular polarization beam. Unfortunately, the experimental result for the radial polarization is not presented, because in my experiment setup it was impossible to achieve sufficient accuracy in the alignment between the centers of the radial polarizer and the PVL.

4.1.2. Experimental result

The experimental results are presented with simulation results in Figure 4.2 and 4.3. For the simulation, I employed the rigorous coupled wave analysis (RCWA) with the 63 Fourier harmonics for the x - and y -directions, respectively. The size of the computation cell was chosen to be $14 \mu\text{m} \times 14 \mu\text{m}$. The absorbing boundary layer was used to simulate aperiodic structure, by which the influence from the adjacent periodic cells is prohibited [15, 31]. In Figure 4.2(a)-(d), presented are the experiment and simulation results for the case in which the rotation direction of the circular polarization beam is the same as that of the geometric vortex topological charge. Figure 4.2(a) and (b) show the field intensity of the SP vortex measured by the NSOM, and the field intensity $|E|^2$ obtained by the RCWA at the interface between the Ag layer and air, both of which

prove the formation of SP vortex clearly. The white arrow denotes the direction of the rotation of the circular polarization beam looking in the top view. In Figure 4.2(a), it is observed that the dark spot surrounded by the bright circumference, which is called the primary ring of a vortex, is generated at the center of the structure [34, 50]. Outside the primary ring, I can see the interference pattern with the period of $\lambda_{SP}/2$. In our experiment, the NSOM signal level at the brightest point on the primary ring is 2.4 V. In our NSOM equipment, the signal level of 1 V indicates that the optical fiber connected to the NSOM tip carries the power of about $1.25 \mu\text{W}$. The power measured through the NSOM tip-fiber at the primary ring is about $3 \mu\text{W}$. Considering that the power of the incident laser beam is 40 mW, the focusing efficiency of the PVL is estimated as 3.13×10^{-5} . Note that, however, since there is some coupling loss of the SP field into the tip, it is difficult to estimate the exact field intensity at the NSOM tip itself as well as the exact focusing efficiency of the PVL. Thus the intensity scales in Figure 4.2(a) and 4.3(a) are in the arbitrary unit. In Figure 4.2(c), the E_z field calculated by the RCWA, one can see five node lines around the center of vortex clearly, which indicates the rotation of the SP vortex. The topological charge of the SP vortex extracted from the E_z field intensity distribution is $j = 5$. In Figure 4.2(d), the intensity distribution of the SP vortex in the experiment is compared with the results of the analytic model and the RCWA simulation. The SP vortex profiles expected from the theory (Eq. (3.6)), the experimental result (along the dashed line in Figure 4.2(a)), and the RCWA simulation result (along the dotted line in Figure 4.2(b)) are plotted by the red dashed line, the blue solid line, and the black dotted line, respectively. The primary ring size of SP vortex is defined as the distance between two peaks surrounding the SP vortex shown in Figure 4.2(d). The experimental result coincides well with the simulation result as well as the analytic model. Note that the topological charge of the SP vortex is $j = 5$, whereas the geometric vortex topological charge of the PVL is $m = 4$. This shows that the RCP beam increases the topological charge of the SP vortex by one.

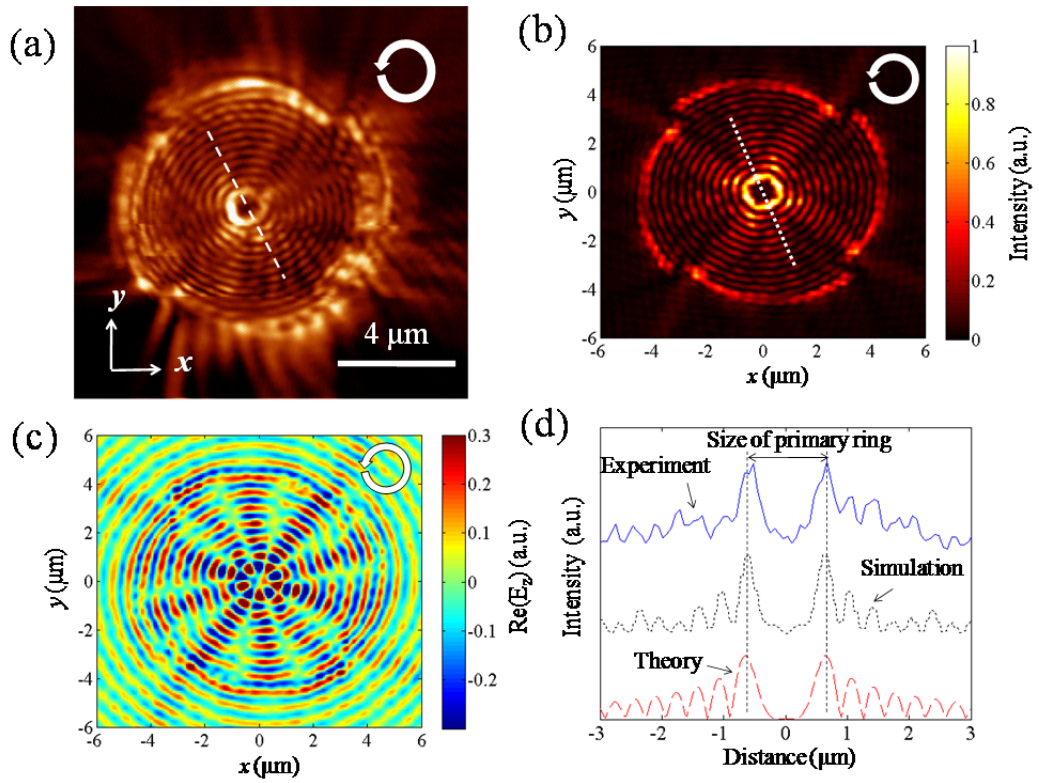


Figure 4.2 Experiment and simulation results under the right-handed circular polarization in (a)-(d). (a) Near-field intensity distribution measured by the NSOM. (b) Near-field intensity distribution calculated by the RCWA. The dark spot is clearly observed in both images. (c) E_z distribution of the near-field calculated by the RCWA. The number of node lines is five, which indicates that the topological charge of the SP vortex is $j=5$. The white arrows in (a)-(c) denote the directions of the rotation of the polarization. (d) Comparison of the intensity profiles. The red dashed line corresponds to the result of the theoretical model, i.e., the square of the absolute value of the 5th order Bessel function of the first kind. The blue solid line depicts the field intensity along the dashed line in the NSOM image of part (a). The black dotted line shows the field intensity along the dotted line in the RCWA image of part (b).

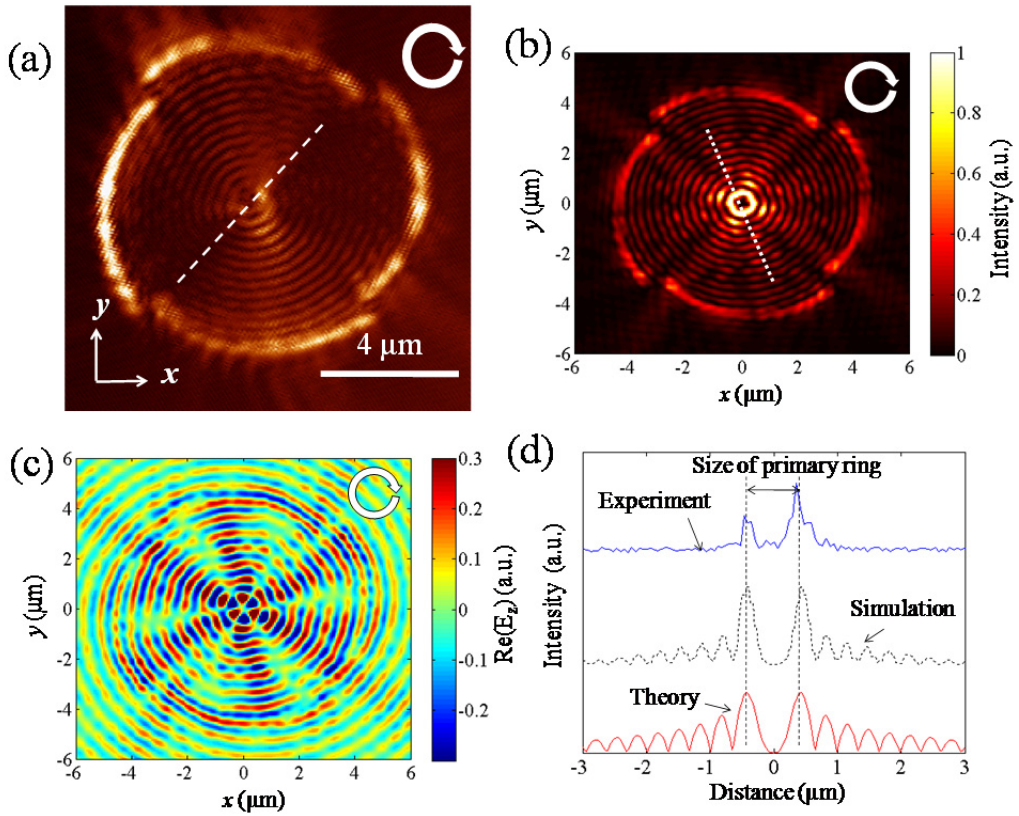


Figure 4.3 Experiment and simulation results under the left-handed circular polarization (a)-(d). (a) Near-field intensity distribution measured by the NSOM. (b) Near-field intensity distribution calculated by the RCWA. The dark spot is clearly observed in both images. (c) E_z distribution of the near-field calculated by the RCWA. The number of node lines is five, which indicates that the topological charge of the SP vortex is $j = 3$. The white arrows in (a)-(c) denote the directions of the rotation of the polarization. (d) Comparison of the intensity profiles. The red dashed line corresponds to the result of the theoretical model, i.e., the square of the absolute value of the 3rd order Bessel function of the first kind. The blue solid line depicts the field intensity along the dashed line in the NSOM image of part (a). The black dotted line shows the field intensity along the dotted line in the RCWA image of part (b).

Secondly, the experiment and simulation results on the use of left-handed circular polarization beam are shown in Figure 4.3(a)-(d). In this case, the excitation beam rotates in the counter direction to the PVL geometry. Figure 4.3(a) and (b) present the field intensity measured by the NSOM and calculated by the RCWA, respectively. It is firstly observed that the diameter of the primary ring of the SP vortex is smaller than that of the RCP beam (Figure 4.2(a) and (b)). The E_z field intensity distribution shows that there are three nodal lines, indicating that the topological charge of the SP vortex is $j = 3$. In Figure 4.3(d), the intensity distributions of the SP vortex in the experiment are compared with the results of the analytic model and the RCWA simulation. The SP vortex profiles expected from the theory (Eq. (3.6)), the experimental result (along the dashed line in Figure 4.3(a)), and the RCWA simulation result (along the dotted line in Figure 4.3(b)) are plotted by the red dashed line, the blue solid line, and the black dotted line, respectively. As shown in Figure 4.3(d), the field intensity distributions measured by the NSOM and calculated by the RCWA are in good agreement with the theoretical prediction with $j = 3$. It has been shown that the RCP and LCP beams upon the PVL with the geometric vortex topological charge of $m = 4$ give rise to the topological charges of the SP vortices with $j = 5$ and $j = 3$, respectively.

In order to be used for other application, high intensity of SP wave is needed. As shown in Figure 4.2 and 4.3, however, the intensity of SP wave is weak in comparison with far-field light from the slit. Bragg grating is one of the ways to increase the intensity of SP wave. By the recent research, intensity of SP wave is 2.5 times by using unidirectional coupler which uses Bragg grating [51]. If there are Bragg gratings on outside of plasmonic vortex lens, the intensity of SP wave will be increased by unidirectional coupling of SPs. The period of Bragg grating need to be half of SP wave length, in this case the period is 320 nm, which is half of 641 nm.

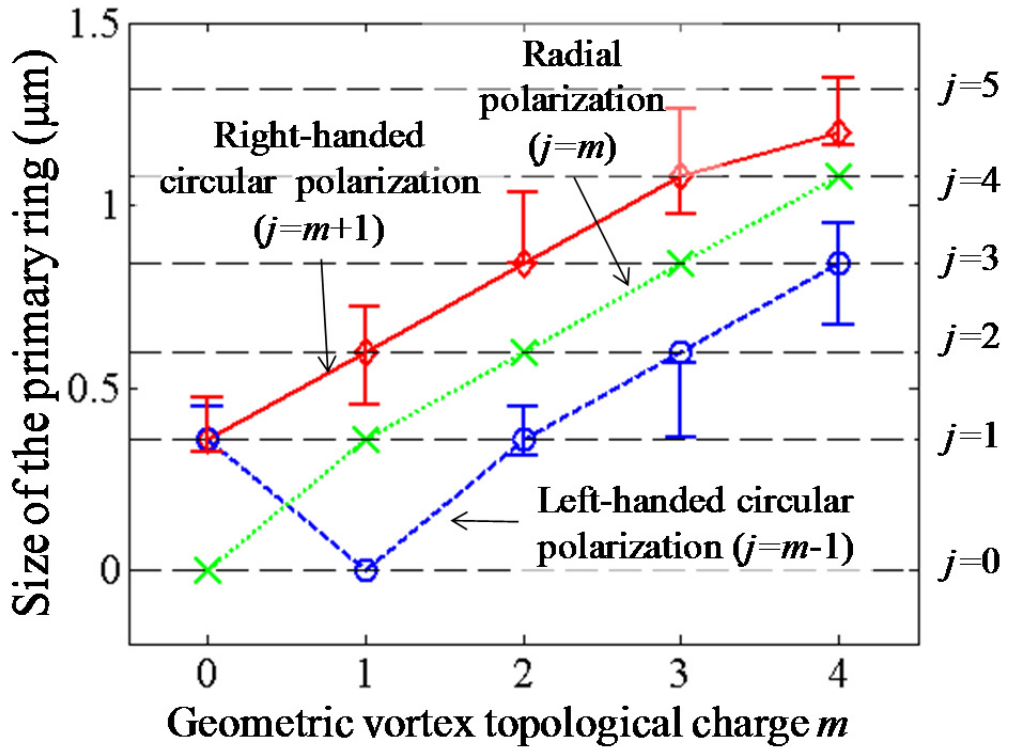


Figure 4.4 Size of the primary ring of the SP vortex as a function of the geometric vortex topological charge m for various types of the polarization states. The straight lines with markers are from the simulation results, whereas the error bars are from the experimental data. The horizontal dotted lines show the sizes of the primary rings from the theoretical prediction given by the Bessel function of the first kind. The topological charge of the SP vortex j is given by $j = m + 1$ for the right-handed circular polarization, $j = m$ for the radial polarization, and $j = m - 1$ for the left-handed circular polarization, respectively.

The aforementioned algebraic rule on the change of SP vortex proved for the PVL with the geometric vortex topological charge $m = 4$ can be extended to PVLs with arbitrary higher order topological charge. I examined the SP vortices generated by the

PVLs with various geometric vortex topological charges. Figure 4.4 plots the diameter of the primary ring of SP vortex as a function of the geometric vortex topological charge m for circular and radial polarizations. Considering that the primary ring size may vary slightly depending on the direction of the cross-line, I comparatively plotted the primary ring size obtained from the RCWA simulation (indicated by markers on straight lines) and that from the experimentally measured data with the error bars indicating maximum and minimum values of the primary ring size. The black horizontal dashed lines indicate the theoretical primary ring size of SP vortices with various topological charges obtained from Eq. (3.6). The rotation direction of the PVLs is kept right-handed ($m \geq 0$). The red solid line with diamond markers and the blue dashed line with circle markers correspond to the results for the RCP and LCP, respectively. The primary ring size of the SP vortex for the RCP increases monotonically with the geometrical vortex topological charge of the PVL and matches the theoretical result of $j = m + 1$. On the other hand, the size of the SP vortex for the LCP reaches its minimum for $m = 1$, and then increases monotonically. It is clearly seen that the SP vortices synthesized by the PVL of the geometric vortex topological charge m with the left-handed circular polarization beam have topological charge of $j = m - 1$. The result for the radial polarization is also noteworthy. The PVLs with the geometric vortex topological charge m under the radial polarization produces SP vortices with $j = m$, as indicated by the green dotted line with cross markers in Figure 4.4. This linear dependence of the primary ring size on the topological charge arises from the fact that the radial field distribution of the SP vortex presented here is ascribed to the characteristics of the Bessel function of the first kind. Whereas the optical vortices having the form of the Laguerre-Gaussian function exhibit the primary ring size proportional to $(j + 1)^{1/2}$ [34, 50], those related to the Bessel function of the first kind show the primary ring size proportional to j [52]. The linear property offers useful insight in design and analysis of the PVL.

4.1.3. Orbital angular momentum of SP vortex

It is noteworthy that the SP vortex carries the orbital angular momentum proportional to the topological charge j . In the Section 3.2.5, it is proved that the orbital angular momentum of the SP vortex, Γ_z , is proportional to the topological charge j as

$$\Gamma_z \propto \frac{P}{\omega} j, \quad (4.1)$$

where P and ω are the power of the SP vortex field and the angular frequency of SP. This is also in agreement with the result of Volke-Sepulveda *et al* [47]. It is therefore expected that the higher-order evanescent vortices generated by the PVLs could offer a way to gain more optical torque keeping the incident power [53–55].

Here, one may be curious about the maximum topological charge that can be achieved in a PVL. If the primary ring size exceeds the diameter of the PVL, then the SP vortex field inside the PVL vanishes. Thus it appears that the topological charge in practical applications should be limited so that the primary ring appears inside the PVL with a finite diameter. To obtain higher orbital angular momentum, I can increase both the diameter of a PVL and the geometric vortex topological charge m . However, as has been reported in Ref. [12], the propagation loss of the SP wave becomes dominant for a PVL with a large diameter. Therefore it seems that the extraction of an exact maximum topological charge in the general PVL geometry is not possible.

The relationship between the SP vortex and the PVLs under various polarization states can be understood by the terms of photon angular momentum. Light is described by its wavefront and polarization, which correspond to the OAM and the SAM, respectively [39, 56]. The orbit angular momentum per photon is obtained by taking the angular momentum operator $L_z = -i\hbar \frac{\partial}{\partial \varphi}$ to the wave function. For example, the application of the angular momentum operator to a wave function with phase profile of $\exp(im\phi)$ gives $m\hbar$. The spin angular momentum per photon is given by taking the spin operator S to the polarization state. The spin operator is defined as

$S = |R\rangle\langle R| - |L\rangle\langle L|$, where $|R\rangle$ and $|L\rangle$ denote the RCP and LCP states, respectively. For example, the RCP and LCP results in $S_R = \langle R|S|R\rangle = 1$ and $S_L = \langle L|S|L\rangle = -1$, respectively. By multiplying the Dirac's constant \hbar to the expectation value of the spin operator, I obtain the SAM per photon. Note that, due to the orthogonality between $|R\rangle$ and $|L\rangle$, the radial polarization $|p\rangle = [\exp(-i\phi)|R\rangle + \exp(i\phi)|L\rangle]/\sqrt{2}$ leads to $S_p = \langle p|S|p\rangle = 0$. The PVL plays a role of converting the SAM of excitation beam to the OAM of SP [16, 57]. The contributions of +1, 0, and -1 in Figure 4.4 are ascribed to the OAM converted from the SAM of $|R\rangle$, $|p\rangle$, and $|L\rangle$, respectively. The PVL with the geometric vortex topological charge m induces the OAM per photon, $m\hbar$, of SP vortex. Thus the total OAM per photon of the SP vortex is given by the sum of two aforementioned contributions, i.e., $j\hbar = (m+1)\hbar$, $m\hbar$, and $(m-1)\hbar$ for $|R\rangle$, $|p\rangle$, and $|L\rangle$, respectively. This algebraic rule can be used for the dynamic switching of SP vortex with the change of polarization state of excitation beam.

4.2. Beam modulation with annular aperture and HVB

Special types of optical beams, such as Bessel beams [58–61], Airy beams [62, 63], and plasmonic mediated micro-beams [64, 65] have been actively investigated for practical applications and as fundamental research. Among them, optical beams with phase singularity generated by a spiral phase plate, referred to as a vortex beam, have been a subject of active research recently [53, 58–61, 66]. Practical applications such as optical tweezers, optical trapping, and optical imaging adopt the unique advantages of using optical vortex beams [53, 66–69] as various functional control techniques of vortex beams are developed.

In general, an optical wave (assumed to be under normal incidence) that passes through a circular aperture with a spiral phase plate produces a slightly diverging vortex beam in the free space. The vortex beam has a phase singularity at the center of the beam.

As a result, a dark region appears at the center of the beam. From a three-dimensional viewpoint, as the phase singularity propagates toward free space, a three-dimensional dark shadow region is formed along the beam profile. This is referred to as a vortex-cone.

In diffractive optics, the manipulation technology pertaining to the intensity profile of an optical field is relatively well established, but the precise phase control of an optical field at a specific far-field plane remains a technological challenge. The spatial light modulator (SLM) is the most important type of diffractive optic device for wave-front modulation of the optical field [70–74]. Conventional amplitude-type SLMs and phase-type SLMs have both recently been developed; however, the development of an SLM capable of the simultaneous modulation of the amplitude and phase, i.e., a complex modulation SLM, is sought for the arbitrary control of complex optical fields, which is considered as a fundamental core technology for applications in holographic three-dimensional displays and optical communications.

In this dissertation, the generation of tiny multiple vortex-cones using a micro-scale annular aperture array and a phase-type SLM is studied. To form well-defined vortex-cones in free space, both the amplitude and phase of the optical field are modulated, during which a phase-type SLM is downscale-imaged onto the surface of the annular aperture array to modulate the phase of the optical field directly on that plane. As a result, an effective micro-scale annular-aperture phase-type SLM is obtained. It was experimentally demonstrated that dynamic and simultaneous control of the topological charge and positional translation of multiple vortex-cones is possible with the proposed direct-phase modulation technique.

Section 4.2 is organized as follows. In Section 4.2.1, the generation and control of a single vortex-cone is described and the experimental results are presented. In Section 4.2.2, the dynamic manipulation of multiple vortex-cones is demonstrated experimentally.

4.2.1. Generation and control of a single vortex-cone

In Figure 4.5 and 4.6, the three-dimensional field profiles of vortex-beam with a single vortex-cone are generated with a circular aperture (See Figure 4.5(a)) [50] and an annular

aperture (See Figure 4.5(b)) with the same diameter and spiral phase profile of the topological charge. Here, the cases of topological charge of three are compared. The simulation was performed based on scalar diffraction theory. In the simulation, the circular aperture, with a radius of $15 \mu\text{m}$, along with the annular aperture, with an outer radius of $15 \mu\text{m}$ and an inner radius of $14 \mu\text{m}$, are analyzed. Each point on the circular slit has a phase of $\exp(i3\varphi)$, where φ varies from 0 to 2π , $\varphi = \tan^{-1}(y/x)$.

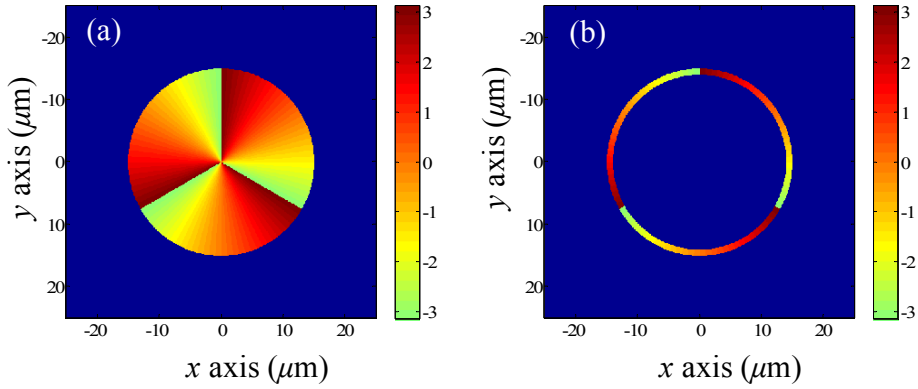


Figure 4.5. Phase profiles of (a) the circular aperture and (b) the annular aperture are shown, where the phase profiles are given by $\exp(i3\varphi)$, where φ as given by $\varphi = \tan^{-1}(y/x)$ varies from 0 to 2π .

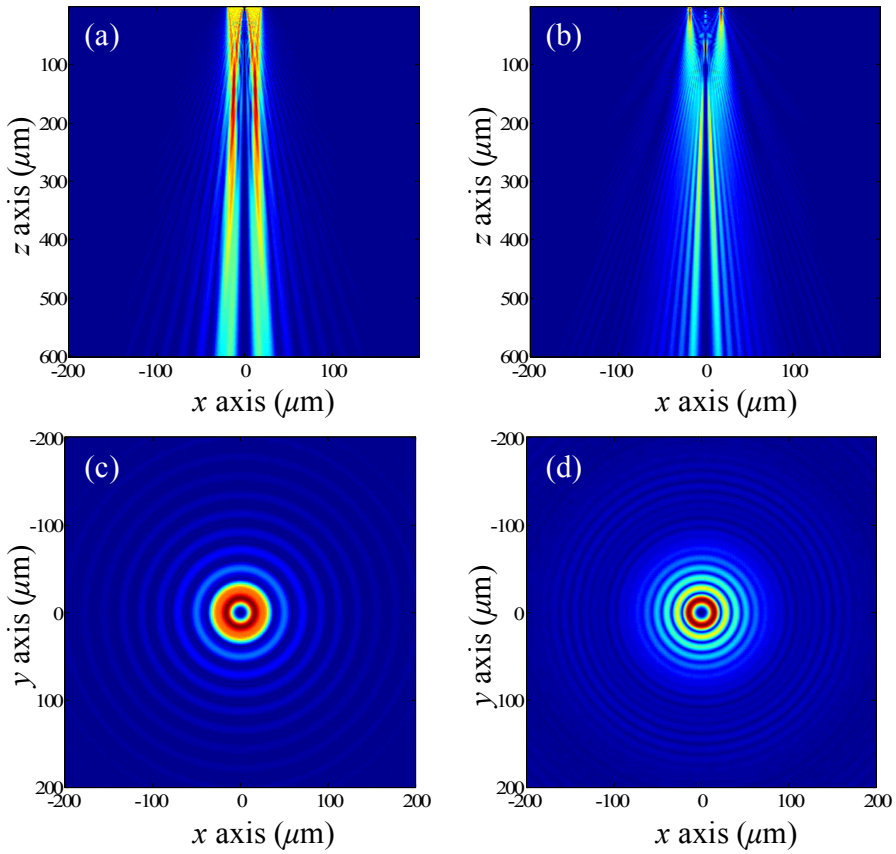


Figure 4.6 The x - z plane cross-sections of (a) the circular aperture and (b) the annular aperture show a slightly diverging profile of the vortex-cone. The x - y plane cross-sections ($z = 300 \mu\text{m}$) of (c) the circular aperture and (d) the annular aperture show vortex profiles with bright thick and thin vortex rings, respectively.

As shown in Figure 4.6, a dark vortex-cone wrapped by a bright cone-shaped caustic surface is formed along the optical axis. Figure 4.6(b) shows that if the annular aperture filters the incident optical field instead of the circular aperture, as shown in Figure 4.6(a), the vortex-cone region is smaller and more regularly defined, whereas when using a circular aperture, the vortex ring is relatively thick (see Figure 4.6(c) and (d)) and the width of the vortex-cone along the optic axis is not uniform (see Figure 4.6(a) and (b)). This characteristic of the formation of the thin vortex ring enables us to create

micro-scale multiple vortex-cones which are narrowly separated. The use of an annular aperture rather than a circular aperture is more advantageous in close inter-distanced multiple vortex-cones, as discussed above. The dynamic control of a multiple vortex-cones and the method used to control them are investigated in the following section.

The optical field on the surface of an annular aperture is given by $A(x,y)\exp[i(kz-\omega t+m\varphi)]$, where $A(x,y) = 1$ when $r_i < x^2 + y^2 < r_o$ at $z = 0$; otherwise, $A(x,y)$ is given as 0 at $z = 0$, where r_i is the inner radius of the annular aperture and r_o the outer radius. The phase modulation is considered to be of the m -th order, when the phase modulation is $m\varphi$, where m is an integer and φ varies from 0 to 2π , $\varphi = \tan^{-1}(y/x)$. With these terms, a third-order vortex-cone is formed by the linear phase modulation of $0-6\pi$ along the annular aperture perimeter in the counter-clock-wise direction.

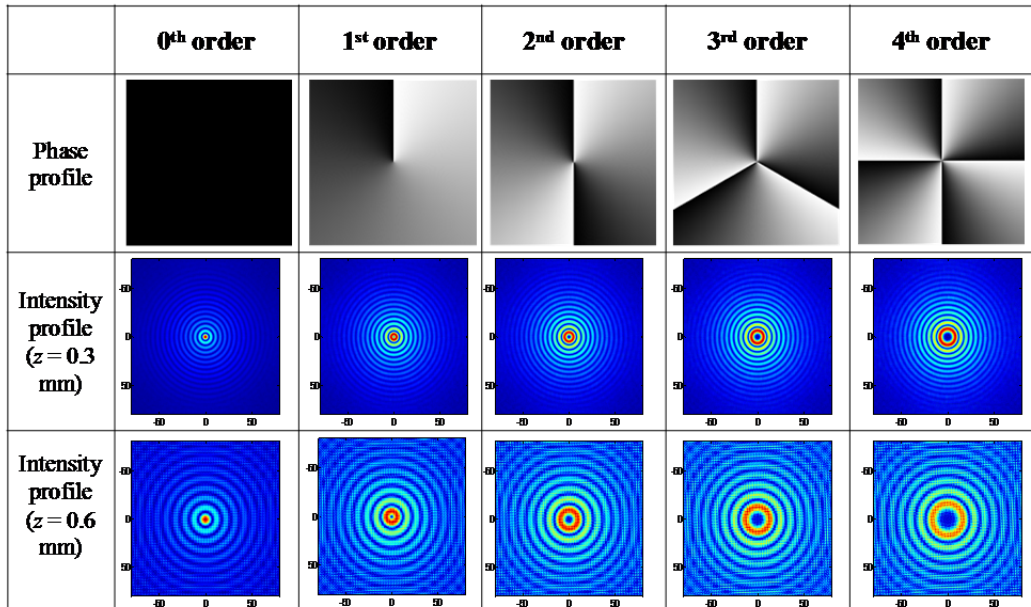


Figure 4.7 The phase modulation profiles of the zeroth to the fourth topological charges to be displayed on the SLM and the x - y cross-sections of the corresponding optical field profiles at $z = 0.3$ mm and 0.6 mm are shown.

In Figure 4.7, vortex-cones synthesized by the annular aperture ($r_i = 14 \mu\text{m}$, $r_o = 15$

μm) with several orders of phase modulation are presented. As shown in Figure 4.7, the zeroth-order beam is simply a Gaussian beam with a bright center. The figure shows that the divergence angle of the vortex-cone wrapped with a clear and thin vortex caustic surface increases with the order of the phase modulation.

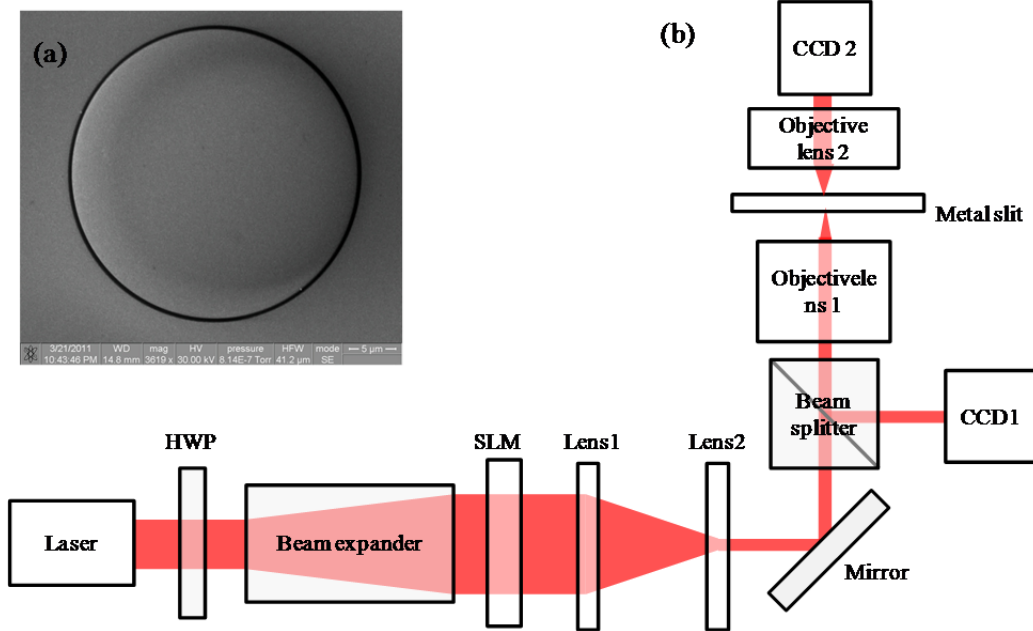


Figure 4.8 (a) A scanning electron microscopy (SEM) image of the annular aperture inscribed on the silver surface. (b) The overall experimental setup is shown.

In Figure 4.8(a) and (b), a SEM image of the annular ring aperture used in the experiment is presented and the experimental setup for the synthesis and measurement of the vortex-cones is schematically illustrated, respectively. To fabricate the sample, silver film with 300 nm thickness was deposited on a fused silica wafer. An annular aperture with a radius of 15 μm was then inscribed on the silver surface. In the experimental setup, the proposed direct-phase modulation technique through downscale imaging of an SLM on an annular aperture is implemented. A laser with a wavelength of 660 nm goes through a beam expander, and the expanded light propagates to a phase SLM (PLUTO of Holoeye). This SLM changes the phase of the light and supplies the proper phase

variation to form the vortex-cone at the annular aperture on the silver surface. The complex image of the SLM is scaled down by a convex lens (Lens 1), a concave lens (Lens 2) and an objective lens, and, consequently, a demagnified SLM image appears on the backside of the annular aperture. The obtained demagnification power is 1/72. Accurate alignment is a key requirement. To align the SLM image with the center of the annular aperture, Charge-Coupled Device 1 (CCD1) captures the overlapped image of the reflected SLM image from the backside of the annular-aperture sample and the annular aperture image itself through a beam splitter. Field images of the vortex-cones are captured by CCD 2.

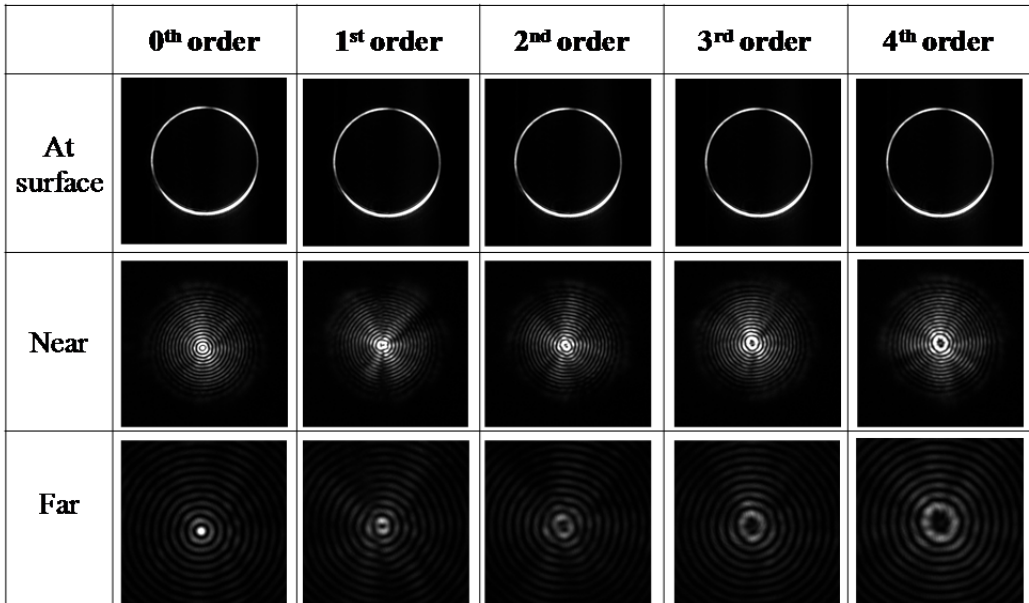


Figure 4.9 Experimentally measured optical field profiles at the aperture surface and relatively close and far planes over the aperture surface are displayed.

Figure 4.9 shows that the experimental results nearly match the simulation results of Figure 4.7. On the surface, as shown in Figure 4.9, all of the light coming from the aperture has the same circular shape. When moved away from the surface, each cone forms a differently sized circular pattern according to the respective topological charge.

Whereas the shape of the zeroth-order beam is a Gaussian beam, the other beams have the shape of a ring of which the center is a dark area. As the beam propagates longer, the dark area size becomes larger and the beam becomes cone-shaped. A higher order cone forms a vortex ring with a larger diameter ring than a lower order cone. As verified in the experimental result, the proposed direct downscale imaging technique of an SLM for the phase modulation of the annular aperture performed successfully the simultaneous control of the topological charge and the horizontal translation of a vortex-cone. This technique can be considered as a type of complex modulation with which both the phase and amplitude are controlled [75].

4.2.2. Generation and control of multiple vortex-cones

By tuning the magnification rate of the optical system, I can control the size of the SLM image on the aperture plane. Thus, it is possible to modulate the phase profile of multiple annular apertures simultaneously using the direct-phase modulation technique. In this section, four closely separated vortex-cones are generated and their topological charges and horizontal translations are controlled with sectional spiral-phase encoding. A phase SLM divided into four quadrants is used, and the four quadrants of the SLM have different instances of phase information with four different topological charges, as shown in Figure 4.10(a), which is imposed on the annular aperture array shown in Figure 4.10(b), as was inscribed on the silver film.

The experimental setup is identical to that of the single-aperture experiment. The film thickness, aperture radius, and demagnification power are also the same as those in the previous single-aperture experiment. The distance between each aperture is $30 \mu\text{m}$. If the number of apertures or the distance between the apertures is increased, the demagnified SLM image may not cover all of the apertures. In such a case, the demagnification power should be decreased. The simulation and experiment results are shown, respectively, in Figure 4.10(c) and (d). The right upper pattern is the zeroth-order cone, and the left upper cone, the left lower cone, and the right lower cone are the third-order cone, the fifth-order cone and the fourth-order cone, respectively. Multiple vortex-

cones can be formed and controlled separately with the phase SLM.

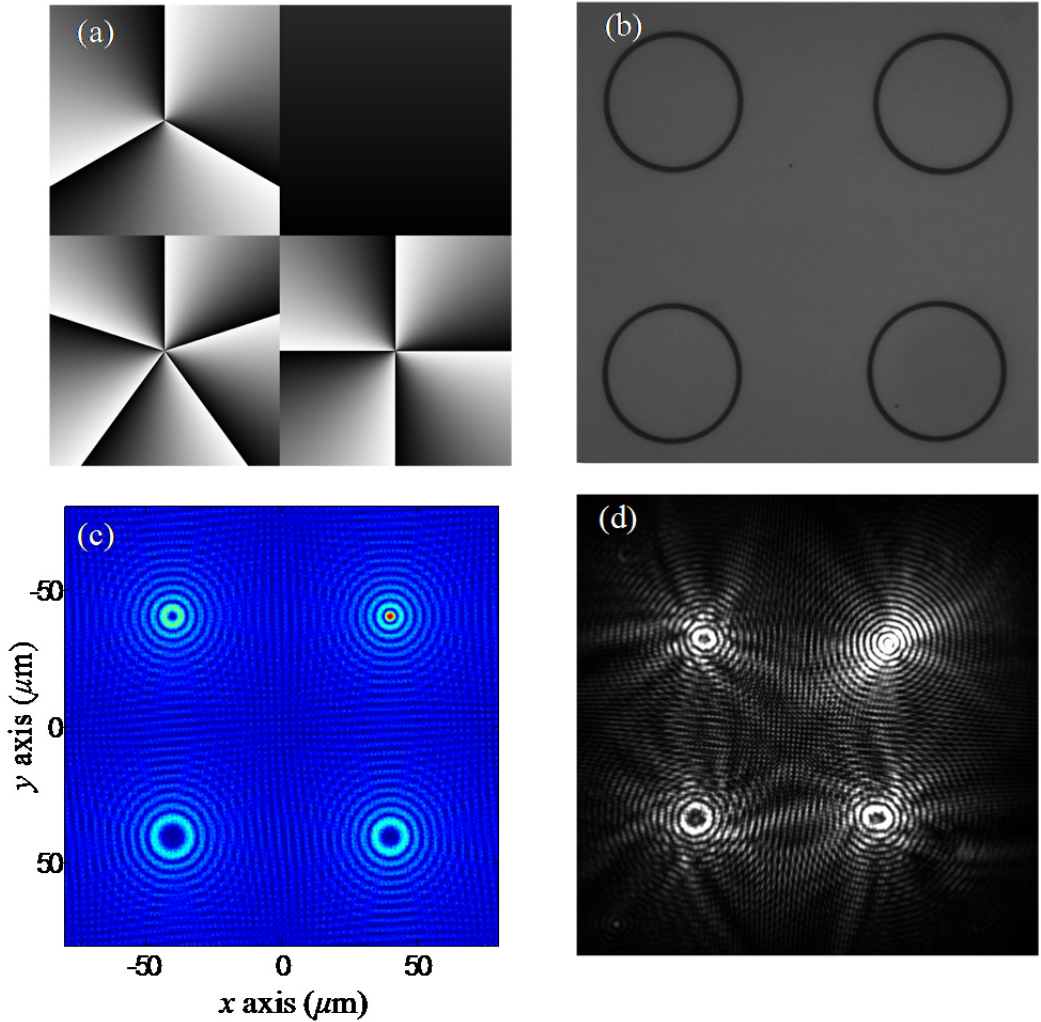


Figure 4.10 (a) The phase modulation profiles and (b) a CCD image of annular aperture array. (c) The simulation and (d) experimental results of multiple vortex-cones. The right upper vortex-cone denotes the zeroth-order topological charge (no vortex) and the left upper, left lower, and right lower vortex-cones denote the third-order, the fifth-order and the fourth-order topological charges, respectively.

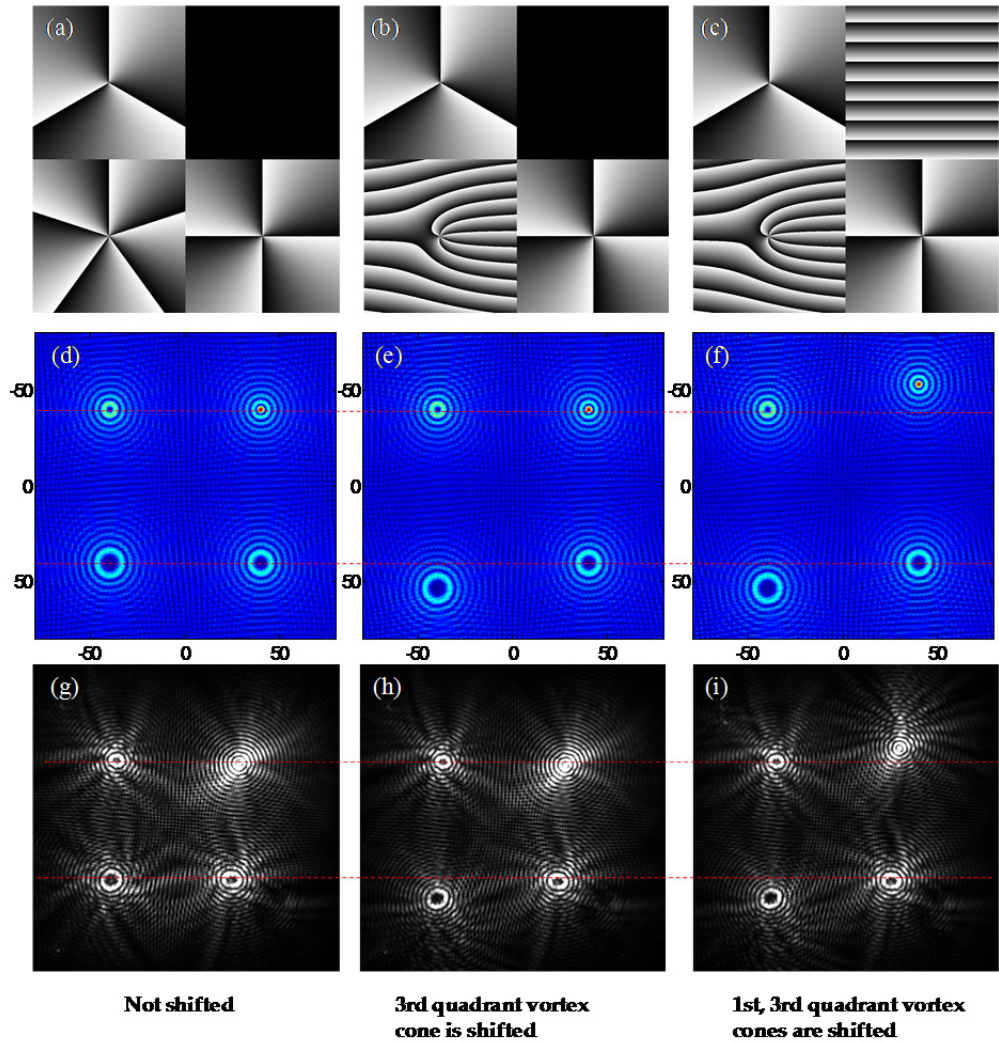


Figure 4.11 (a) ((b) and (c)) The phase profiles to induce the spatial shifting of the vortex-cones, (d) ((e) and (f)) the corresponding simulations, and (g)((h) and (i)) the experiment results. In this experiment, the vortex-cones in the first and third quadrant regions are shifted. The red dotted reference line is drawn for a comparison of the spatial positions of the vortex-cones.

On the other hand, the addition of a blazed linear phase profile to the spiral phase makes the generated vortex-cone shift horizontally on a specific horizontal plane. The exemplary results of this experiment are presented in Figure 4.11. Figure 4.11(a) shows

the same phase profile shown in Figure 4.10, which serves as a reference for comparison, through which four vortex-cones are arranged on the horizontal red dotted lines shown in Figure 4.11(a). The phase profiles obtained by superposing the blazed linear phase profile and the reference phase profile, shown in Figure 4.11(b) and (c), make the corresponding vortex-cones shift horizontally without degrading the shape. In Figure 4.11(e) and (h), the vortex-cone on the third quadrant is shifted downward without having an effect on the other vortex-cones. The second example in Figure 4.11(c) produces multiple vortex-cones with the vortex-cone on the first quadrant tilted upward and that on the third quadrant tilted downward.

Slightly separated and independently controlled multiple vortex-cones were experimentally generated and measured. Through the experiments, I noted that the direct-phase modulation technique is effective for controlling the topological charges and relative horizontal positions of tiny free-space vortex-cones dynamically. How close the inter-distance between the apertures and how close the vortex-cones can approach each other and thus cause significant degradation of the vortex-cones are actually limited by interference.

Chapter 5

Conclusion

The aim of this dissertation was to reveal and propose a method to modulate surface plasmon patterns. Scalar wave analysis and rigorous coupled wave analysis were applied to explain the generation of a surface plasmon pattern. Additionally, the method was verified with near-field and far-field experiments. It is shown that the polarization sensitivity of the plasmonic vortex lens can be utilized for the dynamic switching of the surface plasmon vortices with different topological charges.

In Chapter 2, I demonstrated that arbitrary low-dimensional SP light flows with controllable Poynting vector streams can be designed using the proposed PCFs. The concept of designing an arbitrary SP based low-dimensional light flow can be considered as a generalization of the synthetic focusing of SP fields. The SP caustic light flows extend the potential for novel applications to various fields, including opto-mechanics as well as optical manipulation technology and open an avenue for the management and control of low-dimensional light fields.

In Chapter 3, the model for generating and manipulating a plasmonic vortex with PVL and HVB is proposed and analyzed. The overall effect of the spin polarization s , helix winding number l and the geometric charge of PVL m are explained. s and l are

associated with the spin angular momentum and the orbital angular momentum, respectively. The topological charge j in the plasmonic vortex is given by the superposition rule ($j = l + m + s$), where l and m are real numbers and s is 1, 0 or -1. It is shown that the quantitative primary ring size of the vortex pattern is one of the solutions of the Bessel function of the first kind and that the primary ring sizes of the simulation result coincide well with the solutions. I believe that this finding can provide a novel means of generating and manipulating plasmonic hot spots and vortices.

In Chapter 4, the experimental verification for the plasmonic vortex lens was done. In Section 4.1, the plasmonic vortex lens with circular polarization excitation beam is shown to be advantageous for forming a single surface plasmon hot spot as well. I believe that SP vortices having such remarkable properties may become a core element for the manipulation and control of the electromagnetic field on the subwavelength scale and that they will eventually be extensively used for various applications, such as nano-scale microscopy, optical data storage, quantum computing and particle manipulation. In Section 4.2, I use a direct-phase modulation technique with accurate alignment to control multiple vortex cones simultaneously in free space. The topological charges and horizontal positions of tiny vortex cones can be successfully managed with an annular aperture array and a phase-type SLM. The proposed method addresses the technical need for dynamic control of the micro-scale optical field as required for various applications, such as optical tweezers, optical interconnections, and plasmonic field synthesis.

Bibliography

1. L. Novotny and B. Hecht, *Principles of Nano-optics* (Cambridge University Press, 2006).
2. A. Liebsch, *Electronic Excitations at Metal Surfaces* (Springer-Verlag, 1997).
3. H. Raether, *Surface Plasmons on Smooth and Rough Surfaces and on Gratings* (Springer-Verlag, 1988).
4. W. L. Barnes, A. Dereux, and T. W. Ebbesen, "Surface plasmon subwavelength optics," *Nature* **424**, 824-830 (2003).
5. S. Kawata, Y. Inouye, and P. Verma, "Plasmonics for near-field nano-imaging and superlensing," *Nature Photonics* **3**, 388-394 (2009).
6. J. a Schuller, E. S. Barnard, W. Cai, Y. C. Jun, J. S. White, and M. L. Brongersma, "Plasmonics for extreme light concentration and manipulation," *Nature Materials* **9**, 193-204 (2010).
7. B. Hecht, H. Bielefeldt, L. Novotny, Y. Inouye, and D. W. Pohl, "Local excitation, scattering, and interference of surface plasmons," *Phys. Rev. Lett.* **77**, 1889-1892 (1996).
8. J. Pendry, "Playing tricks with light," *Science* **285**, 1687-1688 (1999).
9. G. Wurtz, R. Pollard, and a. Zayats, "Optical Bistability in Nonlinear Surface-Plasmon Polaritonic Crystals," *Physical Review Letters* **97**, 1-4 (2006).
10. D. Pacifici, H. J. Lezec, and H. a. Atwater, "All-optical modulation by plasmonic excitation of CdSe quantum dots," *Nature Photonics* **1**, 402-406 (2007).
11. T. Nikolajsen, K. Leosson, and S. I. Bozhevolnyi, "Surface plasmon polariton based modulators and switches operating at telecom wavelengths," *Applied Physics Letters* **85**, 5833 (2004).
12. Z. Liu, J. M. Steele, W. Srituravanich, Y. Pikus, C. Sun, and X. Zhang, "Focusing surface plasmons with a plasmonic lens," *Nano Letters* **5**, 1726-9 (2005).

13. Z. Liu, J. M. Steele, H. Lee, and X. Zhang, "Tuning the focus of a plasmonic lens by the incident angle," *Applied Physics Letters* **88**, 171108 (2006).
14. H. Kim and B. Lee, "Diffractive slit patterns for focusing surface plasmon polaritons," *Optics Express* **16**, 8969-80 (2008).
15. G. M. Lerman, A. Yanai, and U. Levy, "Demonstration of nanofocusing by the use of plasmonic lens illuminated with radially polarized light," *Nano Letters* **9**, 2139-43 (2009).
16. Y. Gorodetski, A. Niv, V. Kleiner, and E. Hasman, "Observation of the Spin-Based Plasmonic Effect in Nanoscale Structures," *Physical Review Letters* **101**, 1-4 (2008).
17. S. I. Bozhevolnyi, V. S. Volkov, E. Devaux, J.-Y. Laluet, and T. W. Ebbesen, "Channel plasmon subwavelength waveguide components including interferometers and ring resonators," *Nature* **440**, 508-11 (2006).
18. H. J. Lezec, J. a Dionne, and H. a Atwater, "Negative refraction at visible frequencies.,," *Science* **316**, 430-2 (2007).
19. Y. Liu, T. Zentgraf, G. Bartal, and X. Zhang, "Transformational plasmon optics," *Nano Letters* **10**, 1991-7 (2010).
20. A. N. Grigorenko, N. W. Roberts, M. R. Dickinson, and Y. Zhang, "Nanometric optical tweezers based on nanostructured substrates," *Nature Photonics* **2**, 365-370 (2008).
21. G. Anetsberger, O. Arcizet, Q. P. Unterreithmeier, R. Rivière, a. Schliesser, E. M. Weig, J. P. Kotthaus, and T. J. Kippenberg, "Near-field cavity optomechanics with nanomechanical oscillators," *Nature Physics* **5**, 909-914 (2009).
22. J. F. Nye, *Natural Focusing and Fine Structure of Light: Caustics and Wave Dislocations* (Institute of Physics Publishing, 1994).
23. C. Charmousis, V. Onemli, Z. Qiu, and P. Sikivie, "Gravitational lensing by dark matter caustics," *Physical Review D* **67**, (2003).
24. B. Lee, I.-M. Lee, S. Kim, D.-H. Oh, and L. Hesselink, "Review on subwavelength confinement of light with plasmonics," *Journal of Modern Optics* **57**, 1479-1497 (2010).

25. B. Lee, S. Kim, H. Kim, and Y. Lim, "The use of plasmonics in light beaming and focusing," *Progress in Quantum Electronics* **34**, 47-87 (2010).
26. H. Kim, J. Park, S.-woo Cho, S.-yeol Lee, M. Kang, and B. Lee, "Synthesis and dynamic switching of surface plasmon vortices with plasmonic vortex lens," *Nano Letters* **10**, 529-36 (2010).
27. H. Kim and B. Lee, "Unidirectional Surface Plasmon Polariton Excitation on Single Slit with Oblique Backside Illumination," *Plasmonics* **4**, 153-159 (2009).
28. H. W. Kihm, K. G. Lee, D. S. Kim, J. H. Kang, and Q.-H. Park, "Control of surface plasmon generation efficiency by slit-width tuning," *Applied Physics Letters* **92**, 051115 (2008).
29. M. G. Moharam and T. K. Gaylord, "Rigorous coupled-wave analysis of planar-grating diffraction," *J. Opt. Soc. Am.* **71**, 811-818 (1981).
30. P. Lalanne and G. M. Morris, "Highly improved convergence of the coupled-wave method for TM polarization," *J. Opt. Soc. Am. A* **13**, 779-784 (1996).
31. H. Kim, I.-M. Lee, and B. Lee, "Extended scattering-matrix method for efficient full parallel implementation of rigorous coupled-wave analysis," *Journal of the Optical Society of America. A, Optics, image science, and vision* **24**, 2313-27 (2007).
32. E. Lombard, a Drezet, C. Genet, and T. W. Ebbesen, "Polarization control of non-diffractive helical optical beams through subwavelength metallic apertures," *New Journal of Physics* **12**, 023027 (2010).
33. V. E. Lembessis, S. Al-Awfi, M. Babiker, and D. L. Andrews, "Surface plasmon optical vortices and their influence on atoms," *Journal of Optics* **13**, 064002 (2011).
34. P. S. Tan, X.-C. Yuan, J. Lin, Q. Wang, T. Mei, R. E. Burge, and G. G. Mu, "Surface plasmon polaritons generated by optical vortex beams," *Applied Physics Letters* **92**, 111108 (2008).
35. P. S. Tan, G. H. Yuan, Q. Wang, N. Zhang, D. H. Zhang, and X.-C. Yuan, "Phase singularity of surface plasmon polaritons generated by optical vortices," *Optics Letters* **36**, 3287-3289 (2011).
36. S. V. Boriskina and B. M. Reinhard, "Adaptive on-chip control of nano-optical fields with optoplasmonic vortex nanogates," *Optics express* **19**, 22305-15 (2011).

37. J. Trevino, H. Cao, and L. Dal Negro, "Circularly symmetric light scattering from nanoplasmonic spirals," *Nano Letters* **11**, 2008-2016 (2011).
38. S.-Y. Lee, J. Park, H. Kim, S.-W. Cho, M. Kang, and B. Lee, "Controlling the state of surface plasmon vortex by changing the topological charge and polarization state," in *Proc. SPIE* (2010), pp. 7757-128.
39. B. E. A. Saleh and M. C. Teich, *Fundamentals of Photonics*, 2nd ed. (Wiley Interscience, 2007).
40. Z. Bomzon, G. Biener, V. Kleiner, and E. Hasman, "Radially and azimuthally polarized beams generated by space-variant dielectric subwavelength gratings," *Optics Letters* **27**, 285-287 (2002).
41. P. Lalanne, J. Hugonin, and J. Rodier, "Theory of Surface Plasmon Generation at Nanoslit Apertures," *Physical Review Letters* **95**, 1-4 (2005).
42. J. Leach, E. Yao, and M. J. Padgett, "Observation of the vortex structure of a non-integer vortex beam," *New Journal of Physics* **6**, 71-71 (2004).
43. S. H. Tao, W. . M. Lee, and X.-C. Yuan, "Dynamic optical manipulation with a higher-order fractional bessel beam generated from a spatial light modulator," *Optics Letters* **28**, 1867-1869 (2003).
44. G. M. Lerman, L. Stern, and U. Levy, "Generation and tight focusing of hybridly polarized vector beams," *Optics express* **18**, 27650-27657 (2010).
45. A. Ishimaru, *Electromagnetic Wave Propagation, Radiation, and Scattering* (Prentice Hall, 1991).
46. J. D. Jackson, *Classical Electrodynamics*, 3rd ed. (Wiley, 1998).
47. K. Volke-Sepulveda, VGarcés-Chavez, SChavez-Cerda, J. Arlt, and K. Dholakia, "Orbital angular momentum of a high-order Bessel light beam," *Journal of Optics B* **4**, S82 (2002).
48. E. D. Palik, *Handbook of Optical Constants of Solids* (Academic Press, 1991).
49. I. Horcas, R. Fernández, J. M. Gómez-Rodríguez, J. Colchero, J. Gómez-Herrero, and a M. Baro, "WSXM: a software for scanning probe microscopy and a tool for nanotechnology," *The Review of scientific instruments* **78**, 013705 (2007).

50. V. V. Kotlyar, A. a Almazov, S. N. Khonina, V. a Soifer, H. Elfstrom, and J. Turunen, "Generation of phase singularity through diffracting a plane or Gaussian beam by a spiral phase plate," *Journal of the Optical Society of America A, Optics, image science, and vision* **22**, 849-61 (2005).
51. F. López-Tejeira, S. G. Rodrigo, L. Martín-Moreno, F. J. García-Vidal, E. Devaux, T. W. Ebbesen, J. R. Krenn, I. P. Radko, S. I. Bozhevolnyi, M. U. González, J. C. Weeber, and a. Dereux, "Efficient unidirectional nanoslit couplers for surface plasmons," *Nature Physics* **3**, 324-328 (2007).
52. C. Paterson and R. Smith, "Higher-order Bessel waves produced by axicon-type computer-generated holograms," *Optics Communications* **124**, 121-130 (1995).
53. H. He, M. E. J. Friese, N. R. Heckenberg, and H. Rubinsztein-Dunlop, "Direct observation of transfer of angular momentum to absorptive particles from a laser beam with a phase singularity," *Physical Review Letters* **75**, 826–829 (1995).
54. M. E. J. Friese, J. Enger, H. Rubinsztein-Dunlop, and N. Heckenberg, "Optical angular-momentum transfer to trapped absorbing particles," *Physical review. A* **54**, 1593-1596 (1996).
55. N. B. Simpson, K. Dholakia, L. Allen, and M. J. Padgett, "Mechanical equivalence of spin and orbital angular momentum of light: an optical spanner," *Optics Letters* **22**, 52-4 (1997).
56. E. M. Wright and N. I. Zheludev, "Broken Time Reversal and Parity Symmetries for Electromagnetic Excitations in Planar Chiral Nanostructures," *Physics* **2-5** (2008).
57. Y. Gorodetski, N. Shitrit, I. Bretner, V. Kleiner, and E. Hasman, "Observation of optical spin symmetry breaking in nanoapertures," *Nano Letters* **9**, 3016-9 (2009).
58. Z. Jiang, Q. Lu, and Z. Liu, "Propagation of apertured Bessel beams," *Applied Optics* **34**, 7183-7185 (1995).
59. M. W. Beijersbergen, R. P. C. Coerwinkel, M. Kristensen, and J. P. Woerdman, "Helical-wavefront laser beams produced with a spiral phaseplate," *Optics Communications* **112**, 321-327 (1994).
60. Z. Bouchal, "Vortex array carried by a pseudo-nondiffracting beam," *Journal of the Optical Society of America A* **21**, 1694-1702 (2004).

61. J. Courtial, R. Zambrini, M. R. Dennis, and M. Vasnetsov, "Angular momentum of optical vortex arrays," *Optics Express* **14**, 938-949 (2006).
62. Z. Bouchal, J. Wagner, and M. Chlup, "Self-reconstruction of a distorted nondiffracting beam," *Optics Communications* **151**, 207-211 (1998).
63. C.-Y. Hwang, D. Choi, K.-Y. Kim, and B. Lee, "Dual Airy beam," *Optics express* **18**, 23504-23516 (2010).
64. H. J. Lezec, A. Degiron, E. Devaux, R. a Linke, L. Martin-Moreno, F. J. Garcia-Vidal, and T. W. Ebbesen, "Beaming light from a subwavelength aperture," *Science* **297**, 820-822 (2002).
65. S. Kim, Y. Lim, H. Kim, J. Park, and B. Lee, "Optical beam focusing by a single subwavelength metal slit surrounded by chirped dielectric surface gratings," *Applied Physics Letters* **92**, 013103 (2008).
66. A. T. O'Neil, I. MacVicar, L. Allen, and M. J. Padgett, "Intrinsic and Extrinsic Nature of the Orbital Angular Momentum of a Light Beam," *Physical Review Letters* **88**, 053601 (2002).
67. J. E. Curtis and D. G. Grier, "Modulated optical vortices," *Optics Letters* **28**, 872-874 (2003).
68. J. Curtis and D. Grier, "Structure of Optical Vortices," *Physical Review Letters* **90**, 133901 (2003).
69. C.-shan Guo, Y.-nan Yu, and Z. Hong, "Optical sorting using an array of optical vortices with fractional topological charge," *Optics Communications* **283**, 1889-1893 (2010).
70. C.-S. Guo, X. Liu, J.-L. He, and H.-T. Wang, "Optimal annulus structures of optical vortices," *Optics express* **12**, 4625-4634 (2004).
71. T. Cizmar and K. Dholakia, "Tunable Bessel light modes : engineering the axial propagation," *Optics Express* **17**, 15558-15570 (2009).
72. W. M. Lee, X. C. Yuan, and W. C. Cheong, "Optical vortex beam shaping by use of highly efficient irregular spiral phase plates for optical micromanipulation," *Optics Letters* **29**, 1796-1798 (2004).
73. Y. Izdebskaya, V. Shvedov, and A. Volyar, "Generation of higher-order optical vortices by a dielectric wedge," *Optics Letters* **30**, 2472-2474 (2005).

74. J. E. Morris, T. Cizmar, H. I. C. Dalgarno, R. F. Marchington, F. J. Gunn-Moore, K. Dholakia, and T. Čižmár, "Realization of curved Bessel beams: propagation around obstructions," *Journal of Optics* **12**, 124002 (2010).
75. H. Kim and B. Lee, "Diffractive Optical Element with Apodized Aperture for Shaping Vortex-Free Diffraction Image," *Japanese Journal of Applied Physics* **43**, L1530-L1533 (2004).

한글 초록

표면 플라즈몬은 자유전자와 결합하여 금속과 유전체 사이의 표면을 따라 전송되는 전자기파로, 표면에서 거리가 멀어질 수록 그 크기가 급격히 감소되어 대부분의 에너지가 표면에 집중되어 있는 특징을 가진다. 플라즈모닉스를 이용한 나노 광소자 제작을 위하여 금속과 유전체 구조에서의 표면 플라즈몬파의 집중적 연구가 수행되어왔다. 이러한 나노 광소자들을 이용하여 다양한 표면플라즈몬 패턴을 생성할 수 있다. 이러한 표면 플라즈몬 생성은 최근 플라즈모닉스의 기초 연구 분야로 자리 잡았다. 과장한계 이하의 핫스팟을 형성하는 것에서부터 시작된 표면 플라즈몬 패턴 형성에 관한 연구는 단일 핫스팟만이 아닌 복잡한 표면 플라즈몬의 회절광학을 이용한 형성 및 표면 플라즈몬 패턴의 능동적인 제어 등 다양하게 이루어지고 있다. 본 학위 논문에서는 플라즈모닉 렌즈를 이용하여 표면 플라즈몬을 변조하는 방법을 연구하고, 플라즈모닉 렌즈를 이용하여 다양한 표면 플라즈몬 패턴을 생성하는 방법을 제시한다.

먼저 표면플라즈몬 포락선을 이용하여 광 파워가 특정 방향으로 형성되는 곡면을 형성하는 방법을 제시한다. 자연 현상에서 여러 경로에서 오는 빛이 어느 지점으로 집중될 때, 그 빛의 외곽선의 집합은 다양한 모양의 포락선을 형성하게 된다. 본 논문에서는 표면 플라즈모닉 포락선을 만들기 위한 플라즈모닉 초점기를 제안하고 다양한 모양의 곡선들을 생성하는 방법을 실험적으로 보였다. 플라즈모닉 포락선 초점기는 2차원에서의 빛 에너지의 흐름을 제어하는 방법이 될 것이다.

플라즈모닉 소용돌이 현상에서의 빛의 회전 운동량과 궤도 운동량 두 가지에 대해 정량적으로 해석을 하였다. 플라즈모닉 렌즈에 회전 운동량과 궤도 운동량을 가진 나선형의 벡터 빔을 조사하는 경우에 이 두 가지의 운동량이 플라즈모닉

소용돌이 형성에 기여한다. 플라즈모닉 렌즈의 구조와 이러한 두 운동량이
플라즈모닉 소용돌이에 미치는 영향을 분석하는 모델을 제시하고, 이들이
선형적으로 결합되어 플라즈모닉 소용돌이의 위상을 결정한다는 것을 보여주었다.
또한 입사되는 빛의 운동량 및 플라즈모닉 렌즈의 구조 차수가 분수 값을 가지는
경우에 플라즈모닉 소용돌이에 미치는 영향에 대한 해석을 하였다.

플라즈모닉 렌즈를 이용하여 플라즈모닉 소용돌이를 형성하는 것을
실험적으로 보였다. 편광과 플라즈모닉 렌즈의 구조를 제어하여 플라즈모닉
소용돌이의 위상을 다양하게 제어할 수 있음을 보였다. 입사되는 빛의 운동량과
플라즈모닉 렌즈의 차수가 선형 결합이 됨을 실험적으로 보였다. 또한 복수의 원환
개구와 공간 광 변조기를 이용하여 복수의 소용돌이 빔을 만드는 연구를 하였다.
복수의 소용돌이 빔을 생성하고 수직 수평 위치를 개별적으로 조정하는 것이
가능함을 원환 개구에 조사되는 빛의 위상을 직접적으로 제어하는 방식의
실험으로 보였다. 이러한 연구는 표면 플라즈몬 패턴 형성 제어 분야에 있어
중요한 역할을 할 것으로 보인다.